2009-09-18

Gas Phase Chiral Recognition, Characterization of Porous Polymer Monolith Nanospray Ionization, and the Negative Mode CRAFTI Method Using Fourier Transform Ion Cyclotron Resonance Mass Spectrometry

Nannan Fang
Brigham Young University - Provo

Gas Phase Chiral Recognition, Characterization of Porous Polymer Monolith Nanospray Ionization, and the Negative Mode CRAFTI Method Using Fourier Transform Ion Cyclotron Resonance Mass Spectrometry

by

Nannan Fang

A dissertation submitted to the faculty of
Brigham Young University
in partial fulfillment of the requirements for the degree of

Doctor of Philosophy

Department of Chemistry and Biochemistry
Brigham Young University
December 2009

BRIGHAM YOUNG UNIVERSITY

GRADUATE COMMITTEE APPROVAL

of a dissertation submitted by

Nannan Fang

This dissertation has been read by each member of the following graduate committee and by majority vote has been found to be satisfactory.

Date	David V. Dearden, Chair
Date	Daniel E. Austin
Date	Roger G. Harrison
Date	Matthew R. Linford
Date	Jaron C. Hansen

BRIGHAM YOUNG UNIVERSITY

As chair of the candidate's graduate committee, I have read the dissertation of Nannan Fang in its final form and have found that (1) its format, citations and bibliographical style are consistent and acceptable and fulfill university and department style requirements; (2) its illustrative materials including figures, tables, and charts are in place; and (3) the final manuscript is satisfactory to the graduate committee and is ready for submission to the university library.

Date	David V. Dearden Chair, Graduate Committee

Accepted for the Department

Date	David V. Dearden Graduate Coordinator

Accepted for the College

Date	Thomas W. Sederberg Associate Dean, College of Physical and Mathematical Sciences

ABSTRACT

Gas Phase Chiral Recognition, Characterization of Porous Polymer Monolith Nanospray Ionization, and the Negative Mode CRAFTI Method Using Fourier Transform Ion Cyclotron Resonance Mass Spectrometry

Nannan Fang
Department of Chemistry and Biochemistry
Doctor of Philosophy

Our group has been studying chiral recognition in gas phase using mass spectrometry for more than 10 years. We are interested in gas phase studies of fundamental interactions because the gas phase avoids complications and masking effects that may arise upon solvation. Therefore, the results of gas phase experiments can be directly compared with those of high-level computational studies. In chapter 2, I studied the roles of hydrogen bonding and π stacking in gas phase chiral recognition between aromatic crown molecules and aromatic amines. High affinity between host and guest doesn't necessarily result in better recognition. If the affinity is too high, both host enantiomers will bind to the chiral guest very tightly so little discrimination is observed. In order to build an efficient chiral recognition system, we need to select

a host and guest that have intermediate binding affinity. Hydrogen bonding is another significant factor that controls the host-guest affinity. In the case of host 1, more hydrogen bonds results in better recognition. We also find that the degree of chiral recognition is greater in the gas phase than in solution. Modeling at the B3LYP/6-31G* level is qualitatively correct, but quantitative agreement with experiment is poor.

Inspired by Rekharsky's work which shows successful induced chiral recognition with an achiral host (cucurbituril) in solution, we tested the possibility of applying cucurbiturils as gas phase chiral recognition containers in chapter 5. Conferring chirality on cucurbiturils makes the chiral recognition happen in a restricted space, which might strengthen or hinder the discrimination. By comparing our results with Rekharsky's, we showed the role of solvent in this chiral recognition process. In the gas phase, the enantiodiscrimination does not happen between the "leaving" MP and the "approaching" stronger chiral binder. Because hydrophobic effects are absent in the gas phase, it is possible that the hydrophobic methyl substituent of 2-methylpiperazine and the stronger chiral binder might not be simultaneously included inside the cavity. Therefore, we do not observe enantiodiscrimination in gas phase. The dissociation experiment for the CB[7] ternary complex shows that *sec*-butylamine binds externally to the CB[7] host. Further, the heterochiral diastereomer is more stable than the homochiral diastereomer. This conclusion is consistent with Rekharsky's result in solution.

For more than 15 years, the most common ionization method in our lab has been

electrospray ionization. However, ESI is subject to problems with ion suppression, especially when the sample is a mixture or it has a high concentration of salt. The easily ionized molecules tend to scavenge the available charges in the spray solution and dominate the resulting ion population even though other compounds may be present in high abundance. Nanoelectrospray usually yields cold ionization, and analyte suppression can be greatly reduced at nanospray flow rates. Therefore, we constructed a porous polymer monolith (PPM) nanospray emitter similar to that described by Oleschuk et al. and characterized the properties of the PPM emitter. This work is described in chapter 3. Our tests show that this PPM nanospray emitter possesses some special analytical properties: decreased ion suppression, quite stable spray, strong signal intensity and good reproducibility in emitter performance.

Chapter 4 deals with the application of the new CRAFTI method to negative ions. CRAFTI stands for cross-sectional areas by Fourier transform ICR. The CRAFTI technique measures collision cross sections, providing a probe of the gas phase conformations of supramolecular complexes. Our preliminary work has shown that CRAFTI is applicable to positive ions, so we further demonstrate the application of the newly-developed method to negative ions in this work.

Based on the fact that the experimental cross sections correlate linearly with the theoretical values, we have obtained evidence that CRAFTI is a valid method for negative ions. However, some problems remain. First, we are still working to understand the physical meaning of the CRAFTI cross sections. The absolute values we obtain are generally greater than those obtained from momentum transfer cross

section calculations modeled in helium. Second, the precision of the measurements (currently about 2-3%) is still larger than we desire. We need to carefully tune the excitation and isolation amplitudes to make the signal strong and monoisotopic for weak ions. CRAFTI is a very promising and attractive method because FT-ICR provides accurate mass-to-charge measurement along with the cross section measurement. In other words, one technique is sufficient to obtain the shape, size and mass of a molecule simultaneously.

ACKNOWLEDGEMENTS

At the moment that I complete my Ph.D. study and dissertation, I would like to express my sincere appreciation to my advisor, Dr. David V. Dearden. During my Ph. D. program, he is always helpful and patient in guiding me to become a qualified chemist.

I would like to give my special thanks to my Ph. D. committee members, Dr. Daniel E. Austin, Dr. Matthew R. Linford, Dr. Jaron C. Hansen, and Dr. Roger G. Harrison, for their advice and help through my research and yearly progress reports. The Department of Chemistry & Biochemistry at Brigham Young University grants scholarship to me for my graduate studies, and I really appreciate their support.

I gratefully thank our group members, Haizhen Zhang, Fan Yang and Ruijun Shi, for their help and friendship these years. I would like to thank Binghe Gu, a graduate student in Dr. Milton L. Lee's group, for his help in fabricating PPM emitters.

I would like to thank my parents, who always encourage me and support me during my studies in USA.

Finally I would like to share this work with my husband, Dianliang. It is his company and love that makes me feel energetic to accomplish my Ph.D. program.

Table of Contents

Table of Figures

Table of Tables

Chapter 1

Fourier Transform Ion Cyclotron Resonance Mass Spectrometry

Introduction

Fourier transform ion cyclotron resonance mass spectrometry (FTICR-MS), also called Fourier transform mass spectrometry, is a type of analytical technique for determining the mass-to-charge ratio (m/z) of ions based on the cyclotron frequency of the ions in a fixed magnetic field. In the 1950's, the technique of ICR-MS was first published as a demonstration for measuring very small mass differences at very high precision.[1] Inspired by Fourier transform nuclear magnetic resonance (FT-NMR) spectroscopy, Alan G. Marshall and Melvin B. Comisarow applied FT methods to ICR-MS. They experimentally proved this new FTICR-MS technique in 1974 at the University of British Columbia.[2] After that, Marshall kept developing FTICR-MS techniques at Ohio State University and Florida State University. By 2007, more than 700 FT-ICR mass spectrometers had been installed in laboratories worldwide.

FT-ICR-MS is a powerful technique because it possesses the following features simultaneously: ultra high resolving power and mass accuracy, ultra high sensitivity, one spectrum for all ions at the same time, detecting ions without destroying them, the capability of trapping ions for ion reaction and ion fragmentation to perform multistage tandem mass spectrometry experiments (Collision Induced Dissociation, Electron Capture Dissociation, Infrared Multiphoton Photodissociation etc.), and adaptability to various internal and external ionization sources (EI, CI, FAB, ESI,

MALDI DESI etc.). These advantages have made FT-ICR a very powerful technique for a wide variety of samples such as petroleum, river sludge, pharmaceuticals, biological samples, etc.[3, 4] In recent years, HPLC and CE interfaces have become available to FTICR-MS. Therefore, FTICR MS becomes more and more universally applicable in modern chemistry. Currently, the highest-field superconducting ICR magnet in the world is the 14.5 Tesla FTICR-MS instrument at the National High Magnetic Field Laboratory.[5] A new 21 T state-of-the-art superconducting system is in the development phase, also at the National High Magnetic Field Laboratory.[5]

This chapter includes some important aspects related to FT-ICR-MS, such as theory, instrumentation, performance, and applications.

Theory

The physics of ions in FTICR trapping cell. The trapping cell is located inside a spatially uniform static superconducting high field magnet (typically 4.7 to 14.5 Tesla) cooled by liquid helium and liquid nitrogen. Figure 1.1 shows a schematic of a rectangular ICR trapping cell, which is composed of trapping plates, excitation plates and detection plates. When ions are injected into the trapping cell, they will have three different types of ion motion: cyclotron motion, trapping oscillation, and magnetron motion.

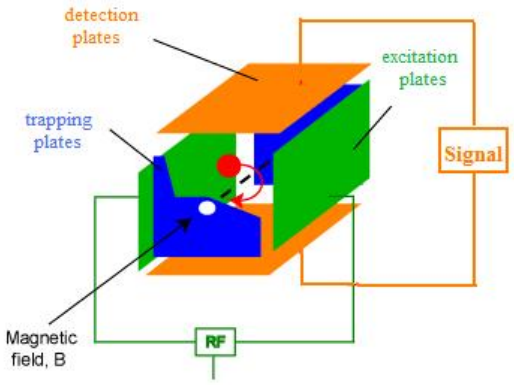

Figure 1.1: A Schematic of a rectangular ICR trapping cell (trapping plates: blue, excitation plates: green, and detection plates: orange.)[7]

Cyclotron Motion. In a constant-strength magnetic field, a charged ion will bend its original path into a circular motion in a plane perpendicular to the magnetic field due to the Lorentz force (Figure 1.2). Ions are prevented from getting out of the cell by the trapping plates at each end (Figure 1.1). The Lorentz force for an ion with a mass m, charge q and velocity **v** is given by equation (1-1) in a constant magnetic field **B**.

Lorentz force $F = q\mathbf{v} \times \mathbf{B}$ (1-1)

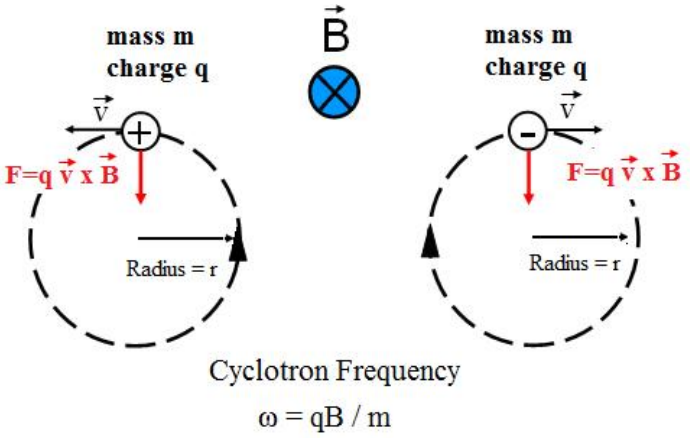

Figure 1.2: Ion cyclotron motion[4]

For a stable circular orbit, the centrifugal force outward exactly balances the magnetic force inward. Therefore, it results in equation 1-2.

$$qvB = mv^2 / r \qquad (1\text{-}2)$$

The angular velocity, ω, is defined as

$$\omega = v / r \qquad (1\text{-}3)$$

From equation (1-2) and (1-3), equation 1-4 is derived:

$$\omega_c = qB / m \qquad (1\text{-}4)$$

Herein, ω_c is defined as the ion cyclotron frequency. Equation (1-4) shows that the cyclotron frequency of the ion is inversely proportional to its mass-to-charge ratio. That is to say a group of ions with a certain mass-to-charge ratio have the same cyclotron frequency no matter what velocity the ions have. Therefore, accurate mass-to-charge ratio measurements can be obtained by measuring the cyclotron frequency without worrying about the translational energy distribution of the ions.

Trapping Oscillation. When the ions enter the ICR trapping cell after they pass the ion guide, their velocity in the magnetic field direction is big enough for them to fly out of the trapping cell. In order to avoid the above situation, a voltage is applied to the front and back trapping plates to repel the ions from the trapping plates. Thus, ions also move in harmonic oscillation along the magnetic field direction between the two trapping plates (Figure 1.3) while they are moving in cyclotron motion. That means the ion cyclotron motion is superimposed on a uniform axial oscillation motion. The trapping oscillation frequency, f_t, can be calculated according to equation (1-5).

$$f_t = 2.21088 \times 10^3 (q\alpha V / ma^2)^{1/2} \qquad (1\text{-}5)$$

In the equation above,[4] α is a geometry factor (2.77373 for the cube) of the cell, q is the ion charge, a is the cell length and V is the trapping voltage. Typically the trapping oscillation frequency is small compared to the cyclotron frequency, with a value of tens of kHz.

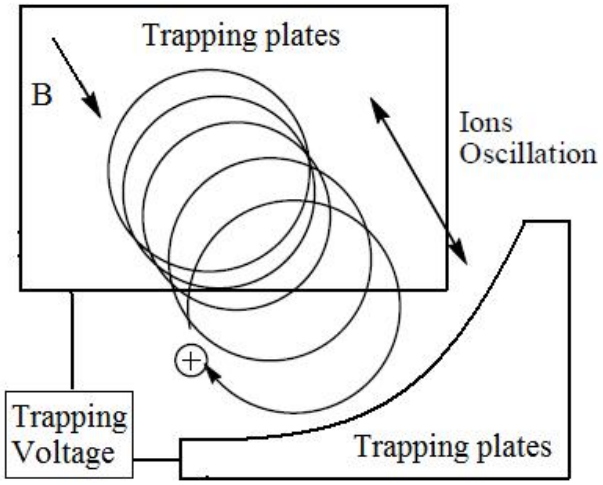

Figure 1.3: Ion trapping oscillation along the magnetic field direction.

Magnetron Motion. After introducing the ion cyclotron motion and trapping oscillation, we should talk about the third fundamental ion motion in the ICR trapping cell, which is called magnetron motion (Figure 1.4). Ion magnetron motion is formed under the combined influence of magnetic field and radial electric field. Ideally the direction of the trap electric field ought to be parallel to that of the magnetic field, but the finite dimension of the ICR trapping cell give rise to a radial component of the trap electric field. This radial electric field generates an electrostatic force on the ion and drags the ion in a direction opposite to the Lorentz force. Therefore, the cyclotron frequency in equation (1-4) needs to be modified to meet the real situation. The

relationship between the real cyclotron frequency ω_c' and the theoretical cyclotron frequency ω_c is shown in equation (1-6). Herein ω_t is the trapping oscillation frequency. As we know, ω_t is usually small compared to ω_c, so the real cyclotron frequency is only slightly smaller than the theoretical value.

$$\omega_c' = \omega_c/2 + [(\omega_c/2)^2 - (\omega_t^2/2)]^{1/2} \qquad (1\text{-}6)$$

$$\omega_m = \omega_c/2 - [(\omega_c/2)^2 - (\omega_t^2/2)]^{1/2} \qquad (1\text{-}7)$$

Equation (1-7) shows how to calculate magnetron frequency according to theoretical cyclotron frequency and trapping oscillation frequency. Because ω_t is usually small compared to ω_c, ω_m should have a very small value (typically 100 Hz). Therefore, magnetron motion, even if coherent, is generally not detectable, because it is usually lower than the low-frequency limit of the detection circuit (typically a few kHz).

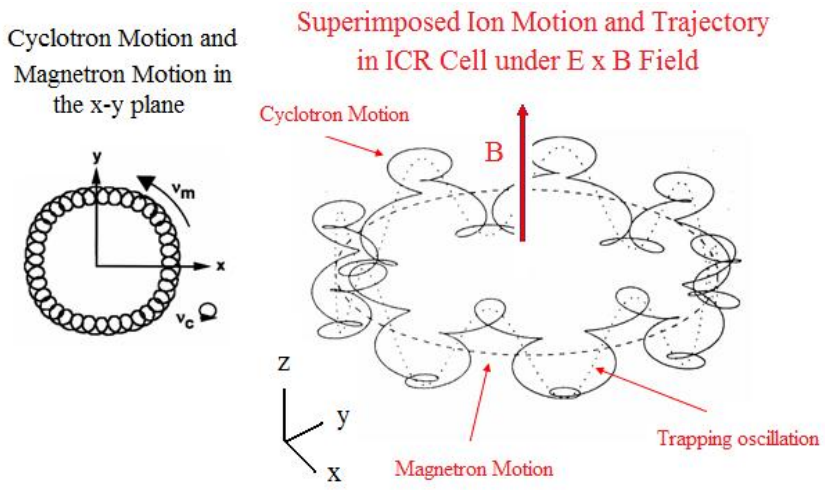

Figure 1.4: Cyclotron motion and magnetron motion in the x-y plane in the ICR cell (left); A schematic of superimposed ion motion and trajectory (right)[4]

Excitation and detection of an ICR signal. Now that the m/z information that we are interested in is related to the ion cyclotron frequency, we need to figure out

how to determine the ion cyclotron frequency in the trapping cell. To make the ion cyclotron frequency observable, ions with the same m/z should get close enough to the detector plates (the initial orbit radii are quite small) and rotate coherently in a packet (randomly distributed ions contribute net zero to the detectable image current). Therefore, ions need to be excited before detection by applying a RF potential to a pair of opposite excitation plates. When the frequency of the RF potential matches the natural cyclotron frequency of a particular m/z packet of ions, the ions are exposed to a net outward electric force and are therefore excited to a larger orbital radius.

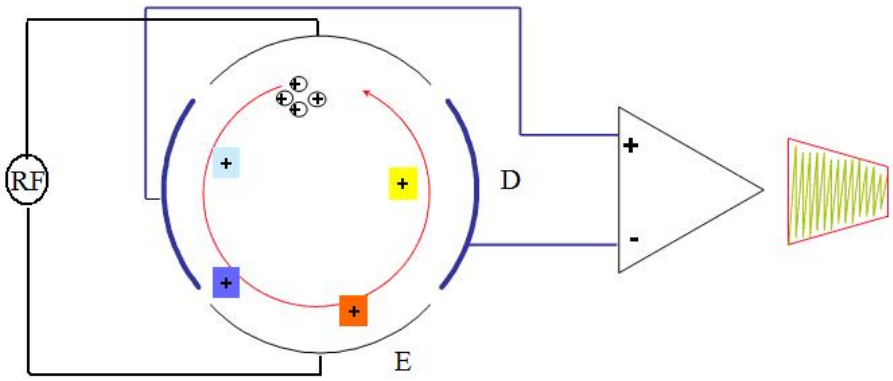

Figure 1.5: Ion excitation and detection in the ICR cell (D: detection paltes, E: excitation plates)[8]

Figure 1.5 is a schematic illustrating ion excitation and detection. In the picture, ions of the same m/z ratio are excited into a coherent packet with a larger orbit, where ions can induce detectable image current on the detector plates. The final radius of the ion packet can be calculated according to equation 1-8:

$$r = E_{ex}t/2B \qquad (1\text{-}8)$$

In this equation E_{ex} is the RF voltage applied on the excitation plates, t is the excitation time and B is the magnetic field strength. Equation 1-8 shows that the

cyclotron orbit radius is not related to the m/z value. That is to say all the ions can be excited to the same orbit radius with a constant excitation amplitude and duration in the same ICR cell. Under low-pressure conditions, the probability of ion-neutral collisions is very small, thus the coherent cyclotron motion will damp very slowly.

The two opposite detector plates, which are connecting by a resistor, can detect the oscillating image current induced by the packet of rotating ions. The image current (Equation 1-9) is then amplified and digitized to give a time domain signal. This time domain signal is stored in a computer and subsequently Fourier-transformed to produce the frequency domain signal, which can be converted to a m/z spectrum by using equation 1-4.

$$I(t) = (Nq^2r/md) \sin \omega t \qquad (1\text{-}9)$$

In the above equation, N is the number of ions, r is the ion cyclotron radius, d is the ICR cell radius, and t is time.

Usually, we would like to get the m/z ratio information for all the ions in the ICR cell, so we have to excite the ions with a RF pulse comprising multiple frequencies. There are several types of excitation strategies featuring different advantages and disadvantages. Figure 1.6 compares these excitation schemes. Impulse excitation was used in the early development stage of FTICR for broad range m/z excitation. Later, chirp excitation became more commonly used. Stored waveform inverse Fourier transform (SWIFT) excitation has become more and more popular since it was invented by Marshall's group[9-11] in 1985, because SWIFT is believed to have the greatest power uniformity as a function of frequency and yields the greatest frequency

resolution.

The function of ion excitation in the ICR cell is not only exciting ions coherently to detectable radii, but also increasing ion kinetic energy above the collision-activated dissociation threshold or ejecting the ions from the ICR trap.

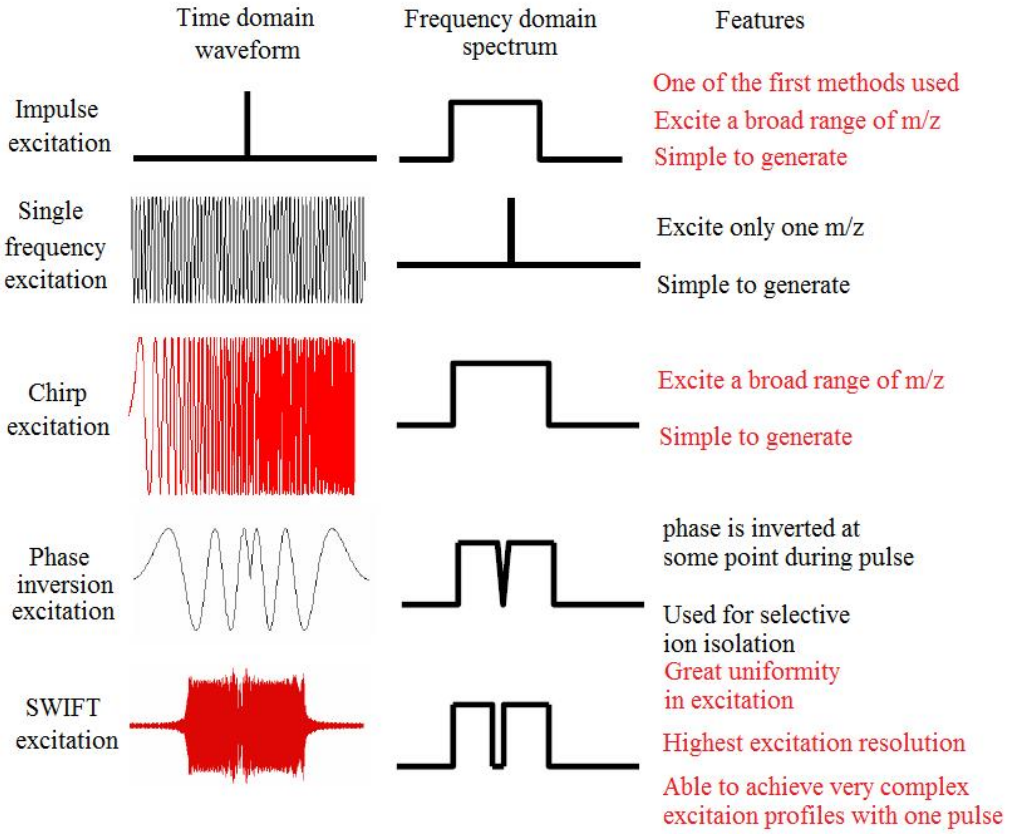

Figure 1.6: Several types of excitation schemes used in FTICR-MS[12]

General FTICR-MS sequence. Mize et al. say that FTICR-MS is a complete ion laboratory by itself.[13] The instrument can accomplish ion formation, ion injection, ion selection, ion reaction, ion dissociation, continuous ion reaction and dissociation, ion excitation, ion detection and data analysis step by step (see figure 1.7). The ICR cell has the capability of trapping ions for a long time and of doing multi-stage ion reaction and dissociation. The particular feature above makes FTICR-MS an

important method in structural analysis of large biomolecules and in delicate separation of extremely complex mixtures.

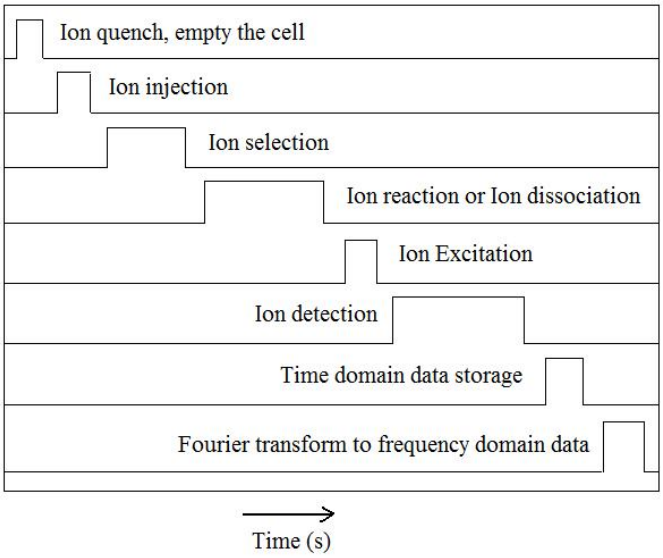

Figure 1.7: A general FTICR-MS sequence comprising time-separated events

FTICR-MS instrumentation

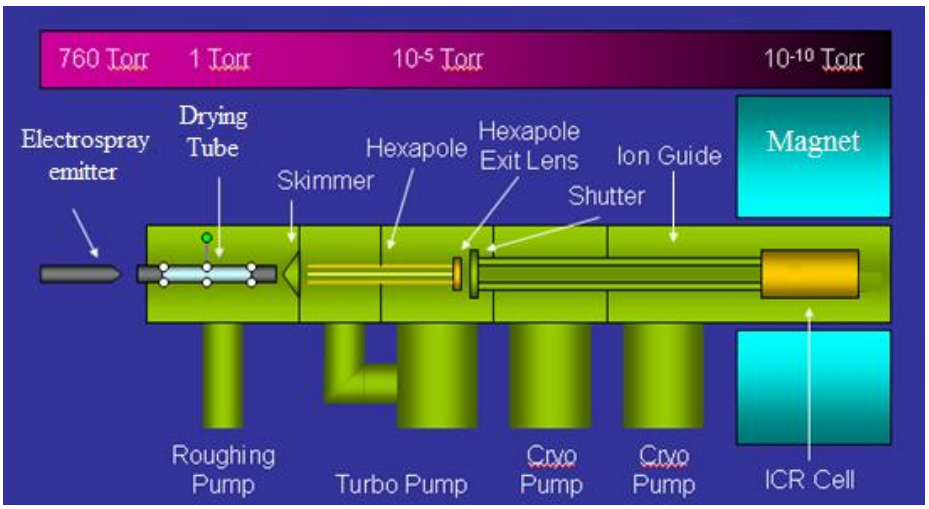

Figure 1.8: The schematic of a general FTICR-MS instrument[8]

Similar to other kinds of mass spectrometry, FTICR-MS also includes the following parts: ionization source, ion guide optics, mass analyzer (ICR cell in a high field magnet) and data analysis device. Most if not all modern FTICR-MS instruments

utilize an external ionization source to generate gas phase ions, which means the ions have to travel from atmospheric pressure to the very low pressure (10^{-9} mbar) required for optimal mass analysis. Therefore, a differential pumping system is another essential part that will be introduced here. Figure 1.8 shows a schematic of a general FTICR-MS instrument. Next, these essential parts will be described in more detail.

Ionization sources. Ionization techniques greatly influence what types of samples can be analyzed by mass spectrometry. For example, some nonvolatile samples can only be transferred to gas phase ions by a particular ionization method. All of the ionization methods applied to FTICR-MS can be classified into two types: internal ionization and external ionization.

Internal ionization is so called because the ionization process happens inside the magnet. In the early stage of FTICR-MS development, internal ionization dominated the FTICR-MS instrument due to its simplicity. The ions do not have to travel a long way to pass the magnet fringe field, thus the ion loss is quite small. Besides, there is no need to have the ion guide and differential pumping system for an internal ionization instrument. However, internal ionization is only applicable to volatile compounds. Volatile samples can be leaked into the trap through a valve, and less volatile substances are placed on a probe surface adjacent to the trap and then heated to vaporize the sample. Next, the sample vapor is ionized in situ by electrons, ions or photons. Electron ionization (EI), chemical ionization (CI) and photoionization (PI) are common internal ionization techniques.[14, 15] In the EI method, energetic electrons (typically 70 eV) interact with gas phase atoms or molecules to generate ions. Due to

the high energy electrons, the ionization process frequently breaks the molecules into fragment ions, which can reveal the structure of the analyte. This technique is particularly suitable for volatile organic samples. Chemical ionization is a lower energy process than EI. Positive or negative ions are produced by the collisions between neutral analyte and reagent ions. The lower energy process gives rise to less fragmentation, so we usually observe molecular ions with this technique, or, often, pseudomolecular ions which are composed of molecular ion and a cation.

With the requirement of examining nonvolatile samples, external ion sources became more and more popular to couple with FTICR-MS. Electrospray ionization (ESI, demonstrated by John Fenn[16, 17]) and matrix-assisted laser desorption/ionization (MALDI, first introduced in 1987[18]) are two common external ionization techniques used in FTICR-MS instruments. Herein, the ionization process happens outside the solenoidal ICR magnet, so the generated ions need to travel through some kind of ion guide to reach the ICR trapping cell. Meanwhile, a differential pumping system is required to guarantee a pressure drop from the high pressures used in the source to the 10^{-9} mbar or lower pressures required in the trap. Although more complex, ion guides and differential pumping both work well for systems where external ion sources are coupled with FTICR-MS.

ICR trapping cell. The heart of the FTICR-MS instrument is the ICR trapping cell, where ion storage, ion selection, ion reaction or dissociation and ion anlysis all take place. With the advent of FTICR, ICR performance has been limited not by the homogeneity of the magnetic field, but by the shape of the electric potential (both D.

C. and R. F.) in the ICR trapping cell.[19] After ions are injected into the cell, their cyclotron motion in the x-y plane is confined by the spatially homogenous and axially directed (z direction) magnetic field. The ion motion along the magnetic field direction is restricted by a d.c. electric potential.

There are many types of ICR cell geometries with different electrical configurations. However, these cells can be classified into two categories: closed cells and open cells. In closed cells, grids or plates are used to apply the axial electric field for trapping ions axially.

When ions are generated by an external ion source, their radial distribution might be large after they pass through the ion guide, so it is better to use an open-ended trap to avoid ion loss. In open cells, the most common geometry is cylindrical. The cell is axially segmented into three parts to function as different ring electrodes. The central ring is employed for excitation and detection. R.F. potential is applied on the central ring. D. C. potential is applied on the terminal rings to trap ions axially in the cell.

There are three common electric potentials for an ICR trap. The first is a three-dimensional axial quadrupolar potential for ion trapping. The second is a two-dimensional azimuthal quadrupolar RF potential used for axialization. The third is a one dimension azimuthal dipolar RF for ICR excitation and detection. Marshall's group has shown the likelihood that any of the three electric potentials can be obtained by appropriate segmentation of a cubic trap.[19] They applied a specific voltage independently to each segment of the cell, so they could construct near-perfect performance in all three electric potential modes without being limited by a single

ICR cell configuration.

Magnet. The super conducting solenoidal magnet is the most costly part in a FTICR-MS instrument. Liquid helium is used as a coolant for most superconductive magnets. To prevent the helium from boiling away, the magnet and liquid helium are surrounded with an outer jacket containing (significantly cheaper) liquid nitrogen (b.p. = 77 K). Superconducting magnets can produce an elongated homogenous magnetic field region with an inner diameter of 150-220 mm. Therefore it is possible for the magnet to contain a large trap cell, which decreases the space charge effect within the ion trap and improves the dynamic range of the instrument.

The strength of the magnetic field influences the performance of FTICR-MS in many aspects. Mass resolving power, quadrupolar axialization efficiency, data acquisition speed and upper mass limit for peak coalescence increase linearly with increasing magnetic field strength B.[4] Maximum ion kinetic energy, upper mass limit due to trapping potential, maximum number of trapped ions, and maximum ion trapping duration increase quadratically with increasing B. Magnetic field strength in FTICR-MS instrument has developed from 1.4 T in the mid 1960s to 21 T today.[4, 5]

Differential pumping system. In the excitation and detection step, ultra low pressure in the ICR cell is necessary for the instrument to get high resolving power and mass accuracy, because collisions between the neutral gas molecules and the desired ions will dephase the ions or cause the ions dissociate, so the signal is heavily destroyed. Due to more and more frequent use of external ion sources, the pressure drop in the FTICR instrument is quite large, usually from 1 atm to 10^{-8} – 10^{-9} Torr.

Therefore, 3 to 4 differential pumping stages are needed to fulfill this requirement. People usually choose cryo pumps or turbo pumps for FTICR-MS instruments, because their high pumping capacity (10^4 - 10^5 liters/sec) can easily achieve ultra-high vacuum or quickly pump down back to low pressure after a reaction step, which is carried out in relatively high pressure.

FTICR-MS performance

Now I will introduce some common parameters used to describe the working performance of FTICR-MS instruments.

Mass resolving power. FTICR-MS becomes a powerful technique in dealing with complex mixtures because it can distinguish two ions of similar mass-to-charge ratio as two distinct ions. The mass resolving power is defined in equation 1-10.

$$R_p = m / \delta m = qB\tau / 2m \qquad (1\text{-}10)$$

Herein, τ is the signal decay constant, m designates the mass and δm is the peak width necessary for separation at mass m. The value of δm is measured at a specified fraction of the peak height, for example 0.5%, 5% or 50%. The last is called the full width at half maximum (FWHM). Resolving power is usually a large number, for example: FT-ICR-MS's world record for highest resolving power is 200,000,000 for singly-charged $^{40}Ar^+$ at FWHM.[20]

Equation 1-10 shows that high resolving power can be obtained by increasing magnetic field strength and data acquisition time (τ is the signal decay constant). In a single mass spectrum, mass resolving power for ions with high m/z values is smaller

than that for low m/z values.

In older publications, people prefer using "resolution" to define the instrument's resolving power. According to the most recent IUPAC orange book definition in 1991, resolution is the peak width of a spectral peak expressed as δm at m.

Mass accuracy. Many applications of FTICR-MS use mass accuracy to help determine the composition of molecules based on accurate mass. Mass accuracy indicates the relative deviation of the instrument response from a known monoisotopic calculated mass, and is expressed in parts per million (ppm).

$$\text{Mass Accuracy (ppm)} = \left| m_{actual} - m_{measured} \right| / m_{actual} \times 10^{6} \qquad (1\text{-}11)$$

The smaller the value, the better performance the instrument has.

The high resolving power of the FT-ICR instrument does not guarantee the mass accuracy of the measurement. As with other mass spectrometric methods, systematic effects can produce deviations between measured and calculated mass values. In FTICR-MS, we obtain high mass accuracy by accurately determining the ion cyclotron frequency. Basically, perturbation of the cyclotron frequency is caused by radial electric fields and space charge effects. The magnetic field inhomogeneity in super conducting solenoidal magnets is not a significant factor for perturbation of ion cyclotron frequency.[28]

Amster et al. published work to prove that it is necessary to accurately calculate the total ion intensity of a mass spectrum for correction of space-charge effects either by matching calibrant and analyte mass spectra or by using the calibration equation.[21]

Mass Range. When talking about the mass range of FT-ICR, we need to

consider two aspects: the lower and upper mass limits. We have already shown that the mass to charge ratio is inversely proportional to the ion cyclotron frequency, so the lower mass limit is decided by the upper limit of frequency that the detection electronics can record. The Nyquist criterion requires that the detection electronics digitizing rate must be at least twice as fast as the measured frequency. With the development of modern electronics, the frequency they can record has become higher and higher, thus the lower mass limit is no longer a significant problem. As for the upper mass limit, several parameters need to be considered, such as trap dimension, trapping potential and space charge.

It is clear that an ion has to be confined inside the ICR cell to be excited and detected, so the cyclotron radius of the ion must be less than the trap radius, d/2. The upper mass limit is given by equation (1-12):

$$m_{upper} = q^2 B^2 r_{max}^2 / 2kT \qquad (1\text{-}12)$$

In this equation, q is the charge, B is the magnetic field strength, r_{max} is the trap cell radius (d/2), k is the Boltzmann constant and T is temperature.

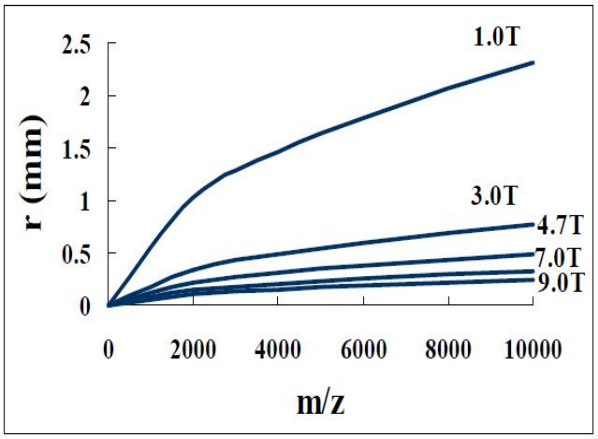

Figure 1.9: Ion cyclotron radius vs. m/z at different magnetic field strengths.[4]

Equation 1-12 indicates that upper mass limit increases quadratically with the

magnetic field strength and linearly with the trap cell diameter. The dimension of the ICR trap is decided by the size of the homogeneous region in the super conducting solenoidal magnet. Figure 1.9 depicts the relationship between the ion cyclotron radius versus the m/z at each of five representative magnetic field strengths: 1.0, 3.0, 4.7, 7.0, and 9.4 tesla at 298 K. It is clear that higher magnetic field strength can confine the same m/z ions to a smaller orbit.

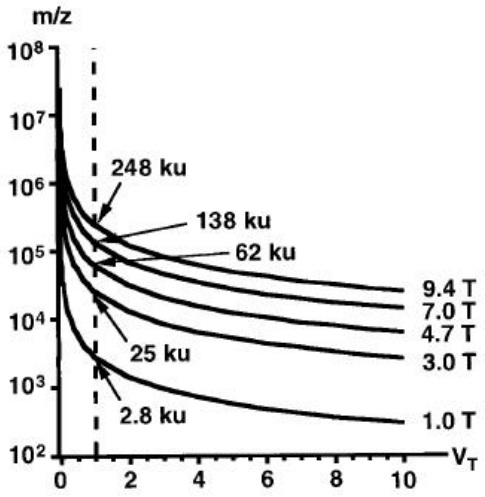

Figure 1.10: Upper mass limit of a singly-charged ion in an ICR trap at several magnetic field strengths (V_T stands for trapping voltage).[4]

The radial component of the trap electric field caused by the finite dimension of the ICR trapping cell is another factor that influences the upper mass limit. When the outward force arising from the radial electric field is stronger than the inward Lorentz force, ions will be ejected from the ICR cell. Thus, the critical mass related to trapping potential can be summarized in equation (1-13):

$$m_c = qB^2a^2 / 8V_{trap}\alpha \qquad (1\text{-}13)$$

Herein, q is the ion charge, B is the magnetic field strength, a is the cell diameter, V_{trap} is the trapping voltage, and α is a constant related to trapping cell dimensions

and geometry. Figure 1.10 shows the upper mass limit for a singly charged ion at five common magnetic field strengths: 1.0, 3.0, 4.7, 7.0, and 9.4 tesla. It also indicates the critical mass at each magnetic field strength when the trapping voltage is 1 Volt.

Space charge effects will broaden the spectral peak, thus decrease the upper mass limit.

Dynamic Range. Dynamic range is defined as the ratio of the largest to the smallest observable signal in a single spectrum.[22] The maximum number of ions that may be trapped can be estimated by space charge considerations. Space charge (Coulomb repulsion) effects tend to spread the trapped ions out in the ICR trap, reducing the coherence of the excited ICR signal and resulting in axial and radial ion loss as well as loss of signal due to charge induced on the trap electrodes rather than the detector electrodes.[22]

For typical FTICR-MS operating parameters, the detection limit is about 180 ions.[4] Compared to other types of mass spectrometry, FT-ICR-MS has a lower dynamic range of about $10^3 - 10^5$.[22] The maximum number of trapped ions may be increased by elongating or widening the trap. Another choice could be ejecting all unwanted species by SWIFT.

Some FTICR-MS applications

Electrospray Ionization. Electrospray ionization is one of the most common ionization methods coupled with FTICR-MS nowadays. I will introduce and discuss this topic in detail in chapter 3.

Tandem mass spectrometry using FT-ICR-MS. Ultrahigh mass accuracy and ultrahigh resolving power are not the only two reasons that make FT-ICR-MS a powerful analysis method in dealing with complex mixtures. Versatile tandem mass spectrometry capabilities (MS^n) carried out in the ICR trapping cell contribute a lot to FTICR-MS's structure analysis capabilities. Tandem mass spectrometry basically works in the following ways: activation of the precursor ions, dissociation or reaction, and then detection of the product ions.

The most popular method in FTICR-MS collision induced dissociation (CID) is called sustained off-resonance irradiation (SORI[23]). In the process, ions of a selected m/z are alternately excited and de-excited due to the frequency difference between the applied excitation frequency and the ions' cyclotron frequency, and then neutral molecules (generally air) are leaked into the trap cell to collide with translationally activated ions. Photodissociation has proven to be very effective in biomolecule structure characterization.[4] IR laser photons are used for "slow heating" activation, and similar fragmentations like those in CID/CAD happen in infrared multiphoton photodissociation (IRMPD[24]). Because no collision gas is applied in IRMPD, the instrument does not need to be pumped down and a high resolution detection event can quickly take place after dissociation. Blackbody infrared radiative dissociation (BIRD[25]) is an alternative to laser photodissociation. Heating the vacuum chamber produces blackbody radiation with known and controllable energy to cause quantitative slow-heating dissociation. Electron capture dissociation (ECD[26]) is very popular in protein analysis. In the process, a multiply protonated molecule interacts

with a free low energy electron, and releasing the electric potential energy results in fragmentation. ECD forms quite different types of fragment ions than other fragmentation methods such as CID and IRMPD. The unique (and complementary) fragments produced and the capability to fragment whole macromolecules effectively are very promising features in protein structure analysis.

Petroleomics. A powerful advantage of FTICR-MS over other mass spectrometry methods is ultrahigh mass accuracy. Marshall et al. have utilized this feature to analyze petroleum crude oil without any sample preparation.[27] If 1 ppm mass accuracy can be achieved, unique elemental composition can be decided directly from the measured mass. Marshall showed an example of resolving 500 singly charged ions in the range 90-300 Da.[4] Besides the mass accuracy capability, a high-magnetic field (9.4 T) and a front end mass filter were employed to extend the mass range and dynamic range, respectively, of the instrument.

Host-guest interactions in the gas phase. The FTICR cell is quite suitable for ion storage and ion reaction in the gas phase.[28] Therefore, FTICR-MS has been used in investigation of host-guest interactions to probe fundamental interactions in supramolecular chemistry. It is very convenient to compare gas phase host-guest experimental results with computational results directly because complicated solvent effects are not present in the gas phase. Our group has focused on characterization of macrocyclic molecules in the gas phase using electrospray FT-ICR-MS.[29-34] Part of my doctoral work focuses on gas phase chiral recognition,[35, 36] which I will discuss in chapters 2 and 3.

Proteomics. There are two strategies used for protein analysis.[37] The first is called the "bottom up" approach, which is performed by cleaving the protein molecules into peptide fragments through enzymatic digestion before ionization. By searching in genome sequence data bases, peptide fragments' compositions can then be identified. The other approach is "top down", which is usually carried out in FTICR-MS. The peptide can be intactly ionized, so the molecular weight could be detected. Then the peptide is broke down into fragments by tandem mass techniques, such as CID or ECD.

Technological advantages of FTICR-MS have made it possible to examine smaller and smaller amounts of larger and larger molecules.[12] The application of electrosray ionization also forms multiply charged protein molecules, so the m/z ratio is much smaller than for singly charged protein molecules. The combination of ESI and FTICR makes intact protein analysis (top-down analysis) possible. The mass for the intact protein points to post-translational modifications which are not indicated in bottom-up analysis.

References

(1) Hipple, J. A.; Sommer, H.; Thomas, H. A. *Physical Review*, **1949**, *76*, 1877 and Sommer, H.; Thomas, H. A.; Hipple, J.A. *Physical Review*, **1951**, *82*, 697.

(2) Comisarow, M. B.; Marshall, A. G. *Chem. Phys. Lett.* **1974**, *25*, 282.

(3) Marshall, A. G. *Int. J. Mass Spectrom.* **2000**, *200*, 331-356.

(4) Marshall, A. G.; Hendrickson, C. L.; Jackson, G. S. *Mass Spectrom. Rev.* **1998**, *17*,

(5) "Ion Cyclotron Resonance (ICR) Overview" on National High Magnetic Field Laboratory website.

(6) Chen, R.; Guan, S.; Marshall, A. G. *J. Chem. Phys.* **1994,** *100,* 2258.

(7) Gates, P. http://www.chm.bris.ac.uk/ms/theory/fticr-massspec.html, Last updated January 23 rd, **2004**.

(8) Guo, Y. http://www.lab.org.cn/UserFiles/FTICRMS(1).doc.

(9) Marshall, A. G.; Wang, T. C.; Ricca, T. L. *J. Am. Chem. Soc.* **1985**, *107*, 7893-7897.

(10) Goodman, S., Hanna, R.: U.S. Patent, **1986**, No. 4945234.

(11) Guan, S.; Marshall, A. G. *Anal. Chem.* **1993**, *65*, 1288-1294.

(12) Dearden, D. V. FT-ICR-MS Tutorial Presentation.

(13) Heeren, R. M. A.; Kleinnijenhuis, A. J.; McDonnell, L. A.; Mize, T. H. *Anal. Bioanal. Chem.* **2004**, *378*, 1048-1058.

(14) Irion, M. P.; Bowers, W. D.; Hunter, R. L.; Rowland, F. S.; McIver, R. T., Jr. *Chem. Phys. Lett.* **1982**, *93*, 375-379.

(15) Ghaderi, S.; Kulkarni, P. S.; Ledford, E. B.; Wilkins, C. L.; Gross, M. L. *Anal. Chem.* **1981**, *53*, 428.

(16) Yamashita, M.; Fenn, J. B. *J. Phys. Chem.* **1984**, *88*, 4451-4459.

(17) Yamashita, M.; Fenn, J. B. *J. Chem. Phys*. **1984**, *88*, 4671-4675.

(18) Karas, M.; Bachmann, D.; Bahr, U.; Hillenkamp, F. *Int. J. Mass Spectrom. and Ion Proc.* **1987**, *78*, 53.

(19) Guan, S.; Marshall, A. G. *Int. J. Mass Spectrom. and Ion Proc.* **1995**, *146/147*, 261-296.

(20) Bamberg, M.; Allemann, M.; Wanczek, K-P. *Proceedings of the 35th American Society for Mass Spectrometry Annual Conference on Mass Spectrometry and Allied Topics* **1987**, 1116–1117.

(21) Easterling, M. L.; Mize, T. H.; Amster, I. J. *Anal. Chem.* **1999,** *71*, 624-632.

(22) Limbach, P. A.; Grosshans, P. B.; Marshall, A. G. *Anal. Chem.* **1993,** *65*, 135-140.

(23) Gauthier, J. W.; Trautman, T. R.; Jacobson, D. B. *Anal. Chim. Acta* **1991**, *246*, 211-225.

(24) Little, D. P.; Chorush, R. A.; Speir, J. P.; Senko, M. W.; Kelleher, N. L.; McLafferty, F. W. *J. Am. Chem. Soc.* **1994**, *116*, 4893-4897.

(25) Dunbar, R. C.; McMahon, T. B. *Science* **1998**, *279*, 194-197.

(26) Xu, L. X.; Huang, Y. L.; Giese, R. W. *J. Mass Spectrom.* **1998**, *33*, 615-620.

(27) Marshall, A. G.; Rodgers, R. P. *Acc. Chem. Res.* **2004**, *37*, 53-59.

(28) Zhang, H. *Doctoral dissertation submitted to Brigham Young University*, **2006**.

(29) Dearden, D. V.; Chu, I.-H. *J. Incl. Phenom. Mol. Recognit. Chem.* **1997**, *29*, 269-282.

(30) Kellersberger, K. A.; Dejsupa, C.; Liang, Y.; Pope, R. M.; Dearden, D. V. *Int. J. Mass Spectrom.* **1999**, *193*, 181-195.

(31) Liang, Y.; Bradshaw, J. S.; Izatt, R. M.; Pope, R. M.; Dearden, D. V. *Int. J. Mass Spectrom.* **1999**, *185/186/187*, 977-988.

(32) Shen, N.; Pope, R. M.; Dearden, D. V. *Int. J. Mass Spectrom.* **2000**, *195-196*, 639-652.

(33) Dearden, D. V.; Liang, Y.; Nicoll, J. B.; Kellersberger, K. A. *J. Mass Spectrom.* **2001**, *36*, 989-997.

(34) Zhang, H.; Paulsen, E. S.; Walker, K. A.; Krakowiak, K. E.; Dearden, D. V. *J. Am. Chem. Soc.* **2003**, *125*, 9284-9285.

(35) Fang, N.; Dearden, D. V. In *54th ASMS Conference on Mass Spectrometry and Allied Topics*; ASMS: Seattle, WA, **2006**.

(36) Fang, N.; Dearden, D. V. *"Equilibrium Methods for Characterizing Gas Phase Chiral Recognition," in Chiral Recognition in the Gas Phase, Zehnacker-Rentien, A., ed.; Taylor & Francis: London, 2010.*

(37) Bogdanov, B.; Smith, R. D. *Mass Spectrom. Rev.* **2005**, *24*, 168-200.

Chapter 2

The Roles of Hydrogen Bonding and π Stacking in Gas Phase Chiral Recognition

Introduction

Since chirality was first observed by Jean-Baptiste Biot in 1815, chirality has been found built into all living things. Many biologically active molecules are chiral, including the naturally occurring amino acids (the building blocks of proteins), sugars and enzymes. Chirality also needs to be build into many synthetic drugs (for example, see figure 2.1) because these drugs are designed to work with chiral biomolecules. In many cases, drugs are being marketed as single enantiomers because only one enantiomer is therapeutically effective whereas the other enantiomer may even be harmful.[1]

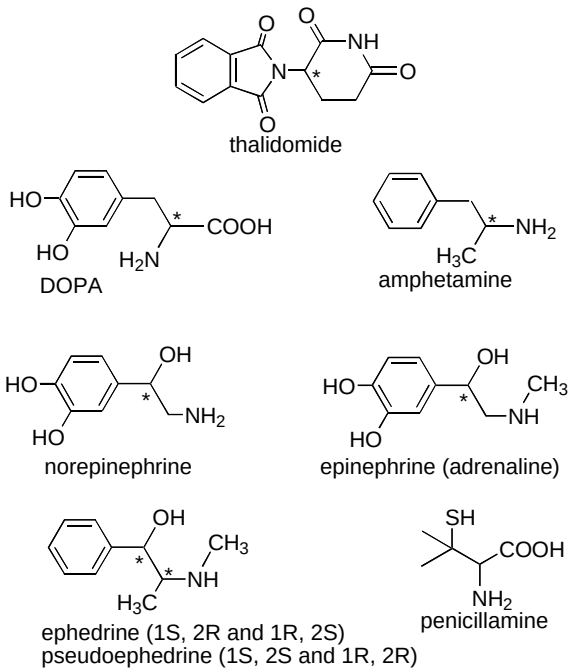

Figure 2.1: Some synthetic chiral drugs.[1]

Due to the increasing application of chiral molecules, a critical need has developed for analytical methods for characterizing chiral species. Currently, NMR, chromatographic, and spectroscopic techniques play an important role in enantiomeric analysis. However, none of these techniques satisfy all of the requirements (easy sample preparation, minimal matrix effects, high sensitivity to enantiomeric excess, rapidity and small sample amount) of an ideal analytical method. Mass spectrometry, although it does not inherently distinguish between enantiomers, has been applied by a number of groups to probe enantiodiscrimination, and shows promise as a method for enantiometric analysis.

The chiral recognition using mass spectrometry done by Sawada et al. involves reaction between a chiral analyte and a racemic mixture in which one of the enantiomers is isotopically labeled.[2] The difference in peak intensities of the resulting diastereomeric complexes allows measurement of the enantiomeric excess in the analyte. The most crucial disadvantage of this method is that it requires one of the enantiomers to be isotopically labeled. Another approach developed by Lebrilla et al.[3] is based on the fact that enantiomers bound to chiral cyclodextrins are replaced by other achiral compounds at different rates. This method is experimentally sound, but the complexes are too large to easily apply accurate computational methods to understand the mechanism of chiral recognition in these systems. Currently, the most promising mass spectrometric method utilized in chiral recognition is probably that developed by Cooks et al.[4] They generate a complex composed of analyte, a transition metal ion, and a neutral chiral reference ligand. The fragmentation patterns

generated by collision-induced dissociation (CID) of the resulting diastereomeric complexes reveal the abundance of the two enantiomers in the analyte. This method is fast, and it works well with a small amount of sample. However, the mechanism underlying this method is unclear, so it is hard to optimize the metal ion and reference ligand to obtain optimum sensitivity. Another study recently reported by Speranza et al.[5] investigated the proton-bound complexes between amino acids and a chiral amido[4]resorcinarene receptor. A guest-exchange reaction was observed that exhibits a distinct enantioselectivity with regard to both the leaving amino acid and the amine reactant. These authors determined the enantioselectivity by measuring the rate constants for the exchange reactions involving the two enantiomers.

Our group has studied gas phase chiral recognition using mass spectrometry for more than 10 years.[6,7] We have previously shown that measurement of amine exchange equilibria is a powerful way to evaluate the degree of chiral recognition.[6, 7] We introduce the two enantiomers into a chiral environment, because only in a chiral environment can the differences between enantiomers become apparent. We are interested in gas phase studies of fundamental interactions because the gas phase avoids complications and masking effects that may arise upon solvation. Therefore, the intrinsic interactions between the species of interest are directly shown in the experimental results. In addition, the results of gas phase experiments can be directly compared with those of high-level computational studies, where the molecular system is isolated as in the gas phase.

The products of enantiomers binding to a chiral neutral molecule are

diastereomers, which have different chemical and physical properties and therefore can be distinguished. The product diastereomers may appear in the mass spectrum with different intensities, which are influenced by the abundances of the analyte enantiomers, reaction rates, dissociation rates or equilibrium constants for exchange reactions.[1, 8] Because we are applying equilibrium techniques, our results directly yield free energy differences that measure the extent of chiral recognition in the system. In order to achieve and characterize equilibrium reactions, we have to find equilibrium reactions with proper reaction rates: neither too slow nor too fast. Slow reactions mean the ions trapped in the ICR cell will take a long time to reach equilibrium, and ion losses during the process result in weak signal. If the reactions are too fast, both of the enantiomers may react with the neutral very quickly, making the difference in equilibrium constants hard to observe. Therefore, we try to carefully choose an appropriate neutral species that has suitable vapor pressures for the equilibrium experiment. While previous work in our group has shown that equilibrium methods can be successfully applied to analytical determination of enantiomeric excess,[9] equilibrium techniques are much better suited to probing the underlying factors responsible for chiral recognition than they are to analytical work. Our goal is elucidating enantiodiscrimination mechanisms rather than the direct development of analytical protocols. We hope that our work will lay the foundation necessary for improved analytical methods.[1]

Both of the two host molecules studied here have two stereo centers and a crown ether chain in their structure, whereas the π system sizes are different (Figure 2.2). As

for the guests, we select a series of aromatic chiral amines with different sizes of π system, different electron densities in the aromatic ring, or different numbers of hydrogen bonds (Figure 2.3).

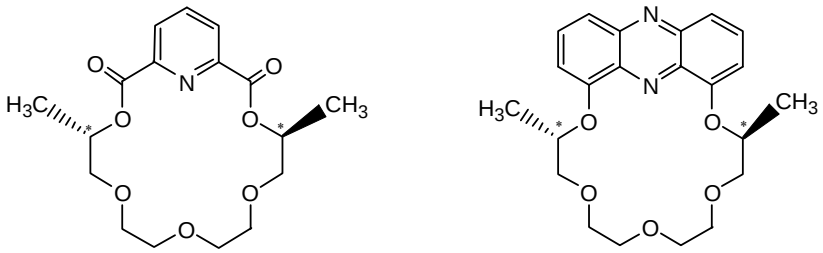

Dimethyldiketopyridino-18-crown-6 Dimethylphenazino-18-crown-6

Figure 2.2: Chiral hosts 1 (left) and 2 (right)

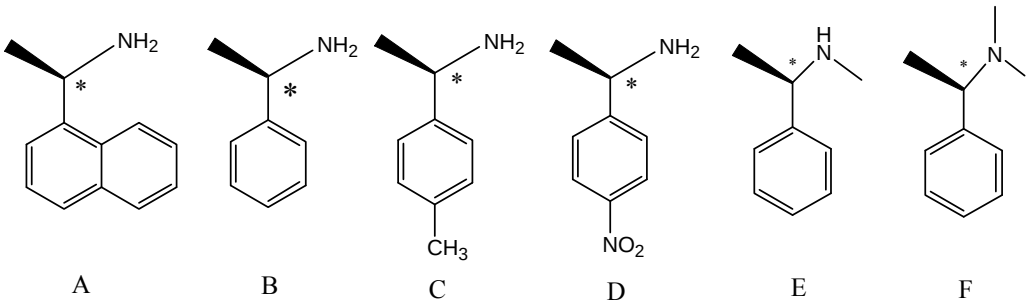

A B C D E F

A: *(R)*-α(1-naphthyl)ethylamine D: *(R)*-nitrobenzylamine

B: *(R)*-1-phenylethylamine E: *(S)*-N, α-dimethylbenzylamine

C: *(R)*-(+)-α,4-dimethyl-benzylamine F: *(S)*-N,N-dimethyl-1-phenethylamine

Figure 2.3: Chiral amine guests

Experimental Section

Instrument. A commercial Fourier transform ion cyclotron resonance mass spectrometer (model APEX 47e, Bruker Daltonics, Billerica, MA) was used in all experiments. High vacuum is provided by one stage of mechanical pumping and an

additional stage of turbopumping followed by three regions of differential cryopumping (Edwards). The base pressure in the trapping cell is typically 1×10^{-9} mbar. The mass spectrometer is coupled with a modified commercial electrospray ionization source (model 10413; Analytica, Branford, MA) operated at atmospheric pressure. We replaced the 34-gauge stainless steel spray capillary with a 50 μm i.d. fused silica capillary having a tapered tip and replaced the manufacturer's glass capillary vacuum interface with a heated type 316 stainless steel desolvating tube (0.0625 in. o.d. × 0.020 in. i.d.). Via a zero dead volume union (Valco, Houston, TX), the spray capillary was coupled to Teflon tubing, which was in turn friction fit to a syringe needle containing the sample solution. Generally, the voltage applied to the spray needle is about 1.5 kV, and the spray flow rate is about 15 μL/h. Ion injection into the trapping cell is carried out via electrostatic focusing of the ion beam along the magnetic field axis. The temperature in the trapping cell is always at ambient temperature (about 300 K). MIDAS is the software that controls the sequence of each experiment.[9,10] Stored waveform inverse Fourier transform (SWIFT) methods were used to isolate the target ions.[11,12]

Materials. Host molecules **1** and **2** were produced according to published procedures.[13,14] Cyclohexylamine (97.9%) was purchased from Fisher. *(R)*-α(1-naphthyl)ethylamine (99%) and *(R)*-1-phenylethylamine (>99%) were purchased from Aldrich, while *(S)*-N, α-dimethylbenzylamine (>98%), *(R)*-nitrobenzylamine (>98%), *(R)*-(+)-α,4-dimethyl-benzylamine (>98%), *(S)*-N,N-dimethyl-1-phenethylamine (>98%) and 4-methylbenzylamine (>97%) came

from Fluka. All compounds were used as supplied, with the exception that they were degassed through several freeze-pump-thaw cycles prior to introduction into the vacuum system.

Theory. In a typical experiment, one enantiomer of the target chiral amine and an achiral reference amine were introduced into the ion-trapping region of the vacuum chamber. Volatile samples were introduced through precision variable leak valves (Varian, Palo Alto, CA), while less volatile amines were introduced via a direct-exposure sample vacuum lock. In most experiments, 4-methylbenzylamine was used as the achiral reference. For *(R)*-α(1-naphthyl)ethylamine and *(R)*-1-phenylethylamine, cyclohexylamine served as a better reference because its affinity for the ligand is more similar to that of the target chiral amine than is that of 4-methylbenzylamine. Following the degassing procedure, the partial pressures of each amine were easily stabilized and were measured using a cold cathode ionization gauge (Balzers). We assume that the gauge has similar response to the chiral and achiral amines, although ultimately the results are not sensitive to the absolute values of the pressures and the gauge is used primarily to ensure that pressures remain constant over time during the experiments.

Typically, the concentration of the host sample was 10 μM in 80:18:2 methanol: water:acetic acid solution. One enantiomer of the chiral host was introduced into the instrument using electrospray [(*R, R*)-1, for example], and the protonated host ions were captured in the trapping cell, where the reaction between the host ions and the neutral amines took place. The chiral amine and the achiral reference amine each

reacted with the protonated host to generate ammonium complexes, and the exchange of the two amines on the host reached equilibrium under favorable conditions. The experiment was then repeated by flushing the electrospray source and spraying the other host enantiomer [(*S, S*-1)].

The reactions used in measuring enantiodiscrimination are summarized here (host 1 is dimethyldiketopyridino-18-crown-6):

$$(R)\text{-amine}\bullet(R,R)\text{-}1H^+ + \text{Ref} \rightleftharpoons \text{Ref}\bullet(R,R)\text{-}1H^+ + (R)\text{-amine} \quad (1)$$

$$\text{Ref}\bullet(S,S)\text{-}1H^+ + (R)\text{-amine} \rightleftharpoons (R)\text{-amine}\bullet(S,S)\text{-}1H^+ + \text{Ref} \quad (2)$$

$$\text{Ref}\bullet(S,S)\text{-}1H^+ + (R)\text{-amine}\bullet(R,R)\text{-}1H^+ \rightleftharpoons (R)\text{-amine}\bullet(S,S)\text{-}1H^+ + \text{Ref}\bullet(R,R)\text{-}1H^+ \quad (3)$$

Both reaction 1 and 2 were carried out in the "forward" and "reverse" directions to verify that equilibrium was obtained. In reaction (3), which is the sum of reactions (1) and (2), Ref • (*S,S*)-$1H^+$ and Ref • (*R,R*)-$1H^+$ are enantiomers, so their thermochemical values are the same, whereas *(R)*amine • (*R,R*)-$1H^+$ and *(R)*amine • (*S,S*)-1 H^+ are diastereomers. Therefore, reaction 3 measures the enantiodiscrimination of host 1 for the chiral amine by measuring the thermochemical difference between the diastereomers.

The extent of the enatiodiscrimination is the free energy of reaction 3, which equals the difference between the free energy changes in reactions 1 and 2, respectively. This is shown in equation 2-1 as follows:

$$\Delta\Delta G^\circ_R = \Delta G^\circ_{R,R\cdot R} - \Delta G^\circ_{S,S\cdot R} = -RT\ln(K_{R,R\cdot R}/K_{S,S\cdot R})$$

$$= -RT\ln(I_{R,R\cdot R}\, I_{S,S\cdot R}/I_{R,R\cdot Ref} I_{S,S\cdot Ref}) \quad (2\text{-}1)$$

In equation 2-1, R and T are the ideal gas constant and absolute temperature, respectively. $K_{R,R\cdot R}/K_{S,S\cdot R}$ is the ratio of equilibrium constants for reactions 1 and 2. $I_{R,R\cdot R}$, $I_{S,S\cdot R}$, $I_{R,R\cdot Ref}$, and $I_{S,S\cdot Ref}$ are mass spectral intensities of the relevant complex peaks in reactions 1 and 2. We monitor the total pressure during the experiment, because it is essential to maintain constant partial pressures of the chiral amine and the achiral reference amine during the forward and reverse reactions for both host enantiomers, so the pressures can be canceled in reaction 3.

For the secondary amine and the tertiary amine, the system takes a relatively long time to reach equilibrium. Therefore, we determined the equilibrium constant by measuring the rate constants of the forward and backward reactions instead of directly measuring the product / reactant ratio at equilibrium (equations 2-2 and 2-3). We collected enough data at short reaction times to make sure the kinetic fit gave accurate rate constants.

$$K_{R,R\cdot R} = k_{forward\text{-}1}/k_{reverse\text{-}1} \quad (2\text{-}2)$$

$$K_{S,S\cdot R} = k_{forward\text{-}2}/k_{reverse\text{-}2} \quad (2\text{-}3)$$

Computational Methods. As for the computational methods, we usually start the calculation with Monte Carlo conformational searches with a molecular mechanics force field, and then subject the lowest-energy conformations found in the conformational search as the starting points for *ab initio* geometry optimization. We conduct conformational searches using the Macromodel package (Schrödinger, Inc.;

Portland, OR). We use both the AMBER*[15] and MMFF94[16-20] force fields supplied with Macromodel.

We set up and manage all of the higher-level calculations using the ECCE package (Pacific Northwest National Laboratory; Richland, WA) and use either the Gaussian 98 (Gaussian Inc.; Pittsburgh, PA) or NWChem (Pacific Northwest National Laboratory) computational engines to carry out the calculations.[1]

Results and Discussion

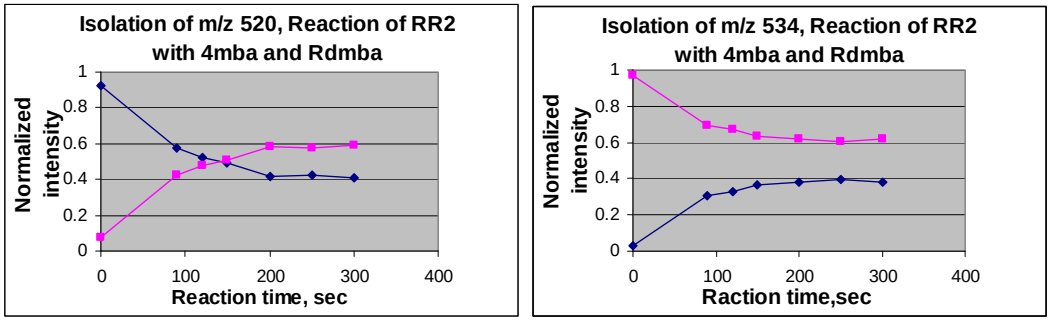

Figure 2.4: Approach to equilibrium in the exchange reaction of 4-methylbenzylamine (achiral reference) and (R)-(+)α,4-dimethylbenzylamine on chiral host 2. The pink dots represent the chiral amine complex (m/z 534), and the blue dots represent the achiral amine complex (m/z 520).

Figure 2.4 shows the approach to equilibrium for host (*R, R*)-2 and *(R)*-(+)-α,4-dimethyl-benzylamine. The left graph shows that the achiral amine (4-methylbenzylamine) complex (*m/z* 520) was isolated at the start, and the reaction goes forward to form more chiral amine complex (*m/z* 534) until the reaction reached equilibrium. The right graph shows the approach to equilibrium from the reverse

direction. We measured the ratio of the $I_{R,R\cdot R}/I_{R,R\cdot Ref}$ from the two sets of experiments and took the average value, which is used in equation 2-1. Then we followed the same experimental sequence for the other host enantiomer, (*S, S*)-2, to determine the $I_{S,S\cdot R}/I_{S,S\cdot Ref}$ value for use in equation 2-1.

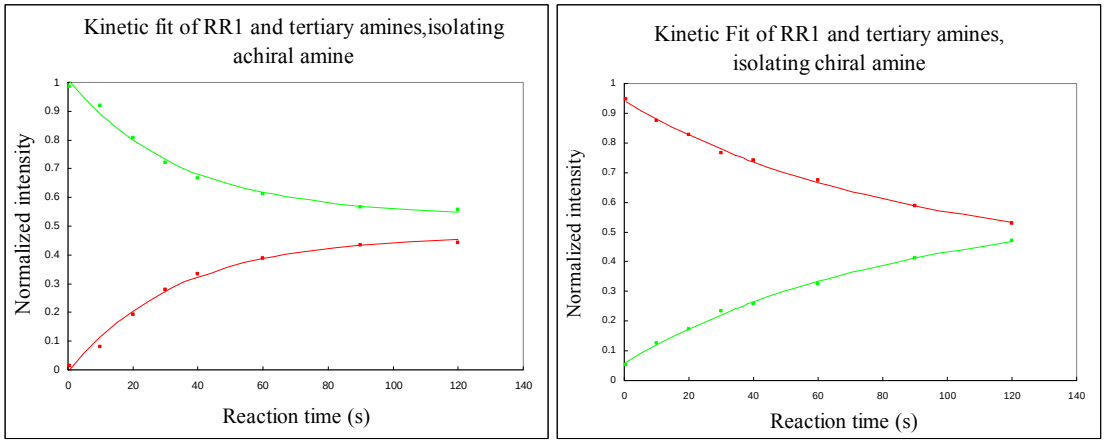

Figure 2.5: Kinetic fit results for (*R,R)*-1 and tertiary amines. The red dots represent the chiral amine complex (m/z 503), and the green dots represent the achiral amine complex (m/z 489).

Figure 2.5 shows the approach to equilibrium for a slow reaction. Here, we do not directly observe equilibrium because the long reaction times required result in very weak signals. In this case we determined the equilibrium constant from the ratio of the rate constants for the forward and reverse reactions, respectively.

Comparing the free energy changes, it is evident that π stacking is one of the main factors influencing enantiodiscrimination. In both host 1 and host 2, larger π systems in the guest result in better chiral recognition. However, if we keep the π system size the same in the guest molecule and increase the π system size in the host, we obtain decreased chiral recognition. These results suggest that the function of the π system in

the guest and host is different. A more extensive π system in the guest favors chiral recognition probably because it increases the binding affinity and brings the chiral centers closer together.

Table 2-1: Chiral recognition data in the host 1 system

Chiral amine	△△*G*°, kJ mol^{-1}
(R)-1-phenylethylamine	-2.4±0.5
(R)– α (1-naphthyl)ethylamine	-3.5±0.6
(R)-(+)- α ,4-dimethyl-benzylamine	-4.5±0.5
(S)-N, α-dimethylbenzylamine	-0.9±0.2
(S)-N,N-dimethyl-1-phenethylamine	-0.8±0.2

Table 2-2: Chiral recognition data in the host 2 system

Chiral amine	△△*G*°, kJ mol^{-1}
(R)-1-phenylethylamine	-1.2±0.4
(R)- α (1-naphthyl)ethylamine	-2.4±0.5
(R)-(+)- α ,4-dimethyl-benzylamine	-1.4±0.5

However, increasing the π system in the host from one to three aromatic rings decreases the degree of enantiodiscrimination. The reason for this is not entirely clear, but it is possible that the large planar area of the 3-ring π system flattens the potential energy surface sufficiently that there is a great deal of flexibility in guest binding. If this is the case, close proximity of the host and guest chiral centers upon binding might not be required, decreasing the possible amount of

enantiodiscrimination even if the overall binding affinity increases.

For host 1, methyl substitution on the chiral guest makes the enantiodiscrimination greater by about 2 kJ mol^{-1}. Methyl is an electron-donating substituent, so methyl substitution should increase the electron density in the π system. Higher electron density in the aromatic ring strengthens the host-guest π stacking interaction, leading to greater enantiodiscrimination.

We had hoped to further test the effect of π system electron density by examining a chiral benzylamine guest with an electron-withdrawing nitro substituent. However, *(R)*-nitrobenzylamine barely reacts with any of the tested hosts. The nitro group decreases the electron density of the aromatic ring in the guest. It is possible that this leads to much weaker host-guest affinity than for the unsubstituted guest, such that the host and guest do not bind strongly enough for us to observe. Perhaps a more likely possibility is that *(R)*-nitrobenzylamine's vapor pressure is too low for observable reaction rates within the time frame of our experiments.

For host 2, the effect of increasing electron density in the guest π system via methyl substitution is negligible with respect to experimental error. We speculate that the large π system of host 2 allows enough flexibility in the complex that addition of electron density to the π system does not enhance enantiodiscrimination.

Hydrogen bonding is another significant factor that influences host-guest affinity. Compared to the primary amine, we expect the secondary amine and tertiary amine to have weaker binding with the hosts, because as more H atoms are replaced by alkyl groups, the number of hydrogen bonding interactions between the host and guest

decreases. The experimental data indicate that host 1 has worse chiral recognition for the secondary amine and tertiary amine than for the primary amines. I also attempted to study complexes of host 2 with tertiary amines; however, the signal of their complexes was too weak to be isolated for further reaction.

Compared to chiral recognition results measured in methanol and other solvents, we find that the degree of recognition is greater in the gas phase than in solution for both host 1 and host 2 (see data in table 2-3).

Table 2-3: Free energy comparison between solution phase[20] and gas phase

	$\Delta\Delta G°$, kJ mol-1	(Guest: naphthylethylamine)
Host	Gas Phase	Solution
1	-3.5 ± 0.6	-2.4 (CH_3OH)
2	-2.4 ± 0.5	-0.4 (1:1 CH_3OD:$CDCl_3$)

Computational methods were also applied to elucidate the intermolecular interactions. Our goal was to test whether the calculations correctly predicted the enantiodiscrimination, and to determine what intermolecular interactions were responsible. We computationally examined the π–π angle, the ring-ring distance, and the H-O bond distances in the complexes (see data in table 2-4). The π-π angle is the angle between the planes of the aromatic rings in the host and guest. The ring-ring distance is the distance between the two centers of the aromatic rings in the host and guest. The H-O bond distance is the average value of the hydrogen bond lengths in the host-guest complexes.

If π-π stacking were important, we would expect the π-π angle to be close to zero and the ring-ring distances to be small. If H-bonding is more important, we would expect the H-bond lengths to be less for the favored complexes.

Table 2-4: Computational data for host 1

Complex	π-π angle	ring-ring distance	H-O bond distance
SSR- phenylethylamine	27.05	4.7863	2.010
SSS- phenylethylamine	22.06	4.3428	2.112
SSR- naphthylethylamine	25.43	4.3504	2.015
SSS- naphthylethylamine	20.02	4.1094	2.114

The π-π angle for the *S*,*S*(1-naphthyl)ethylamine complex is smaller than that of the *S*,*S*(1-phenyl)ethylamine complex, suggesting that the larger π structure in the guest results in better π-π stacking. However, we can't explain why the observed hetero-preference of the system (*S*,*S*-host binds *R*-guest better than *S*-guest) is not consistent with the angles. The host-guest homo complex, which is energetically less favorable, has a smaller π-π angle than is computed for the hetero complex. The same trend is observed for ring distance. Likely the B3LYP/6-31G* method does not do a good job of accounting for π–π interactions.

The hydrogen bond distance between hydrogen atoms in ammonium and oxygen in the host matches the experimental results very well. The hetero complexes (such as the (*S*, *S*)-host and *(R)*-guest) have shorter hydrogen bonds than the corresponding

homo complexes. This correlates with the experimentally observed hetero-preference very well, suggesting the important role of hydrogen bonding in the enantiodiscrimination of these complexes.

Table 2-5: Computed $\Delta\Delta G°$ Values (*hetero- homo,* kJ mol^{-1}) for Chiral Crown-Ammonium Complexes

	MMFF		B3LYP/6-31G*	
Guest	Host 1	Host 2	Host 1	Host 2
phenylethylamine	-4.9	-1.7	-13.3	0.4
α(1-naphthyl)ethylamine	-10.5	-1.2	-11.8	0.1
α,4-dimethyl-benzylamine	-6.0	1.4	-13.6	0.7

Computed energetics for various complexes at the MMFF and B3LYP/6-31G* levels of theory are listed in Table 2-5, and may be compared with the experimentally measured values in Tables 2-1 and 2-2, if entropic effects are assumed to be small. The computed values for host **1** reflect the experimentally observed *hetero* enantiomeric preference at both the MMFF and B3LYP/6-31G* levels of theory. Theory at both levels also predicts greater enantiodiscrimination for host **1** than for host **2**, as observed. For host **1**, the experimentally observed increase in enantiodiscrimination upon methylation of the guest π system is also reflected in the computed results. However, the complexes involving host **2** do not appear to be as accurately described by theory, which suggests that methylation of the guest π system reverses the enantioselectivity and also suggests *homo* preference for each guest

examined at the B3LYP/6-31G* level. The quantitative agreement between theory and experiment is also poor, as might be expected when the differences between the diastereomers are as small as those measured here; this level of theory is not adequate to accurately describe such small differences.

Conclusions

The fundamental interactions between aromatic crown molecules and aromatic amines in gas phase are π-π stacking and hydrogen bonding. High affinity between host and guest doesn't necessarily result in better recognition. If the affinity is too high, both host enantiomers will bind to the chiral guest very tightly so little discrimination is observed. In order to build an efficient chiral recognition system, we need to select a host and guest that have intermediate binding affinity. Hydrogen bonding is another significant factor that controls the host-guest affinity. In the case of host 1, more hydrogen bonds results in better recognition. We also find that the degree of chiral recognition is greater in the gas phase than in solution. Modeling at the B3LYP/6-31G* level is qualitatively correct, but quantitative agreement with experiment is poor.

An important extension of this work will be the investigation of chiral recognition in a restricted space, such as within the cavity of a cucurbituril molecule (see chapter 5). The restricted space might result in closer stereo center distances, therefore enhancing chiral recognition. Similar work has been done by Kim et al. in solution.[21]

References

(1) Fang, N.; Dearden, D. V. "Equilibrium Methods for Characterizing Gas Phase Chiral Recognition," in *Chiral Recognition in the Gas Phase,* Zehnacker-Rentien, A., ed.; Taylor & Francis: London, 2010.

(2) Sawada, M. *Mass Spectrom. Rev.* **1997**, *16*, 73-90.

(3) Ramirez, J.; He, F.; Lebrilla, C. B. *J. Am. Chem. Soc.* **1998**, *120*, 7387-7388.

(4) Tao, W. A.; Zhang, D.; Wang, F.; Thomas, P. D.; Cooks, R. G. *Anal. Chem.* **1999**, *71*, 4427-4429.

(5) Tafi, A.; Botta, B.; Botta, M.; Monache, G. D.; Filippi, A.; Speranza, M. *Chem. Eur. J.* **2004**, *10*, 4126-4135.

(6) Dearden, D. V.; Dejsupa, C.; Liang, Y.; Bradshaw, J. S.; Izatt, R. M. *J. Am. Chem. Soc.* **1997**, *119*, 353-359.

(7) Dearden, D.V.; Liang, Y. *J. Phys. Chem. A* **2002,** *106,* 9665-9671.

(8) Senko, M. W.; Canterbury, J.D.; Guan, S.; Marshall, A. G. *Rapid Commun. Mass Spectrom*. **1996**, *10*, 1839-1844.

(9) Kellersberger, K. A.; Dearden, D. V. In *The Encyclopedia of Mass Spectrometry;* P. B. Armentrout, Ed.; Elsevier: San Diego, 2003; Vol. 1 (Theory and Ion Chemistry); pp. 338-345.

(10) Liang, Y.; Bradshaw, J. S.; Izatt, R. M.; Pope, R. M.; Dearden, D. V. *Int. J. Mass Spectrom.* **1999**, *185/186/187*, 977-988.

(11) Chen, L.; Marshall, A. G. *Int. J. Mass. Spectrom. Ion Processes.* **1987**, *79*, 115-125.

(12) Chen, L.; Wang, T.-C. L.; Ricca, T. L.; Marshall, A. G. *Anal. Chem.* **1987**, *59*,449-454.

(13) Samu, E.; Huszthy, P.; Somogyi, L.; Hollosi, M. *Tetrahedron: Asymmetry,* **1999**, *10(14)*, 2775-2795.

(14) Weiner, S. J.; Kollman, P. A.; Nguyen, D. T.; Case, D. A. *J. Comput. Chem.* **1986**, *7*, 230-252.

(15) Halgren, T. A. *J. Comput. Chem.* **1996**, *17*, 490-519.

(16) Halgren, T. A. *J. Comput. Chem.* **1996**, *17*, 520-552.

(17) Halgren, T. A. *J. Comput. Chem.* **1996**, *17*, 553-586.

(18) Halgren, T. A. *J. Comput. Chem.* **1996**, *17*, 587-615.

(19) Halgren, T. A. *J. Comput. Chem.* **1996**, *17*, 616-641.

(20) Izatt, R. M.; Wang, T.; Hathaway, J. K.; Zhang, X. X.; Curtis, J. C.; Bradshaw, J. S.; Zhu, C. Y. *J. Inclusion Phenom. Mol. Recogn. Chem.* **1994**, *17*, 157-175.

(21) Rekharsky, M. V.; Yamamura, H.; Inoue, C.; Kawai, M.; Osaka, I.; Arakawa, R.; Shiba, K.; Sato, A. Ko, Y. H.; Selvapalam, N.; Kim, K.; Inoue, Y. *J. Am. Chem. Soc.* **2006**, *128*, 14871-14880.

Chapter 3

Characterization of Porous Polymer Monolith Nanospray Ionization with FTICR-MS

Introduction

About Electrospray Ionization. Most of the work in our group is focused on the characterization of supramolecules. Transferring these supramolecular complexes into the mass spectrometer without breaking the weak interactions that hold them together is an essential task for such research. For more than 15 years, the most common ionization method in our lab has been electrospray ionization. Electrospray ionization (ESI) is an atmospheric pressure ionization technique that produce gas-phase ions by spraying solution-phase analyte at high voltage. This ionization method was first introduced by Dole et al. in 1968.[1] In the early 1980s, Fenn et al. further developed the application of ESI as an ionization technique for mass spectrometry (MS).[2,3] The 2002 Nobel prize in chemistry was granted to Fenn for this invention. Since then, ESI has become one of the most significant ionization methods for MS due to its capability of intactly ionizing large biomolecules, non-volatile molecules and non-covalently bonded supramolecules.[4, 5] What's more, ESI makes it easy to couple liquid-based separation techniques, such as liquid chromatography (LC)[6, 7] and capillary electrophoresis,[8-10] to MS instruments, so ESI has become a very general ionization technique. However, recent studies[11] indicate that small cations gain extensive internal energy in the ESI process. This internal energy may destroy the

weak noncovalent interactions between the molecules in supramolecular complexes. Another drawback of ESI is ion suppression, especially when the sample is a mixture or it has a high concentration of salt. In ion suppression, the easily ionized molecules tend to scavenge the available charges in the spray solution and dominate the resulting ion population even though other compounds may be present in high abundance.

Brief introduction to nanoelectrospray and its properties. When the electrospray spray rate falls into the nL/h range, it is called nanoelectrospray or nanospray, which was first demonstrated by Wilm and Mann in 1994.[11] Nanospray has ionization source construction and operating conditions similar to ESI.[11,12] By pulling common capillaries to a fine tip with i.d in the micrometer range, the flow rate can be reduced to the nanospray range, typically tens of nL/min. Conductive coatings, like gold, graphite, or a conducting polymer are deposited on the fine tip to provide electrical contact and allow application of high voltage to the spray solution.

However, nano-ESI is more than just a minimized-flow ESI.[13] Nanoelectrospray usually yields cold ionization, meaning that fragile complexes survive the ionization process, keeping the noncovalent bonds intact. Second, analyte suppression can be greatly reduced at nanospray flow rates, and nano-ESI shows a higher tolerance towards salt contamination. Further, some groups have already obtained good signal in the nanospray range without pneumatic assistance,[11] which means higher sensitivity may be achieved with nanospray.

Ionization Mechanism. To understand the special analytical properties appearing in nano-ESI,[14] it is necessary to discuss the ion formation mechanism. The ion

formation process in ESI can be divided into two consecutive processes. The first process is to disperse the analyte into charged droplets. In the second process, these initial droplets evaporate and fission into smaller and more highly charged offspring droplets. The second process repeats on and on to form the observable ions. Because the droplet fission steps themselves likely do not differ in conventional ESI and nano-ESI, the origin of the differences in mass spectral behavior must exist in the first process, the dispersion of the liquid into the charged droplets. In the most widely accepted model,[15] ion release happens after a series of unsymmetrical droplet fissions until the droplet reaches a critical size. It is usually assumed that within each fission step the initial droplet loses 15% of its charge and 2% of its mass, and the offspring droplet diameter is 1/10 of the initial diameter.

Therefore, the size of the initial droplet has a significant influence on ion formation. First, the time scale of ion formation can be affected by the initial droplet size. Larger droplets require additional fission steps to be small enough for ion release, so the formation of the observable ions occurs later than for the small droplets. Second, the initial droplets need to evaporate to reach a sufficient charge density for fission to occur, leading to a concentration increase of both the analyte and any contaminants. The larger the initial droplets are, the higher the concentration in the final droplets. Higher salt concentration favors formation of salt clusters, which depress the analyte signal. Hence, the offspring droplets formed early in the ESI process (before much evaporation can occur) and those arising from small precursor droplets contain low salt concentration and generate less salt clusters. Third, the

fission residue finally becomes a "wet salt crystal" with the ongoing loss of charge and increase in salt concentration. For large initial droplets, the total ion yield is greatly influenced. Therefore, nanospray, producing small droplets initially, has higher ionization efficiency. From the considerations above, we conclude that conventional ESI and nano-ESI undergo different numbers of fission steps before forming the mass spectral ions.

Another analytical property of nano-ESI is less suppression of hydrophilic analytes. The desolvation energy for hydrophilic molecules is higher than that for hydrophobic molecules. Therefore, hydrophilic molecules require more fission steps (resulting in smaller droplets) before they can be released from the droplets. For small precursor droplets, hydrophilic molecules can directly release from the droplets without waiting for droplet fissions, and ion formation efficiency for hydrophilic molecules is strongly enhanced.

Several models have been used to estimate the size of the initial droplets according to the flow rate.[16] Experimental results also show a relationship between flow rate and initial droplet size. Among these models, the Wilm model[11] fits the experimental results best. The droplet diameter at the typical nano-ESI flow rate of 20 nL/min is about 80 nm according to the Wilm model, about 1/10 of the size in conventional ESI. The representative solvent in the Wilm study was a methanol/water mixture containing a few percent of acetic acid, typical of what is used in ESI.

The development and application of nano-ESI. The advantages of nano-ESI in comparision to conventional ESI have driven more and more people toward applying

nano-ESI and studying how to build improved nano-ESI. Wilm and Mann mentioned one additional advantage: they can use long-time signal averaging without any changes of ionization conditions to obtain accurate mass measurements in protein mixture analysis because of the small sample consumption in nano-ESI.[16] They also claim that they can spray salt-containing aqueous solutions with nanospray. Such a high tolerance for salt has been the exclusive property of MALDI.

Wood et al. used a conductive polymer coating on a pulled capillary instead of the more common metallized coating, which is highly susceptible to deterioration by electrical discharge.[17] This long-term durable emitter is relatively easy to produce, and the transparent polymer film allows the user to visualize the analyte solution in the emitter. The sensitivity of this polymer-coated emitter is similar to that of a gold-coated emitter.

Smith et al. generated multiple electrosprays by using microfabricated polycarbonate arrays.[18] Each emitter has a 150 μm o.d. and 30 μm i.d. There is a gap between the outer edge of each emitter and the array substrate, so no wetting of the capillary occurs at the end of the emitter. Separate Taylor cones are generated at the end of each emitter. Stable spray current was obtained from 2 to 9 emitters in the arrays. At a constant total flow rate, the total ion current is proportional to the square root of the number of emitters, n (Equation 3-1).

$$I_{total} = nI^{*} = n[f(\varepsilon)(Q^{*}K\gamma/\varepsilon)^{1/2}] = n^{1/2}[f(\varepsilon)(nQ^{*}K\gamma/\varepsilon)^{1/2}] = n^{1/2}[f(\varepsilon)(QK\gamma/\varepsilon)^{1/2}] = n^{1/2}I_{single} \quad (3\text{-}1)$$

In Equation 3-1, I^* and Q^* are the ion current and the liquid flow rate carried by each emitter in the array respectively, K is the electric conductivity of the liquid, γ is the surface tension of the liquid, ε is the dielectric constant of the liquid, I_{total} is the total ion current from the multielectrosprays, and I_{single} is the ion current from a single electrospray at the same flow rate. This ionization source device applies a syringe pump to supply the analyte, which results in an ionization duration of several hours without reloading analyte, whereas the analyte in a typical nano-ESI needle usually only lasts for 20-30 minutes.

Oleschuk et al. produced a robust nanospray emitter by utilizing a porous polymer monolith (PPM) at the end of a fused-silica capillary.[19, 20] This nanospray emitter is more robust than conventional pulled silica emitters. It can be used at a wide range of flow rates with only a modest increase in back-pressure, so this nanospray is a suitable interface to couple microfluidic devices to mass spectrometers. The reproducibility from tip to tip was reported to be 17% RSD. The sensitivity of the PPM emitter is better than that of the conventional nanospray emitter when the flow rate is between 100 nL/min to 1000 nL/min，whereas conventional nanospray shows better sensitivity at flow rates below 100 nL/min. It is difficult to get a good spray at low flow rate with a large-diameter PPM-filled capillary. Decreasing the i.d. of the capillary might help to increase the sensitivity; however, it hurts the absolute signal and also causes wetting problems at the end of the emitter.

Although nanospray has its advantages, conventional nanospray suffers from several limitations. For pulled nanospray capillaries with conductive coatings,[21, 22] the

lifetime of the coated tip is generally short because of both breakage and clogging. Furthermore, the coatings are often thin and uneven, and could not guarantee stable electrospray for more than several hours. Third, the fabrication of the coating is time-consuming and requires special instrumentation. Finally, it is impossible to control the flow rate of nanospray during the spray process because the sample is not provided by a syringe pump. The spray can only be turned on and off with the high voltage.

The goal of this work. We are interested in using multiple electrosprays to enhance the signal, and building porous polymer monolith (PPM) nanospray with common size capillaries seems to be very promising.[19] In this case, we can use a syringe pump to provide sample, so we can have more control of the spray than in conventional nanospray. In collaboration with Professor Lee's group at Brigham Young University, we produced robust nanospray emitters (shown in figure 3.1) by utilizing a porous polymer monolith (PPM) at the end of a fused-silica capillary.[19] Dr. Oleschuk invented the PPM emitter interface to replace the conventional pulled silica emitters, which suffer from limitations including poor robustness, clogging, and low flow rates. Some new properties that we would like to test with the PPM emitter are ion suppression and the "coldness" of PPM nanospray. We will also improve the fabrication steps to make the PPM emitter behave in a fine mist mode, rather than in Taylor cone mode. In addition, we will apply PPM emitters to the study of supramolecular complexes for the first time.

The porous polymer monolith, which is about 1-2 mm in length, is

photopatterned so that it is present only close to the spray end of the capillary. A platinum wire is threaded through the capillary, with one end touching the monolith. The wire provides high voltage, even in the presence of gas bubbles in the capillary. The manufacturing process for a PPM-filled capillary is quite reproducible and easy. In this chapter we will show that this PPM nanospray emitter possesses some special analytical properties: decreased ion suppression, quite stable spray, strong signal intensity and good reproducibility in emitter performance.

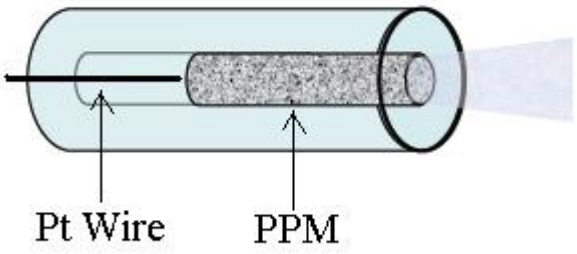

Figure 3.1: Schematic of the PPM emitter. Not drawn to scale.

Experimental Section

Fabrication of the PPM emitter. In a pre-treatment step,[23] the capillary was first washed with ethanol and deionized water, then rinsed with 0.3 M NaOH for 0.5 hour. Next, the capillary was immersed in 2 M hydrochloric acid for 3 hours at the boiling point. Afterward, it was rinsed with water and ethanol and dried at 110 ℃ overnight in a vacuum desiccator. The capillary was then immersed in a 15% solution of 3-(trimethoxysilyl) propyl methacrylate in dried toluene overnight at 35 ℃. After silanization, the capillary was rinsed with toluene and acetone and dried overnight in a vacuum desiccator. In the fabrication step,[24] the monomer mixture was prepared with solutions added in the following sequence: 0.008 g photo-initiator (2,

2-dimethoxy-2-phenyl-acetophenone), 0.48 g monomer (butyl methacrylate), 0.32 g crosslinker (ethylene glycol and dimethacrylate) and porogens (1.02 g methanol & 0.18 g 1-propanol). The monomer mixture was ultrasonicated for 5 minutes. Then the monomer mixture solution was introduced to the capillary via surface tension. The capillary was then placed under a Dymax 5000AS UV curing lamp (Torrington, CT) for 10 minutes. The irradiation intensity of the UV curing lamp is 200 mW/cm^2 in the wavelength range of 320-390 nm.

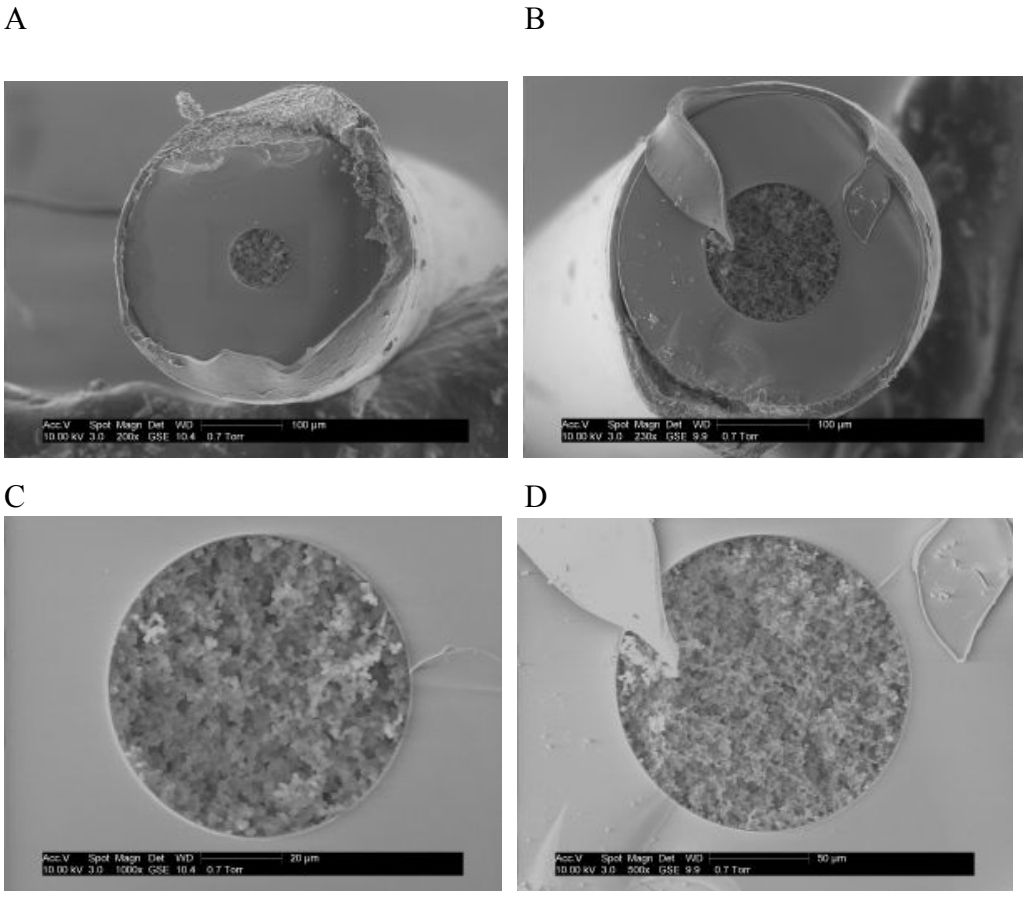

Figure 3.2: SEM micrographs of the structure of the monoliths in 75 µm i.d. capillary (A) and 150 µm i.d. capillary (B). Pictures (C) and (D) are zoomed views of (A) and (B) respectively.

We have photopatterned monoliths in both 75 µm i.d., 360 µm o.d. and 150 µm i.d., 360 µm o.d. capillaries. The morphology of the prepared monolith was investigated using a scanning electron microscope (SEM). Figure 3.2 shows SEM micrographs of the structure of the monolith in the cross section of the capillary. The SEM images show the monoliths formed in both capillaries are homogenous. The pore size is about 1-2 µm.

Instrument. A commercial Fourier transform ion cyclotron resonance mass spectrometer (model APEX 47e, Bruker Daltonics, Billerica, MA) was used in all experiments. MIDAS is the software that controls the sequence of each experiment.[25, 26] The nanoelectrospray source was mounted on an x-y-z translation stage. A zero-dead volume union was used to couple the solution transfer line and the PPM-filled capillary. A 50 µL syringe (Hamilton) filled with analyte was pushed by a syringe pump (Harvard Apparatus, Harvard, MA).

Results and Discussion

The goal in producing a PPM emitter is to have a large number of individual nanoelectrospray emitters. Wetting of the capillary face can be an issue with these emitters because if the flow of the individual pores recombines the result is one large Taylor cone rather than many nanospray emission sources. Such a Taylor cone is easily visible when the emitter is viewed with a microscope. What we hope to see instead is a fine mist spraying from the end of the monolith.

For the capillary with 75 μm i.d., the hydrophobic monolith is a relatively small portion of the cross section of the emitter face. The silica portion of the face is hydrophilic and subject to wetting. Therefore, the 75 μm capillary is more likely to have wetting problems than the 150 μm i.d. capillary. What we observed in the spraying process with the 75 μm i.d. capillary is that a visible Taylor cone is often formed at the emitter end, which means the various flow channels are combining such that ionization occurs under conventional ESI conditions. This wetting problem is less severe when we use the 150 μm i.d. capillary as the spray emitter. Thus most of the following results were obtained with 150 μm i.d. capillaries.

In the pre-treatment step for the 150 μm i.d. capillary, we have tried to skip the step of rinsing the capillary with NaOH to avoid excessive etching of the capillary wall, which might thin the capillary wall and cause it to be vulnerable to breakage. However, the attachment between the monolith and the capillary wall becomes weak in this case.

We have also tried to photopattern the monolith with larger or smaller pore sizes by changing the ratio of the two porogens. We found that larger pore size emitters don't have nanospray properties and smaller pore sizes cause extremely high back pressure, so the choice of 1-2 μm pore sizes is a compromise between these factors.

The durability of the current PPM emitter is satisfactory. The following SEM image shows the cross section at the emitter end after 100 hours of spray. The capillary is still filled homogenously with monolith (shown in figure 3.3).

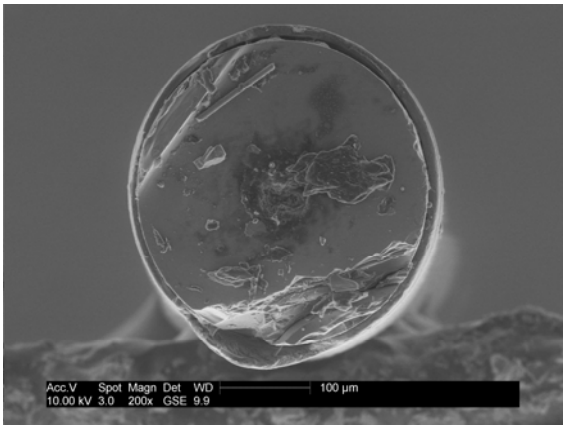

Figure 3.3: SEM images of the structure of the used monolith in 75 µm i.d. capillary

For the following tests, we use 18-crown-6 and metal ions (Li^+, Na^+, K^+, Rb^+) as the testing system because cations bind well with 18-crown-6 and all the complexes are easily ionized in electrospray. In addition, we are quite familiar with the properties of the various complexes, which facilitates characterization of the PPM emitter.

Stability Test on PPM Emitter. I electrosprayed a mixture of 18-crown-6 and metal ions (Li^+, Na^+, K^+, Rb^+) with a PPM nanospray emitter and a common microspray emitter (50 µm i.d., 360 µm o.d. capillary) respectively to compare the stability of the two electrospray modes by measuring the absolute signal strength of each metal complex. The experiments were done in a series of alternating 100-scan runs comparing the PPM emitter to the fused silica microspray emitter. The concentration of the 18-crown-6, Li^+ and Rb^+ were 133 µM, 59.2 µM, and 7.4 µM respectively, in pure methanol. Na^+ and K^+ are contaminants (less than 0.04%) in the LiCl salts and 18-crown-6. The experimental event setting in MIDAS and the tuning parameters for the ionization source are exactly the same for PPM nanospray mode

and common microspray mode. Therefore, the differences in the spectra are only due to differences in the emitters. In the PPM nanospray mode, the sample flow rate was 333 nL/min, and the voltage applied to the sample was 2.1 kV. The emitter was always placed 1.5 mm away from the drying tube and 0.5 mm to the right of the drying tube axis. In the common microspray mode, the sample flow rate was also 333 nL/min, and the voltage applied to the sample was 1.8 kV. The emitter was always placed 1.5 mm away from the drying tube and 0.2 mm to the left of the drying tube axis. With the emitter in this location, a stable Taylor cone was formed. Figure 3.4 shows the absolute signal strength of each metal complex in consecutive sets of 100 scans. Graphs A, C, and E were done with the PPM nanospray emitter and graphs B, D, and F were done with the common microspray emitter.

A

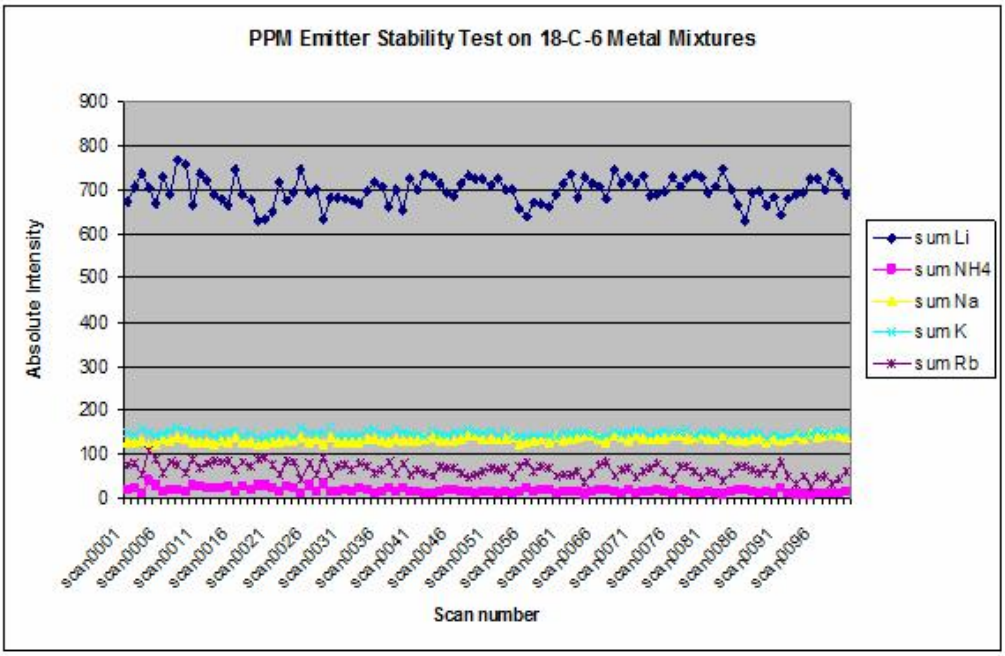

B

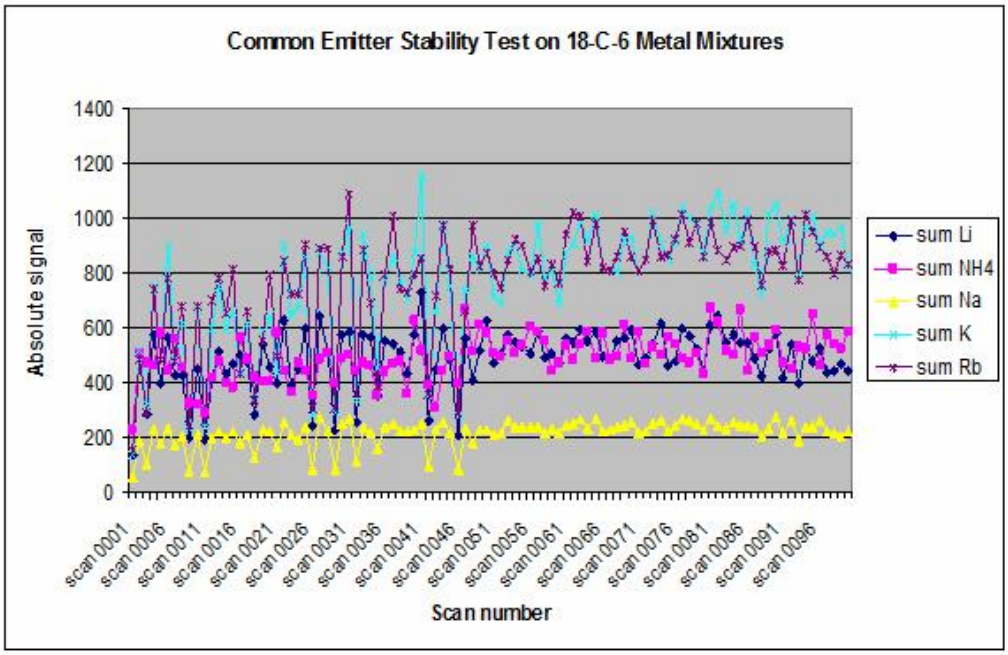

C

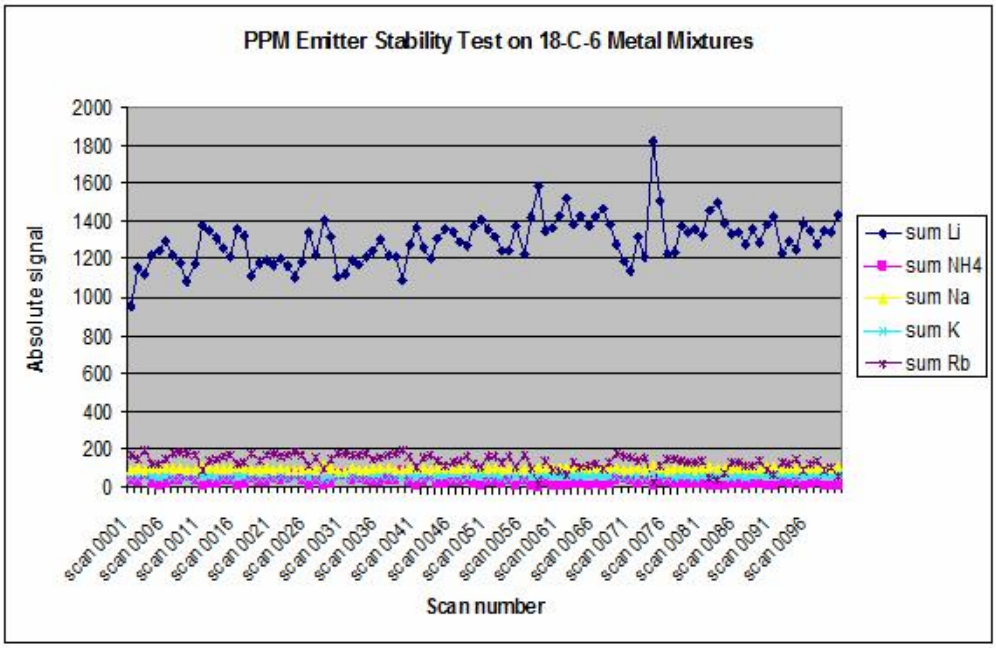

D

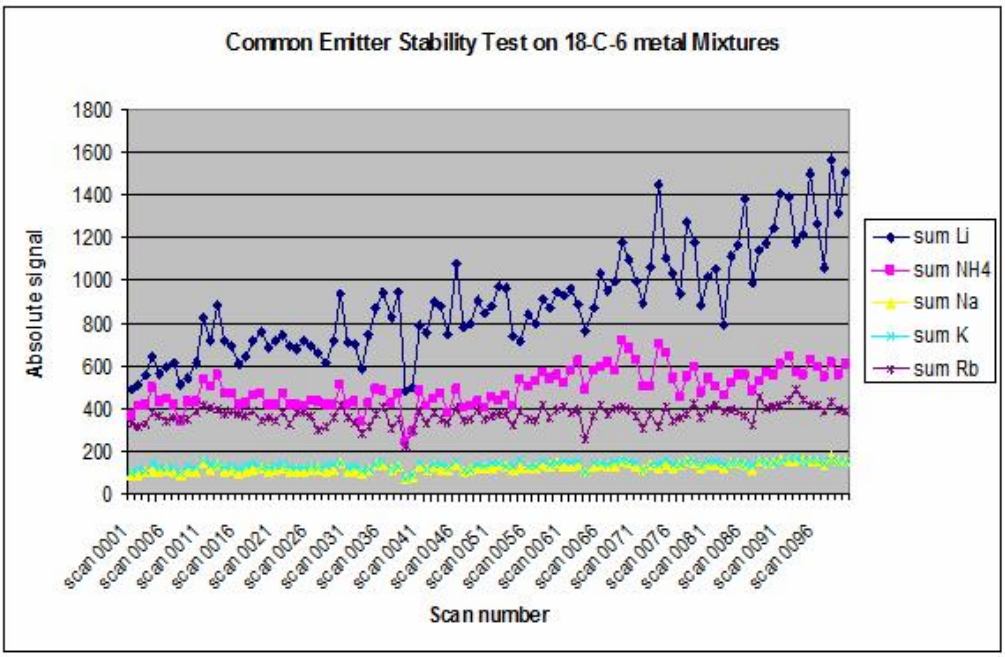

E

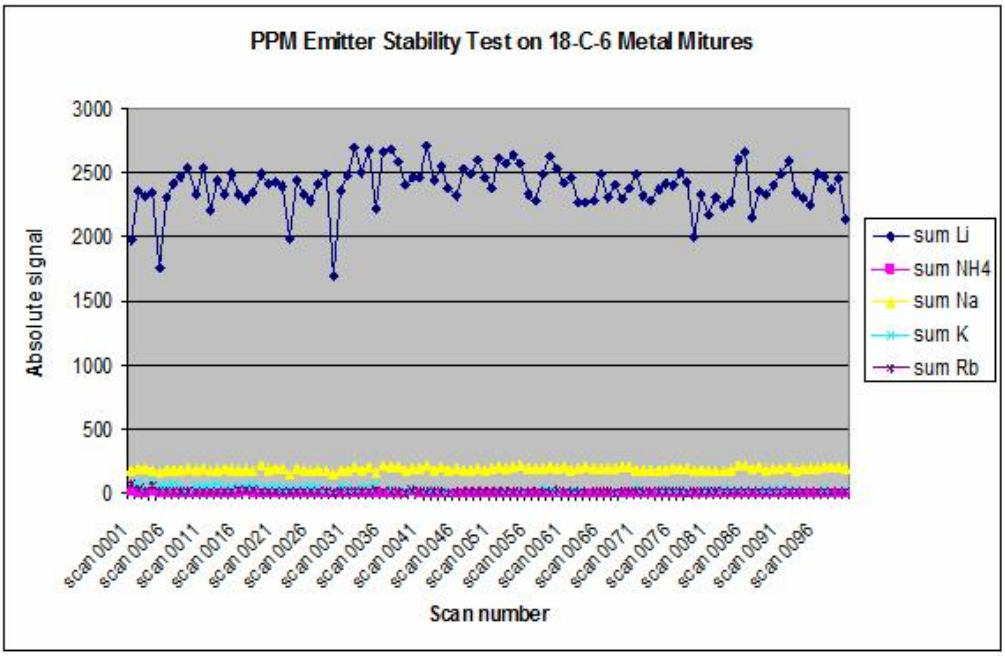

F

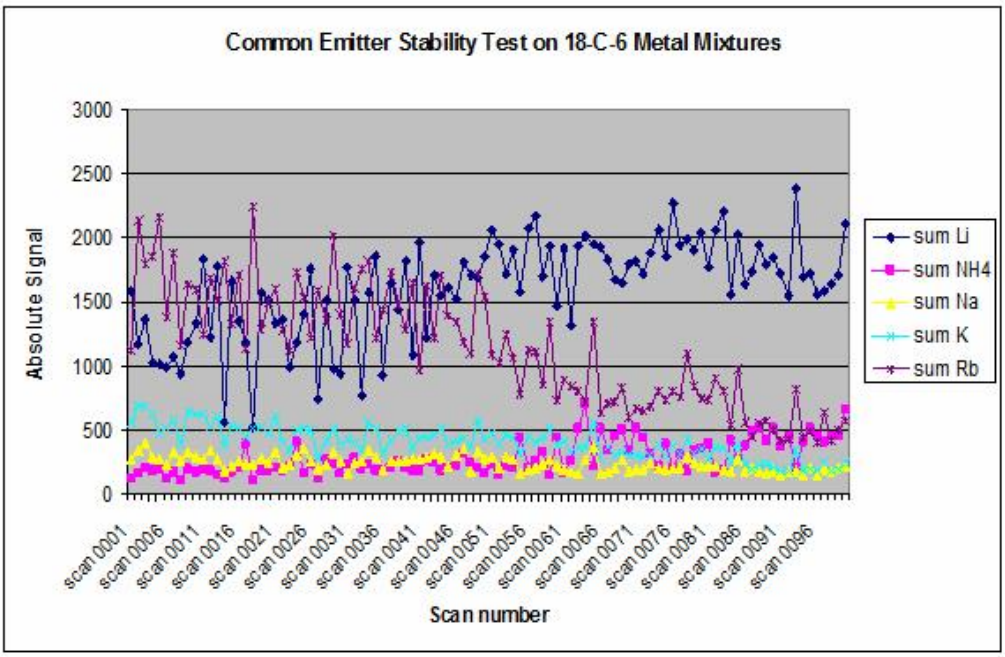

Figure 3.4: The absolute signal strength of each metal complex in consecutive 100 scans. (A), (C), (E) were done with the PPM nanospray emitter, and (B), (D), (F) were done with the common microspray emitter.

Signal from the 18-crown-6•Li^+ complex is quite strong in both modes, so we calculated the relative standard deviation of its absolute signal strength to compare the stabilities in each mode. The relative standard deviations of tests A, C and E are 4.3%, 9.4 and 7.3%, respectively. The relative standard deviations of tests B, D, and F are 22.5%, 28.2% and 23.9%. From these data, the PPM nanospray emitter showed much better stability for the 18-crown-6•Li^+ complex than the common microspray emitter. The graphs from A to F also showed the stabilities for all the other metal complexes are also better for the PPM emitter.

Absolute Signal Strength. In addition to stability, the absolute signal strength is another important property of an ionization method. The mean absolute 18-crown-6•Li^+ complex signal strength in tests A, C, and E was 699.2, 1295.9 and 2392.3, respectively. In contrast, the mean absolute 18-crown-6•Li^+ complex signal strength in tests B, D, and F was 487.3, 894.3 and 1603.1, respectively. Therefore, the average signal for the 18-crown-6•Li^+complex was about 30% stronger for the PPM emitter than for the common microspray emitter. We attribute the stronger signal to the fact that even though the total flow rates were the same, the PPM emitter has many emission sources, whereas conventional microspray just has one source.

Ion Suppression Test. One of ESI's drawbacks is ion suppression, especially when the sample is a mixture or it has a high concentration of salt. The ion suppression properties of PPM emitters have not been previously characterized, and

this problem is what we would like to overcome in the ionization step. The easily ionized molecules tend to scavenge the available charges in the spray solution and dominate the resulting ion population even though other compounds may be present in high abundance. In nanospray, the spray droplets become so small that the likelihood of multiple analytes being present in the same droplet is low. When analyte molecules are in separate droplets, they do not compete for the available charge on the droplet, and ion suppression is therefore decreased.[13, 14]

A

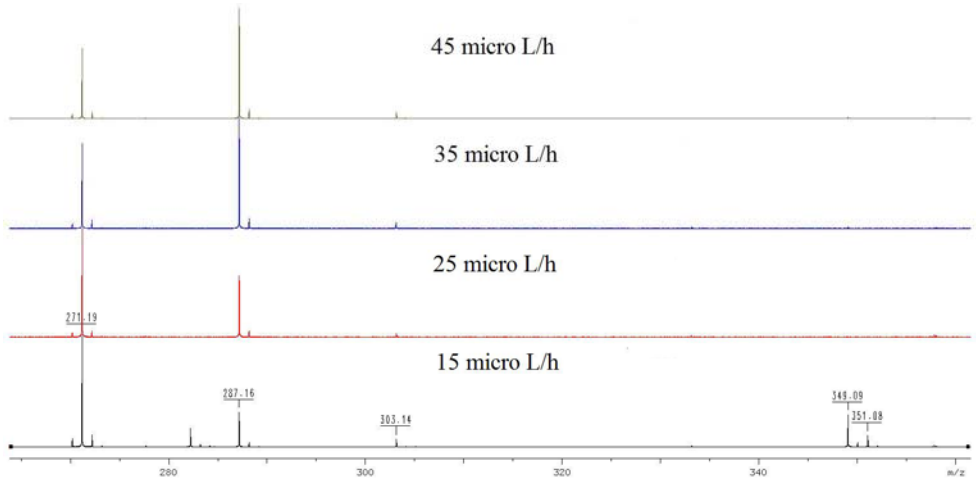

B

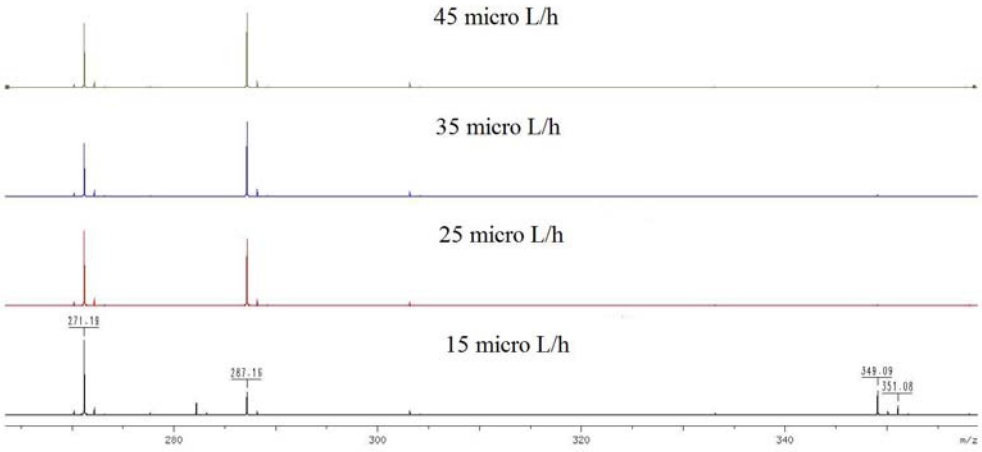

C

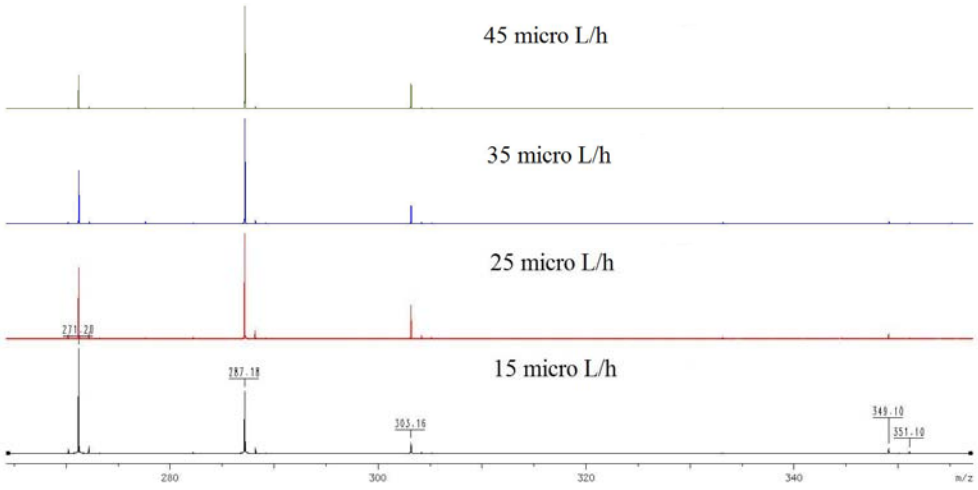

D

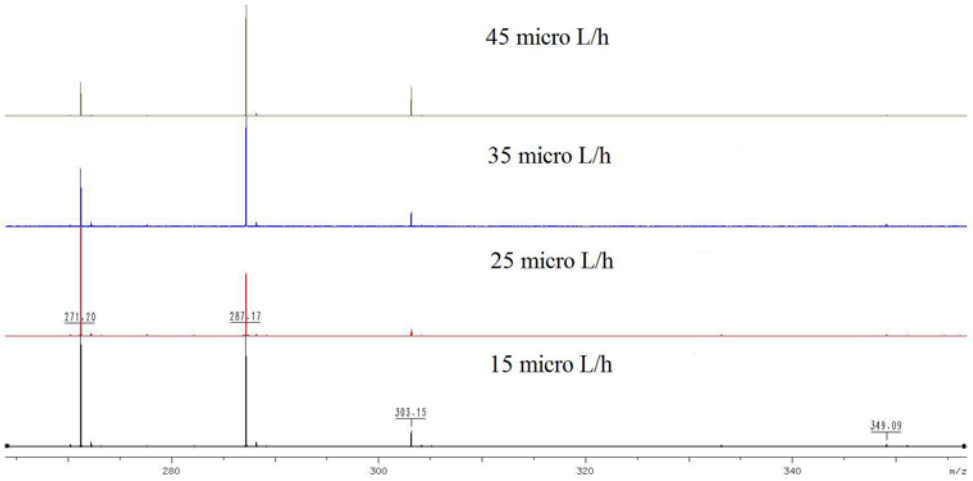

E

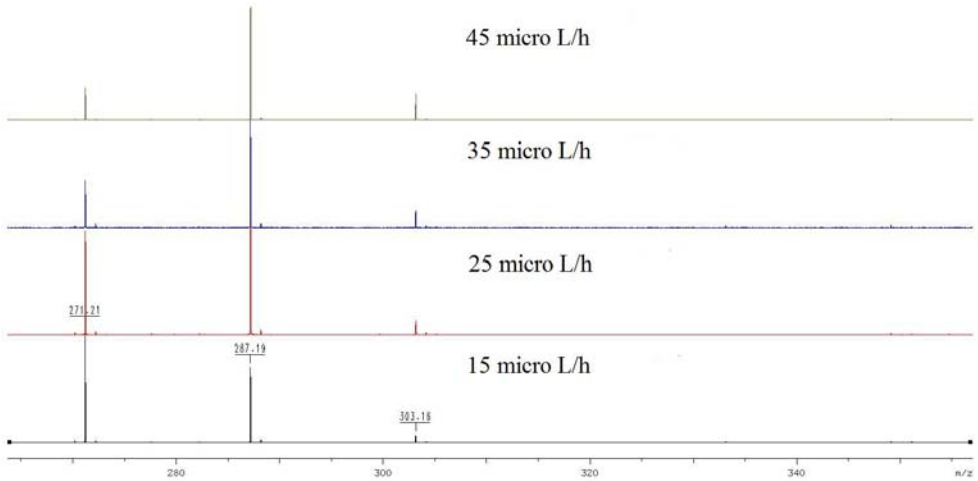

F

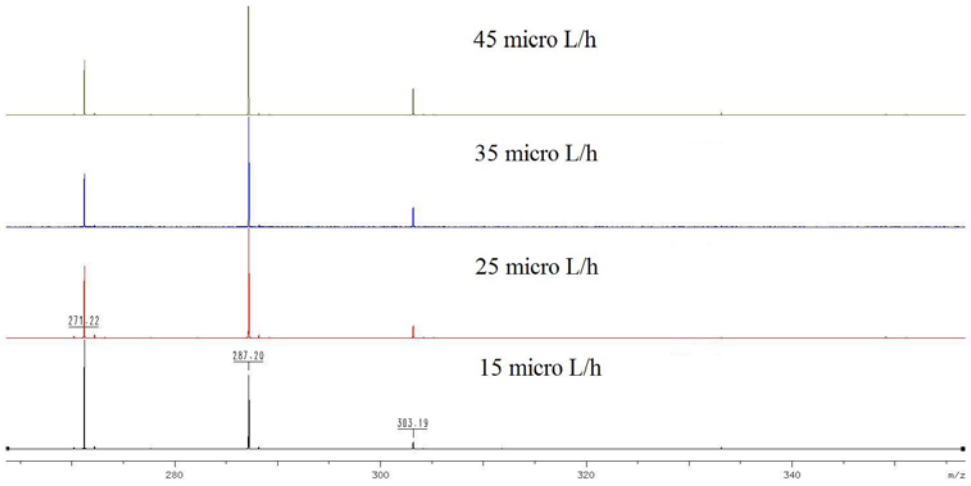

Figure 3.5: Mass spectrum of 18-crown-6 and metal ions (Li^+, Na^+, K^+, Rb^+) mixtures with PPM emitter at variable flow rate.

We have examined ion suppression by spraying mixtures with known solution concentrations and observing the relative peak intensities in the resulting spectra. In the mixtures we used, the concentrations of Na^+ and K^+ are low as they are contaminants. However, they tend to compete and suppress the Li^+ and Rb^+ due to their high binding affinity with 18-crown-6. Rb^+ has a higher binding affinity with 18-crown-6 in solution than Li^+, and it has lower desolvation energy than Li^+. According to calorimetric results in water,[27] the order for complex stability is 18-crown-6•K^+ > 18-crown-6•Rb^+ > 18-crown-6•Na^+ > 18-crown-6•Li^+. The data in figure 3.4 show that the 18-crown-6•Li^+:18-crown-6•Rb^+ ratio is about 1.5 with the microspray emitter. However, 18-crown-6•Li^+:18-crown-6•Rb^+ ratio is about 10 with the PPM emitter, which is in good agreement with the concentrations in solution. Therefore, the PPM emitter achieves the expected nanospray benefit of decreased ion

suppression, without incurring the weak, unstable signal problems that often plague conventional nanospray emitters.

We did variable flow rate tests on the PPM emitter to further investigate the influence of droplet size on the relative complex signal strengths. We electrosprayed a mixture of 18-crown-6 and metal ions (Li^+, Na^+, K^+, Rb^+) with the PPM emitter and the sample injection flow rate was varied through values of 15 µL/h, 25 µL/h, 35 µL/h, and 45 µL/h. The concentration of the 18-crown-6, Li^+ and Rb^+ are 70.0 µM, 28.0 µM, and 1.8 µM, respectively in pure methanol. From set A to set F, the experimental event setting in MIDAS and the tuning parameters for the ionization source were the same. The voltage applied to the sample was 1.8 kV. The emitter was always placed 1.5 mm away from the drying tube and 0.2 mm to the left of the drying tube axis. Suppression tests A and B (shown in figure 3.5) were done with one PPM emitter and tests C, D, E and F were done with a different PPM emitter. They all show similar results.

We observed that the 18-crown-6•Na^+ complex suppressed the 18-crown-6•Li^+ complex more and more with increasing flow rate, which is proportional to droplet size[11] (shown in figure 3.5). From set A to set F, 18-crown-6•Li^+ is the most abundant peak at 15 µL/h. The 18-crown-6•Na^+ became the strongest peak at 25 µL/h or 35 µL/h. We expected to see growth of the 18-crown-6•Rb^+ peak with increasing flow rate; however, we only see 18-crown-6•Rb^+ at 15 µL/h. It is likely that 18-crown-6•Na^+ not only suppresses 18-crown-6•Li^+ but also suppresses 18-crown-6•Rb^+. Perhaps this is not surprising because the Rb^+ ion concentration is

actually very low in the sample. When we attempted to increase the Rb^+ concentration, suppression of the 18-crown-6•Li^+ signal was severe.

Conclusions

We have investigated the application of porous polymer monolith (PPM) emitters as a nanospray method which has the advantages of conventional nanospray without incurring such disadvantages as poor signal stability, poor capillary robustness and low absolute signal strength. In comparison to conventional tapered fused silica microelectrospray emitters, the PPM emitters produce generally stronger absolute signal with much greater stability. Ion suppression is decreased with the PPM emitter to the extent that the complex ratio is in good agreement with the concentrations in solution. Finally, we generally gained good reproducibility in emitter performance.

References

(1) Dole, M.; Mach, L. L.; Hines, R. L.; Mobley, R. C.; Ferguson, L. P.; Alice, M. B. *J. Chem. Phys*. **1968**, *49*, 2240-2249.

(2) Yamashita, M.; Fenn, J. B. *J. Phys. Chem.* **1984**, *88*, 4451-4459

(3) Yamashita, M.; Fenn, J. B. *J. Chem. Phys*. **1984**, *88*, 4671-4675.

(4) Fenn, J. B.; Mann, M.; Meng, C. K.; Wong, S. F.; Whitehouse, C. M. *Science* **1989**, *246*, 64-71.

(5) Tang, X.; Bruce, J. E.; Hill, H. H.; *Anal. Chem.*, **2006**, 78 (22), 7751-7760.

(6) Whitehouse, C. M.; Dreyer, R. N.; Yamashita, M.; Fenn, J. B. *Anal. Chem.* **1985**,

57, 675-679.

(7) Bruins, A. P.; Covey, T. R.; Henion, J. D. *Anal. Chem.* **1987**, *59*, 2642-2646.

(8) Smith, R. D.; Loo, J. A.; Edmonds, C. G.; Barinaga, C. J.; Udseth, H. R. *J. Chromatogr.* **1990**, *516*, 157-165.

(9) Hofstadler, S. A.; Swanek, F. D.; Gale, D. C.; Ewing, A. G.; Smith, R. D. *Anal. Chem.* **1995**, *67*, 1477-1480.

(10) Lee, E. D.; Mueck, W.; Henion, J. D.; Covey, T. R. *Biomed. Environ. Mass Spectrom.* **1989**, *18*, 844-850.

(11) Wilm, M.; Mann, M. *Anal. Chem.* **1996**, *68*, 1-8.

(12) Anderegg, R. J.; *Anal. Chem.* **1997**, *69*, 3188-3192.

(13) Juraschek, R.; Dulcks, T.; Karas, M. *J. Am. Soc. Mass Spectrom.* **1999**, *10*, 300-308.

(14) Cech, N. B.; Enke, C. G. M*ass Spectrum. Rev.* **2001,** *20,* 362-387

(15) Kebarle, P.; Tang, L. Anal. Chem. 1993, 65, 972A-986A.

(16) Schmidt, A.; Karas, M.; Dülcks, T. *J. Am. Soc. Mass Spectrom.* **2003**, *14*, 492-500.

(17) Maziarz, E. P.; Lorenz, S. A.; White, T. P.; Wood, T. D. *J. Am. Soc. Mass Spectrom.* **2000**, *11*, 659-663.

(18) Tang, K.; Lin, Y.; Matson, D. W.; Kim, T.; Smith, R. D. *Anal Chem*. **2001**, *73*, 1658-1663.

(19) Koerner, T.; Turck, K.; Brown, L.; Oleschuk, R. D. *Anal. Chem*. **2004**, *76*, 6456-6460.

(20) Lee, S.; Oleschuk, R. D. *Rapid Commun. Mass Spectrom.* **2005**, *19*, 2671-2680.

(21) Bergquist, J.; Wetterhall, M. *Anal. Chem.* **2002**, *74*, 239-245.

(22) Skog, K.; Viberg, P. *Anal. Chem.* **2004**, *76*, 4241-4244.

(23) Strancar, A.; *J. Chromatogr. A.* **2005**, *1065*, 51-58.

(24) Mojca M.*; J. Sep. Sci.* **2003**, *26*,322-330.

(25) Kellersberger, K. A.; Dearden, D. V. In *The Encyclopedia of Mass Spectrometry;* P. B. Armentrout, Ed.; Elsevier: San Diego, 2003; Vol. 1 (Theory and Ion Chemistry); pp. 338-345.

(26) Liang, Y.; Bradshaw, J. S.; Izatt, R. M.; Pope, R. M.; Dearden, D. V. *Int. J. Mass Spectrom.* **1999**, *185/186/187*, 977-988.

(27) Ozutsumi, K.; Ohtsu, K.; Kawashima, T. *J. Chem. Soc., Faraday Trans.*, **1994**, *90*, 127-131.

Chapter 4

Applying the CRAFTI Method to Negative Ions

Introduction

CRAFTI is a recently-developed method to measure collision cross sections with FTICR-MS.[1] CRAFTI stands for cross-sectional areas by Fourier transform ICR. The CRAFTI technique provides information to probe the gas phase conformations of supramolecular complexes, and more importantly it allows determination of the shape, size and mass of a molecule at the same time, with ultrahigh mass resolution. Our group has considerable evidence that CRAFTI is an appropriate method for positive ions. Therefore, we are eager to know whether this new technique is valid for negative ions as well. In this chapter, I will introduce other approaches for measuring collision cross sections, the procedure we use for CRAFTI with positive ions, and the application of CRAFTI to negative ions.

Our group has been interested in investigating host-guest interactions in the gas phase for more than 15 years. With the FTICR-MS instrument, we are able to measure both the host-guest complexes' mass-to-charge ratio and their binding structures through tandem MS techniques. However, conventional FTICR does not determine the size of host-guest complexes. Collision cross sections for ions colliding with neutral gases reflect ion sizes, which provide useful information about the conformations of those ions. There are several approaches to measure collision cross sections for ions.

Measuring ion mobility is one way to obtain collision cross sections, σ. Ion mobility spectrometry (IMS) is a technique capable of separating and identifying ions based on their mobility (a property that depends on ion mass, size, and shape) in the gas phase. The heart of the IMS instrument is a drift tube, which provides a region of constant electric field and neutral background molecules through which ions migrate.[2] From the ion drift time, the ion mobility is measured, which can be used to derive the collision cross section. Equation 4-1 shows how collision cross section is calculated.[3,4]

$$\sigma_{avg} = \frac{(18\pi)^{1/2}}{16} \frac{ze}{(k_b T)^{1/2}} \left(\frac{1}{m_I} + \frac{1}{m_B} \right)^{1/2} \frac{t_d E}{L} \frac{760}{P} \frac{T}{273.2} \frac{1}{N_0} \qquad (4\text{-}1)$$

In the above equation, m_I is the mass of the ion, m_B is the mass of collision gas, z is the charge of the ion, k_b is the Boltzmann constant, t_d is the drift time, E is the electric field strength, T is the temperature, N_0 is the number density of collision gas, P is the pressure of collision gas, and L is the drift tube length. It is evident that the pressure and temperature in the drift tube have a significant influence on the value of collision cross sections,[5] so the instrument has to be calibrated before each use to guarantee an accurate measurement. Classical IMS usually suffer from low resolution and sensitivity mainly due to the lack of high-gain detectors and space charge limitation,[6] which impede the accurate measurement of cross sections. Furthermore, IMS requires a dedicated and specially-designed instrument setup. Finally, ions have to sustain multiple collisions before they get to the detector, so the structural features that we are trying to measure might be distorted in the migrating process.

Covey and Douglas proposed an energy loss method using a triple quadrupole mass spectrometer to determine collision cross sections, especially for protein ions in the gas phase.[7] They believed that the axial kinetic energy of an ion would decrease when it passes through a cell and collides with neutral gas. The hard sphere model was used here to build the relationship between the energy loss and the number of collisions. They reported the cross sections of motilin, ubiqitin, cytochrome c, myoglobin, and bovine serum albumin using this method. However, Douglas' group thought the hard sphere model for elicitation of energy loss by ion-neutral collisions was oversimplified.[8] Therefore, a drag coefficient, C_D, was introduced as a new parameter to interpret collisions taking place in the triple quadrupole mass spectrometer. This coefficient was essentially based on diffuse scattering. It related the force on an ion moving through a neutral gas with the cross sectional area, and varied with the density, viscosity, mean free path, and thermal speed of the collision gas, and with the size and speed of the ions. Equation 4-2 shows the relationship between the energy loss and the collision cross sections.

$$E/E_0 = \exp(-C_D \sigma n m_2 l/m_1) \qquad (4\text{-}2)$$

Herein, E_0 is the initial kinetic energy of the ion, E is the final energy, n is the collision gas density, σ is the collision cross section, and l is the cell length. The collision cross sections of myoglobin and cytochrome c ions in collisions with Ne, Ar, and Kr were measured using this new method. The difference between the values from this new model and those from the ion mobility experiments is just 5% on average. The comparison indicates that the diffuse scattering model is appropriate for

measuring collision cross sections.

The Rudich group designed a simple low-vacuum mass spectrometer (LVMS) operating in the milliTorr pressure regime to measure both mass and collision cross section simultannously.[6] This spectrometer is a linear time-of-flight instrument. Mass information is obtained from the TOF spectra, and collision cross section values are deduced from measurement of the ion beam attenuation as a function of the bath gas pressure in the field free drift region. They employed a microsphere plate (MSP) as the ion detector in order to get high ion sensitivity and high drift time resolution.

Investigating collisional line broadening in drift ICR is another approach to measurement of collision cross sections. The early work dates from the 1960s and 1970s by Beauchamp et al.[9] They proposed that collisional broadening in drift ICR was caused by ion-molecular interactions. Based on this assumption, they studied the effects of electric field strength, neutral gas pressure and temperature in the trapping cell on the line shapes. Their experimental results showed that the Lorentzian linewidth has a linear relationship with the pressure of the neutral gas. The ion mobilities of ions that were determined from the linewidth measurement had good agreement with results from drift ion mobility spectrometry. However, the collisions in drift ICR are low-energy-collisions, so ions have to undergo multiple collisions to undergo linewidth broadening. The number of collisions has to be carefully measured to make sure the collision cross sections can be accurately determined. Due to the lower magnitude fields and relatively low mass resolution in drift ICR, this method never gained wide acceptance.

The review above encouraged us to consider the possibility of carrying out collision cross sections measurement using FTICR-MS. It is well known that accurate mass-to-charge ratio measurements can be obtained by measuring the ion cyclotron frequency. In order to determine the ion cyclotron frequency, a radio frequency (RF) pulse is added on the transmitter plates to excite trapped ions. Ions whose cyclotron frequency is the same as that of the applied RF absorb the RF energy and are excited coherently to a larger orbit. Then a detectable image current signal is produced, digitized and recorded. If these ions collide with background gas, the ion packet dephases, causing signal decay in the time domain. The width of the observed signal peak in the frequency domain depends inversely on the length of time the ions remain coherent.[10] Therefore, FT-ICR experiments are usually done at lower pressures (10^{-9} Torr) to obtain high resolution. Marshall et al. investigated the effects of ion-neutral collisions on ion motion in the FT-ICR trapping cell.[11] They employed both Langevin and hard sphere models to study the ion trajectories. In the Langevin model, the ion is treated as a point charge, and the neutral gas is treated as an electric dipole induced by the ion. The collision cross section is inversely proportional to ion speed. The Langevin model gives rise to an exponentially decaying time-domain signal and a Lorentzian-shaped frequency domain spectrum. The Langevin model is suitable for low-energy collisions between low-mass ions and the neutral gas. The hard sphere model is appropriate for ions of high velocity (more than 1 eV translational energy), and the ion collision frequency is linearly proportional to ion velocity in this model.[12] Generally, the hard sphere model is applied to high-mass ions colliding with low-mass

neutral gases.

CRAFTI Theory. Based on the analogy between collisional broadening in drift ICR and FT-ICR, Dr. Dearden postulated that collision cross-sections could also be measured through the measurement of linewidths in FTICR-MS. Several assumptions are included in the theory. First, we assume that collisions between the ions and the neutral gas are the primary factor to broaden the linewidth. Second, we suppose that single collisions are sufficient to "dephase" the ions. We also adjust the experimental conditions so that collisions are the dominant source of broadening, which is accomplished by operating at much higher pressure than in conventional FT-ICR. We measure the variation of the peak linewidth as a function of the pressure variation. The slope of the plot of linewidth vs. pressure (neutral number density) is used in equation 4-3 to calculate collision cross sections.

$$\sigma_d(v_0) = (\xi/N)*(1/v_0)*(m+M)/M \qquad (4\text{-}3)$$

In this equation, M is the mass of the neutral gas, m is the mass of the analyte ion, and v_0 is the relative velocity of ion-neutral pair, ξ is the collision frequency and N is the number density.

The goal of this study is to explore a new method to measure collision cross sections with our instrument (FTICR-MS), which is a general-purpose mass spectrometer. The CRAFTI capability will enable FTICR-MS to provide both mass information and conformational information for macromolecules, proteins and organic polymers.

CRAFTI for positive ions. The preliminary work about applying CRAFTI to positive ions was accomplished in our group by Fan Yang. Xe was employed as the damping gas at first. The Lorentzian FWHM (full width at half maximum) of the FTICR line was plotted versus the number density which can be deduced from the neutral gas pressure. The slope of the plot was then used to calculate the cross section based on Equation 4-3. In figure 4.1, CRAFTI cross section values were plotted against theoretical values, and the linear relationship suggested that the CRAFTI method is valid with Xe collision gas.

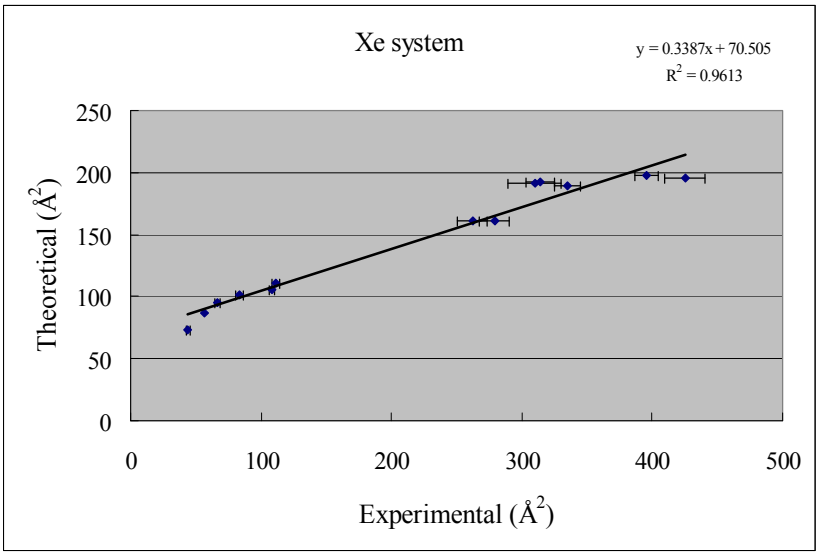

Figure 4.1: Experimental cross sections for a series of positive complexes versus their computational results in Xe[1]

Xe is not a desirable choice for collision gas because it is quite expensive. Other appropriate damping gases were tested with CRAFTI. The results for He and SF_6 are shown in Figures 4.2 and 4.3, respectively. These two figures show that the experimental cross-sections correlate poorly with theoretical results when using He as the neutral gas, whereas the correlation shows good linearity when using SF_6.

Therefore, not all gases are suitable for the CRAFTI technique. Our interpretation for the different gas results is that the molecular weight of He is much smaller than those of Xe or SF_6. The ion-neutral collisions in He might be inefficient for damping the cyclotron motion of heavy ions.

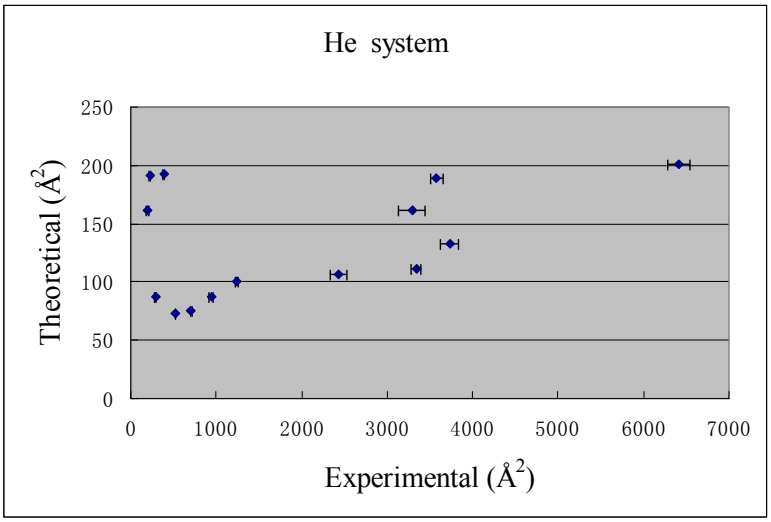

Figure 4.2: Experimental cross sections for a series of positive complexes versus their computational results in He[1]

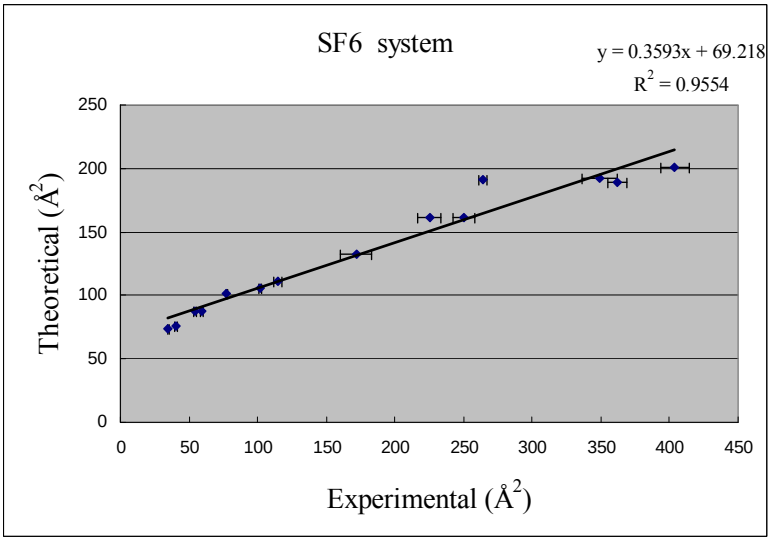

Figure 4.3: Experimental cross sections for a series of positive complexes versus their computational results in SF_6[1]

In conclusion, the data suggest the CRAFTI technique is an appropriate method for conformational studies because the experimental cross sections correlate linearly with the theoretical values. The most obvious advantage for CRAFTI compared to IMS is that we do not have to calibrate the pressure and temperature every time before use. More importantly, FT-ICR provides an accurate mass-to-charge value along with the cross section measurement, which means now we can use one technique to obtain the shape, size and mass of a molecule at the same time, instead of needing a specialized instrument to measure the mobility. The choice of the collision gas is the primary concern in CRAFTI. Up to now, two kinds of neutral gas, Xe and SF_6, have been shown to be applicable to CRAFTI while He has not.

CRAFTI for Negative Ions. The successful application of CRAFTI to positive ions encourages us to broaden the technique to negative ions. Compared to positive ions, our experience with negative ions is much less in host-guest selection, ionization, signal tuning and theoretical computation. Therefore, our current aim with negative ions is not characterizing or optimizing CRAFTI but validating the method in negative mode.

The initial problem is to select a series of negative ions with strong ESI signals suitable for cross section measurements. In positive mode, we often use decamethylcucurbit[5]uril (mc5) and cucurbiturils (CBn)[13-15] as the host molecules to bind guests because positive complexes are easily formed with mc5 and CBn. However, it is not easy for these hosts to bind negative ions due to their chemical

properties. Cyclodextrins (CDs)[16, 17] and cucurbiturils (CBn) are both important host molecules that have been extensively studied and characterized. However, CDs show distinct binding behavior compared to CBn. Cyclodextrins are cyclic sugars with a torus-like shape. The most common CDs are α, β, and γ-CD which are composed of 6, 7, and 8 glucose units, respectively. The interior cavity of CDs is relatively hydrophobic, and CD hosts can form inclusion complexes with appropriately-sized molecular guests. CD has a less symmetric geometry with one opening to the interior lined with primary hydroxyl groups; the other opening is lined with secondary hydroxyls. The hydroxyl groups that line the CD portals can also bind cations, but function both as hydrogen bond donors and as acceptors. Further, the CDs' structures are much more flexible than those of CBn, particularly on the side that consists of secondary hydroxyl groups. This feature makes the binding selectivity more diverse.

Adenosine monophosphate (AMP), also called 5'-adenylic acid, is a nucleotide that is found in DNA and RNA. AMP consists of a phosphate group, the sugar ribose, and the nucleobase adenine. AMP can be easily ionized by electrospray ionization, and a singly charged AMP anion with the strong peak at 346 is observed.

Therefore, we would like to electrospray the CDs and AMP to form a series of negative ions and measure their CRAFTI cross section.

Experimental Section

Instrument. All experiments were performed using a 4.7 Tesla Fourier transform ion cyclotron resonance mass spectrometer (Bruker, model APEX 47e). High vacuum

is provided by one stage of mechanical pumping, one stage of turbodrag pumping, two stages of diffusion pumping and one turbopumping for the final stage. The base pressure in the trapping cell is typically 1×10^{-9} mbar. The mass spectrometer is coupled with a modified commercial electrospray ionization source (model 10413; Analytica, Branford, MA) operated at atmospheric pressure. The details of the ion source modification can be found in chapter 2. Generally, the voltage applied to the spray needle is about 2.0 kV, and the spray flow rate is about 25 μL/h. Ion injection into the trapping cell is carried out via electrostatic focusing of the ion beam along the magnetic field axis. The temperature in the trapping cell is always at ambient temperature (about 300 K). Predator is the software that controls the sequence of each experiment and acquires the mass spectra. Igor Pro was used to analyze the original data file.

Materials. The concentration of host molecules (α-CD, β-CD, and γ-CD) was about 10 μM while the concentration of the guest molecules (AMP) was about 60 μM in 80% MeOH and 20% deionized water. For each 1 ml of mixed host-guest solution, 1 drop of 1 M NH_3 solution was added to help the formation of negative complexes.

All of the negative mode CRAFTI experiments were done with SF_6 as the collision gas.

Computational Methods. We usually start the calculation with Monte Carlo conformational searches, and then apply the lowest-energy conformations found in the conformational search to higher-level calculations as the starting points. The conformational searches are carried out with the *MacroModel* package (version 7.1,

Schrödinger, Inc.; Portland, OR) with the MMFF94S force field. Then the theoretical cross section was calculated using MOBCAL.[18-20]

Results and Discussion

Measurement of Cross Section using CRAFTI. The negative ions formed in electrospraying the α-CD + AMP solution are $[AMP]^-$, $[\alpha\text{-CD}]^-$, $[\alpha\text{-CD} + AMP]^-$ and $[\alpha\text{-CD} + AMP]^{2-}$. By adjusting the voltage applied on each part of the source and electrostactic focusing optics, we can control the ion strength of each negative ion. For each experiment, we choose one of the negative ions as the target ion to carry out the following experimental sequence in the ICR cell. The events included in the CRAFTI experiment are in this sequence: Initialization—Quench—Injection—SWIFT Isolation of the target negative ion—Pulsed Leak Valve—Quadrupolar Axialization (QA)—Pump down—Pulsed Leak Valve for variable Pressure—Simultaneous Excitation and Detection (SED)—Pump down.

The Quadrupolar Axilization (QA) step is built to translationally cool down the ions back to the axis of the ICR cell prior to the transient peak broadening measurement.[21, 22] However, this step usually hurts the ion strength signficantly. This is especially crucial for ions that are not in large abundance, such as the $[\alpha\text{-CD} + AMP]^-$ and $[\alpha\text{-CD} + AMP]^{2-}$ for the α-CD + AMP solution. Subsequently we found that the QA step does not have significant influence on the CRAFTI results for either positive or negative ions, so we eliminated this QA step in all negative mode CRAFTI

experiments to obtain better signal strength.

The gas pressure was varied by changing the duration of the "Pulsed Leak Valve for variable Pressure" event. A series of durations is controlled automatically and the details of the setup are shown in Table 4-1. We note that the pressure gauge does not have the same sensitivity to all kinds of gases. The standard gas used to calibrate the pressure gauge is nitrogen, so it is necessary to adjust the sensitivity value for SF_6 compared to nitrogen. The isolation step here is still SWIFT isolation, which is used to isolate the mono isotopic peak from the target ion. The reason for isolating the monoisotopic peak is to prevent peak broadening caused by overlap with other isotopic peaks.

Simultaneous excitation and detection (SED[23, 24]) permits observation of ion motion during an excitation event. In the excitation event, neutral-ion collisions take place, so real-time detection can reflect the extent of collisions during excitation. In SED spectra, we observe a narrow peak superimposed on the wide excitation band. When the signal strength gets weaker and weaker, the narrow peak disappears and is hidden under the excitation band. For each target ion, we need to choose the proper excitation amplitude range. If the amplitude is too small, ions are not coherently excited, so the detected signal is weak. If the amplitude is too large, the ions are ejected from the trap.

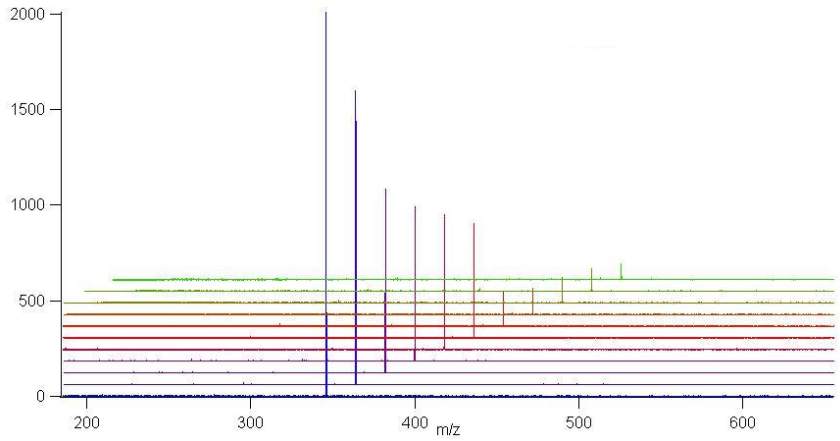

Figure 4.4: Mass spectra of $[AMP]^-$ under different SF_6 gas pressures

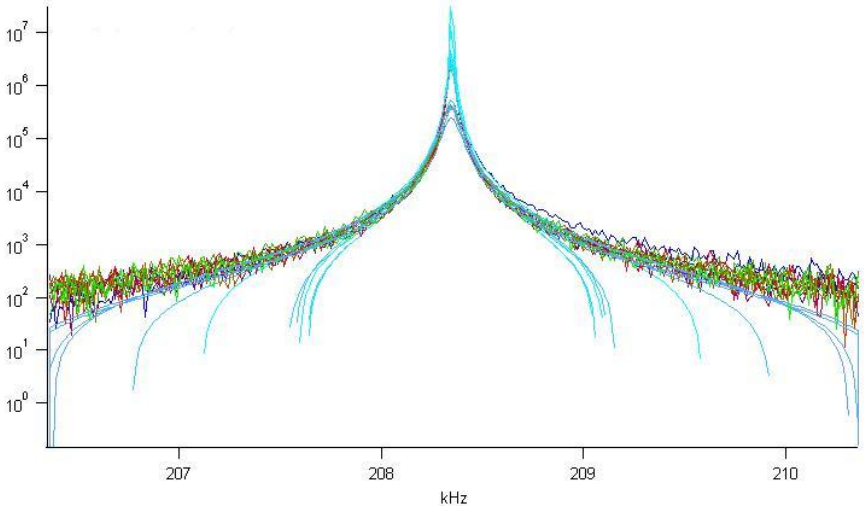

Figure 4.5: Lorentzian linewidth broadening with increasing pressure for $[AMP]^-$

(The light blue curves are Lorentzian fits to the experimental data.)

Data Processing. We use the negative ion $[AMP]^-$ as an example to show how we process the mass spectral data to measure the collision cross section of $[AMP]^-$. In figures 4.4 and 4.5, we observe that the signal strength of the monoisotopic peak belonging to $[AMP]^-$ deceases and the linewidth of the monoisotopic peak broadens with increasing SF_6 pressure. At different neutral gas pressures, the collision

frequency between the neutral gas ions and target ions is changed. According to equation 4-3, we need to obtain the collision frequency change rate from the experimental result to calculate the cross section. As I have mentioned above, we assume that the broadening is mainly caused by collisions between the neutral gas and the target ions. We also assume that a single collision is sufficient to cause one target ion to dephase. The higher the pressure of neutral gas, the more dephasing occurs, and the weaker the signal strength and the wider the peak linewidth become.

Table 4-1: Variation of Lorentzian linewidths by increasing the valve time for $[AMP]^-$

Scan Number	Valve Time (sec)	Pressure (mbar)	Number density (cm^{-3})	Lorentzian FWHM (Hz)
1	0.002	6.00E-08	2.16E+09	6.3
2	0.005	1.20E-07	4.33E+09	16.7
3	0.007	6.00E-07	2.16E+10	39.8
4	0.01	1.00E-06	3.61E+10	63.5
5	0.012	1.20E-06	4.33E+10	78.9
6	0.014	1.40E-06	5.05E+10	93.7
7	0.016	1.60E-06	5.77E+10	116.0
8	0.018	1.90E-06	6.85E+10	131.6
9	0.02	2.20E-06	7.93E+10	144.6
10	0.022	2.60E-06	9.38E+11	160.9
11	0.026	3.20E-06	1.15E+11	188.4
12	0.03	3.80E-06	1.37E+11	238.8

The Igor Pro program was used to fit the frequency domain peak to a Lorentzian peak shape, shown in Figure 4.5, so we can accurately obtain the Lorentzian FWHM (full width at half maximum). The FWHM value was then plotted versus the number density which was deduced from the gas pressure. Figure 4.6 is the plot of Lorentzian linewidths for $[AMP]^-$ versus the SF_6 number density. The linewidth increases linearly

with number density, which is consistent with the old results from drift ICR.[3] The slope of the plot can be applied in equation 4-3 to calculate the cross section.

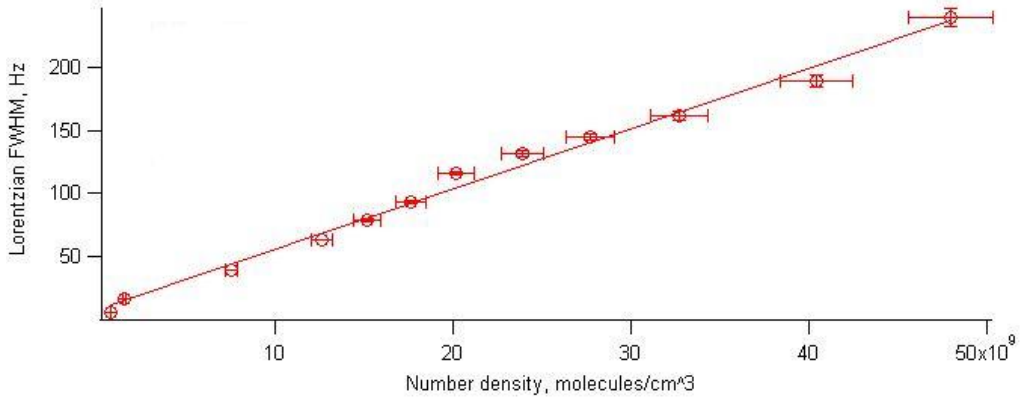

Figure 4.6: Variation of Lorentzian linewidths with change of neutral gas number density for $[AMP]^-$

We also electrosprayed β-CD + AMP solution and γ-CD + AMP solution, and the following negative ions were obtained from the corresponding solutions: $[AMP]^-$, $[\beta\text{-CD}]^-$, $[\beta\text{-CD} + AMP]^-$, $[\beta\text{-CD} + AMP]^{2-}$, $[\gamma\text{-CD}]^-$, $[\gamma\text{-CD} + AMP]^-$ and $[\gamma\text{-CD} + AMP]^{2-}$. For the doubly charged complexes, the signals get quite weak after increasing the gas pressure. Therefore we can not observe their Lorentzian linewidth broadening as the pressure increases. The experimental results are listed in table 4-2 for all the ions whose cross sections could be measured. The computational results for cross sections of the same ions are also shown in table 4-2.

Table 4-2: Experimental and Computational Cross Sections of Negative Ions ($Å^2$)

Negative ions	Experimental cross section	Computational cross section
$[AMP]^-$	155.0 ± 8.7	107.6 ± 3.1
$[\alpha\text{-CD}]^-$	626 ± 22	218.3 ± 4.9
$[\beta\text{-CD}]^-$	754 ± 32	251.7 ± 5.3
$[\gamma\text{-CD}]^-$	838 ± 27	284.4 ± 5.8
$[\alpha\text{-CD} + AMP]^-$	781 ± 49	276.7 ± 9.1
$[\beta\text{-CD} + AMP]^-$	886 ± 31	296.1 ± 7.1
$[\gamma\text{-CD} + AMP]^-$	1013 ± 47	329.8 ± 15.8

Discussion. The results above show that the experimental collision cross sections of these negative ions are much larger than the computational values. That means some of the factors that influence the cross section measurement have not been accounted for in the CRAFTI experiment. What's more, the errors in the experimental results are relatively large, so we need to improve the experimental accuracy, probably by measuring the pressures more accurately and by working with stronger signals. However, we can check the validity of negative mode CRAFTI by plotting the experimental results for a series of complexes versus theoretically computed cross sections values for those complexes, in a manner analogous to what was done earlier for positive ions.

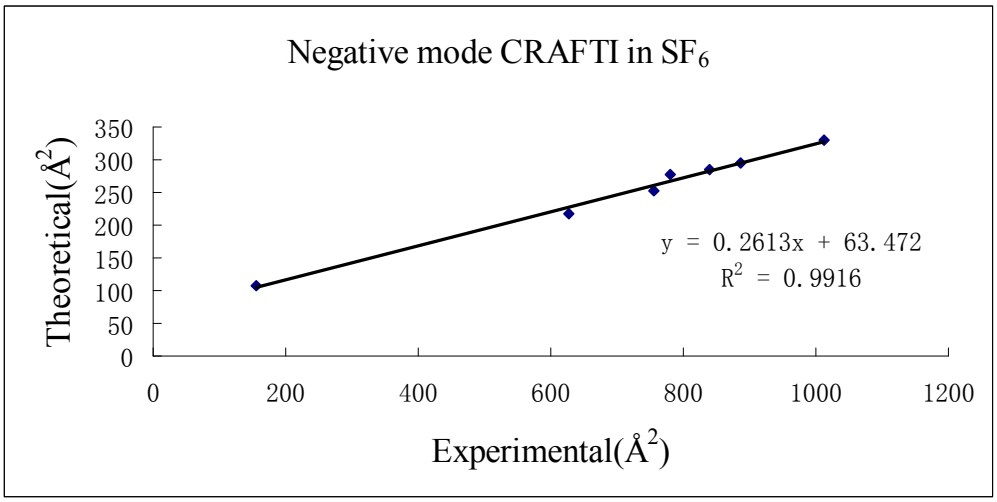

Figure 4.7: Experimental cross sections for negative complexes compared with computational results in SF_6

Figure 4.7 shows a good linear relationship between the experimental results and the theoretical results for the same negative ions. Therefore, the negative mode CRAFTI appears promising as a method to measure collision cross sections for negative ions. However, before we apply this method to additional negative ions, we need to better understand the factors that cause the big differences between the theoretical values and experimental values. Although we compare the theoretical results and experimental results, we didn't expect the good numerical agreement between CRAFTI cross sections and hard sphere collision cross sections calculated for collisions in He, which is what we obtain from MOBCAL, We also know that ion dissociation is a large contributor to CRAFTI cross sections so we expect them to be larger than the MOBCAL values.

The errors in the experimental results might come from the neutral gas. As we have shown in positive mode CRAFTI, He was an inappropriate neutral gas because

He is too light to provide efficient dephasing for heavier ions in a single collision. Herein, the molecular weight for $[\gamma\text{-CD} + \text{AMP}]^-$ is 1643.5, much larger than the mass of SF_6, which is 146. It's possible that SF_6 is also too light to cause efficient dephasing in a single collision for these heavier ions.

Conclusion

Based on the fact that the experimental cross sections correlate linearly with the theoretical values, we have obtained evidence that CRAFTI is an appropriate method for negative ions. However, there are still some problems left in this method. The first one is the system factors that influence the experimental values of each negative ion, such as the pressure reading, the assumptions used in the model which we used to calculate the results. The second problem is the relatively high experimental errors. We need to carefully tune the excitation amplitude and the isolation amplitude to make the signal strong and monoisotopic for some weak ions. CRAFTI is a very promising and attractive method because FT-ICR provides accurate mass-to-charge measurement along with the cross section measurement. That is to say one technique is enough to obtain the shape, size and mass of a molecule simultanously.

References

(1) Dearden, D. V.; Yang, F. *57th ASMS Conference on Mass Spectrometry and Allied Topics*; ASMS: Philadelphia, PA, **2009**.

(2) Herbert, H.; William, F.; Robert, H.; *Anal. Chem.* **1990,** *62*, 1201A-1209A.

(3) Valentine, S. J.; Counterman, A. E.; Clemmer, D. E. *J. Am. Soc. Mass Spectrom.* **1999**, *10*, 1188–1211.

(4) Rusyniak, M. J.; Ibrahim, Y. M.; Wright, D. L.; Khanna, S. N.; El-Shall, M. S. *J. Am. Chem. Soc.* **2003**, *125*, 12001-12013.

(5) Covey, T.; Douglas, D. J. *J. Am. Soc. Mass Spectrom.* **1993**, *4*, 616-623.

(6) Ring, S.; Naaman, R.; Rudich, Y. *Anal. Chem.* **1997,** *71*,648-651.

(7) Davis, E. J.; Dwivedi, P.; Tam, M.; Siems, W. F.; Hill, H. H. *Anal. Chem.* **2009,** *81*, 3270-3275.

(8) Chen Y. L.; Collings B.A.; Douglas D.J. *J. Am. Soc. Mass Spectrom.* **1997**, *8*, 681-687.

(9) Beauchamp J. L. *J. Chem. Phys.* **1967**, *46*, 1231-1244.

(10) Marshall, A. G.; Hendrickson, C. L.; Jackson, G. S. *Mass Spectrom. Rev.* **1998**, *17*, 1-35.

(11) Guan S. H.; Li G. Z.; Marshall A. G. *Int. J. Mass Spectrom and Ion Pro.* **1997**, *167/168*, 185-193.

(12) Vining, B. A.; Bossio, R. E.; Marshall, A. G. *Anal. Chem.* **1999,** *71*,460-467.

(13) Mock, W. L. In *Comprehensive Supramolecular Chemistry;* F. Vögtle, Ed.; Elsevier: New York, 1996; Vol. 2; pp. 477-493.

(14) Lagona, J.; Chakrabarti, S.; Isaacs L. *Angew. Chem. Int. Ed.* **2005**, *44*, 4844-4870.

(15) Kim, J.; Jung, I.-S.; Kim, S.-Y.; Lee, E.; Kang, J.-K.; Sakamoto, S.; Yamaguchi, K.; Kim, K. *J. Am. Chem. Soc.* **2000**, *122*, 540-541.

(16) Bender, M. L.; Komiyama, M. *Cyclodextrin Chemistry*; Springer-Verlag: Berlin, 1978.

(17) Szejtli, J.; Osa, T., Ed.; Elsevier: Oxford, 1996; Vol. 3.

(18) Mesleh, M. F.; Hunter, J. M.; Shvartsburg, A. A.; Schatz, G. C.; Jarrold, M. F. *J. Phys. Chem.* 1996, *100*, 16082-16086

(19) Shvartsburg, A. A.; Jarrold, M. F. *Chem. Phys. Lett.* 1996, *261*, 86-91

(20) Shvartsburg, A. A.; Pederson, L. A.; Hudgins, R. R.; Schatz, G. C.; Jarrold, M. F. *J. Phys. Chem. A* **1998**, *102*, 7919-7923.

(21) Guan, S.; Kim, H. S.; Marshall, A. G. *Chem. Rev.* **1994**, *94*, 2161-2182.

(22) Hendrickson, C. L.; Drader, J. J.; Laude, D. A. *J. Am. Soc. Mass Spectrom.* **1995**, *6*, 448-452

(23) Beu, S. C. In *46th ASMS Conference on Mass Spectrometry and Allied Topics*; Orlando, FL, 1998.

(24) Beu, S. C.; Blakney, G. T.; Quinn, J. P.; Hendrickson, C. L.; Marshall, A. G. *Anal. Chem.* **2004**, *76*, 5756-5761.

Chapter 5

Gas Phase Chiral Recognition in Cucurbituril Cavities

Introduction

Cucurbiturils (CB) are pumpkin-shaped macrocycles that are cyclic polymers of glycoluril (see figure 5.1).[1] Although the first cucurbituril molecule was synthesized in 1905, it was not until 1981 that the chemical nature and structure were fully characterized by Mock and co-workers. In the past, receptors such as cyclodextrins, crown ethers and calixarenes have been well developed in host-guest chemistry.[2,3] In recent years, more and more interest has turned to the cucurbituril family due to its rigid structure, wide size range and high binding selectivity.[4-10] Cucurbiturils can selectively bind amines, cations and neutral molecules through noncovalent interactions at the two portals or inside the cavity.[11-13] For instance, Dearden et al. have shown that alkyldiammonium ions form pseudorotaxanes with CB6 in the gas phase using electrospray FTICR mass spectrometry.[14]

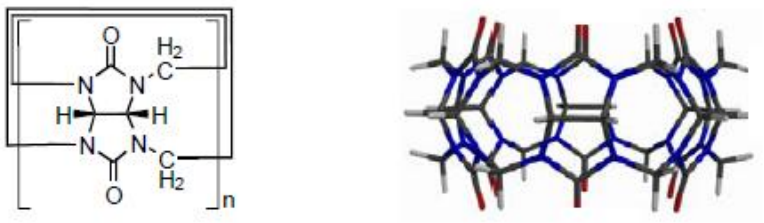

Figure 5.1: Chemical structure of the cucurbit[n]uril macrocycle[1]

Cucurbiturils are achiral molecules, and this property naturally restrains their application in chiral recognition. Recently, a study has been done to induce chirality

into achiral cucurbiturils by introducing chiral ligands into the cucurbituril architecture.[15] Rekharsky and co-workers have proven that CB[6] or CB[7], bound to a chiral ligand, can be used as an effective chiral discriminator in solution. They found that (S)-2-methylbutylamine can be discriminated by two enantiomeric supramolecular hosts, composed of CB[6] and (*R*)- or (*S*)-2-methylpiperazine, with an unprecedented 95% enantioselectivity in aqueous NaCl solution (see figure 5.2). Similarly, CB[7], with a larger cavity, exhibited diastereoselectivities up to 8 times higher for diastereomeric dipeptides, as demonstrated for L-Phe-L-Leu-NH_3 versus L-Phe-D-Leu-NH_3. This is the highest enantioselectivity ever reported for a supramolecular system derived from an achiral host.[15]

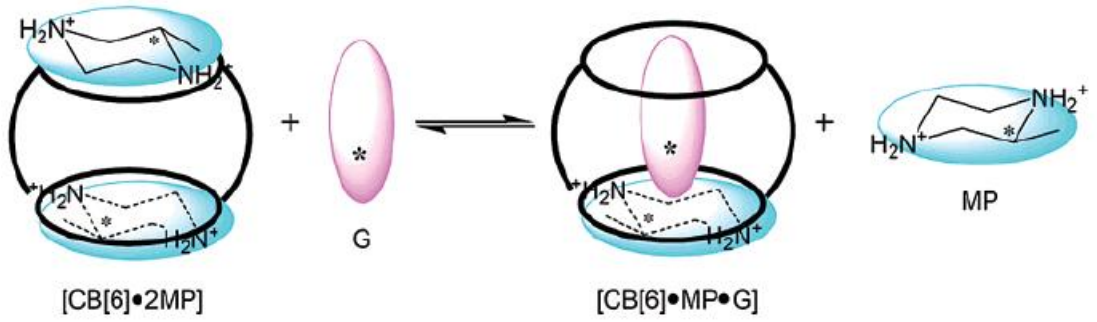

Figure 5.2: Replacement of 2- methylpiperazine (MP) auxiliary by another chiral guest, such as 2-methylbutylamine or sec-butylamine.[15]

Their work indicates that an inherently chiral host is not necessarily required for chiral recognition in solution phase. A combination of achiral host (CB) and chiral inductor can also function as a supramolecular chiral discriminator, where the chiral recognition ability may be tuned by choosing the chiral inductor.[15]

Our group has long been interested in investigating gas phase chiral recognition

in macrocycles via noncovalent interactions.[16,17] Much background has been given in chapter 2, which relates to chiral recognition with chiral hosts. Rekharsky's work shows successful chiral recognition using an achiral host in solution, which inspired us to think about the possibility of applying CBs as chiral recognition containers in the gas phase. Conferring chirality on cucurbiturils makes the chiral recognition happen in a restricted space, which might strengthen or hinder the discrimination. By comparing our results with Rekharsky's, we hope to see the role of solvent in this chiral recognition process.

The key point is to find the right size cucurbituril and corresponding chiral ligands/auxiliaries that give high enantiodiscrimination. Cucurbit[6]uril (CB6) is the most common molecule in the cucurbituril family. It has a hydrophobic cavity with a diameter of 5.8 Å, accessible via two carbonyl-lined portals of 3.9 Å diameter. Our past work showed that CB6 is a suitable host for amines, so we will start with CB6 to find the proper combination of chiral ligands and auxiliaries.

With computational modeling like B3LYP/6-31G* geometry optimization and energy calculation, we should be able to predict whether the system results in high enantiodiscrimination or not. These predictions will guide us in the search for effective chiral discriminators.

In the past, we have tried to use amino acids as auxiliary molecules to confer chirality on CB[6]. Lysine forms a doubly-protonated 1:1 inclusion complex with cucurbit[6]uril in the gas phase, and the complex reacts with (*S*)-cyclohexylethylamine via adduction. Experimental results showed that there is no

enantiodiscrimination associated with this adduction reaction. The computational results indicate that cyclohexylethylamine approaches CB[6] on the opposite side of CB6 from the Lys stereocenter, so the two stereocenters on L-lysine and (*S*)-cyclohexylethylamine respectively are not close enough to promote enantiodiscrimination.

In Rekharsky's study, 2-methylpiperazine (MP) seemed to be a very promising chiral ligand for CB[6] in solution. In our experiment, two MP molecules strongly bind CB[6] at the two portals and a very stable doubly-charged complex is formed via electrospray ionization. In this case, no matter which side of the complex is approached by a chiral amine in an exchange reaction, the chiral amine must closely approach the MP molecule for the exchange reaction to occur, suggesting good enantiodiscrimination might be possible.

Experimental Section

Materials. Cucurbit[6]uril (CB[6]), 2-methylpiperazine (MP), (*S*)-2-methylbutylamine (MB), (*S*)-*sec*-butylamine (BA), propylamine (PA), (*S*)-cyclohexylethylamine (CHE), (*S*)-N, α-dimethylbenzylamine (DBA) and L-lysine were purchased from Sigma Chemical Co. (St. Louis MO) and used without further purification. Formic acid was purchased from Fisher Scientific (Fair Lawn, NJ). HPLC grade water and methanol were purchased from Mallinckrodt Baker Inc. (Phillipsburg, NJ).

Sample Preparation. 5×10^{-4} CB[6] stock solution was prepared by dissolving

solid sample in a 7:3 formic acid/methanol mixture. MP was dissolved in pure methanol. Electrospray solutions were prepared by mixing CB[6] with (*R*)-MP or (*S*)-MP directly from the stock solutions with the ratio of 1:2, and then diluting the mixture with 50:50 water/methanol solvent to a concentration of 5×10^{-5} M in CB[6]. CB[7] can be easily dissolved in 50:50 water/methanol solvent without using strong acid.

Instrument. Mass spectrometric measurements were carried out using a Bruker model APEX 47e FT-ICR mass spectrometer controlled by a Predator data system.[18,19] The mass spectrometer is coupled with a modified commercial electrospray ionization source[20] (Model 10413; Analytica, Branford, MA) operated at atmospheric pressure.

Reactivity Experiments. CB[n]-based complexes were generated by electrospraying a mixture of cucurbituril and one enantiomer of auxiliary compound (MP) into the instrument. In addition, one enantiomer of another chiral guest was introduced into the trapping region of the instrument to constant partial pressure via a controlled variable leak valve. The reaction time (between SWIFT isolation[21] of the ionic reactant and detection of reactants and products) was varied programmatically. Data analysis was performed with a modified version of the MIDAS Analysis software that was capable of extracting peak amplitudes from a set of spectra that differ in one or more experimental parameters (in this case, reaction time).

Basically, we discriminate between enantiomers by their reaction rate differences or their free energy change differences associated with the exchange reaction, adduction reaction or dissociation reaction. Since we are going to use a mass

spectrometer to measure the abundance of reactants or products, they must differ in mass. Otherwise, the mass spectrometer can not quantify the reaction.

SORI-CID Experiments. We use stored waveform inverse Fourier transform (SWIFT) techniques[21] to isolate target peaks. Sustained off-resonance irradiation collision-induced dissociation (SORI-CID) experiments[22] were performed by irradiating 1 kHz below the resonant frequency of the ion of interest. Collision gas (air) was introduced using a Freiser-type pulsed leak valve.[23] SORI events involved pulsing the background pressure in the trapping cell up to 10^{-5} mbar and applying the off-resonance irradiation for 5 seconds, followed by a 10 second delay to allow the trapping cell to return to baseline pressure (about 10^{-8} mbar) prior to detection. The amplitude of the SORI RF pulse was varied through a range of values from less than the threshold for dissociation to several times the threshold value.

Results and Discussion

Computational results show that CB[6] has a more appropriate cavity size for binding 2-methylpiperazine (MP) than either CB[5] or CB[7], therefore we started the investigation with the system containing CB[6] and MP. Electrospray ionization of a mixture of CB[6] and MP yields a prominent doubly-charged ion corresponding to $[CB[6]•2MP+2H]^{2+}$. We introduced achiral propylamine (PA pressure: 1.4×10^{-5} mbar) into the hexapole region of the electrospray source and let it react with $[CB[6]•2MP+2H]^{2+}$ to form a ternary complex $[CB[6]•MP•PA+2H]^{2+}$, which is then injected into the FTICR trapping cell. In the cell, the ternary complex readily exchanges neutral PA for neutral (*S*)-BA, which showed that PA is more easily

displaced by BA than is MP. The experimental results indicated no enantiodiscrimination occurred in the exchange reaction (Figure 5.3) because both the reaction rate constant and the reactant/product ratio are the same for the (*R*)-MP system and (*S*)-MP system, which means the equilibrium constants are the same in both systems. When exchange occurs, (S)-BA likely approaches CB[6] from the side on which the achiral PA is attached. During the exchange process, the stereo center in (*S*)-BA is evidently far away from the stereo center of MP, so no enantiodiscrimination was observed.

(*R*)-MP

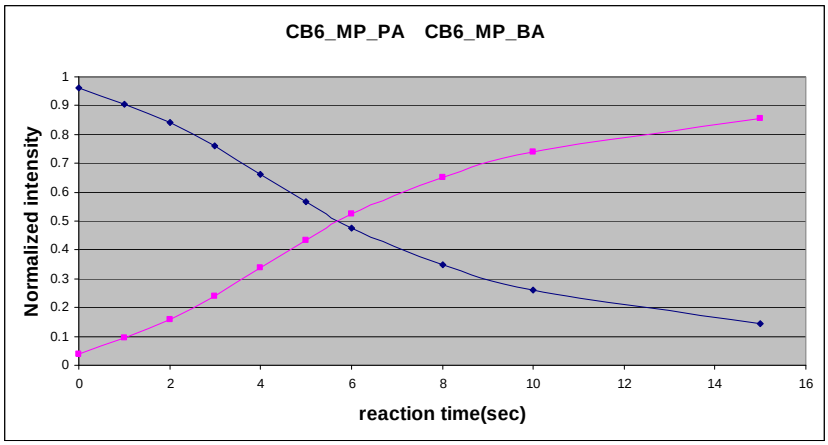

(*S*)-MP

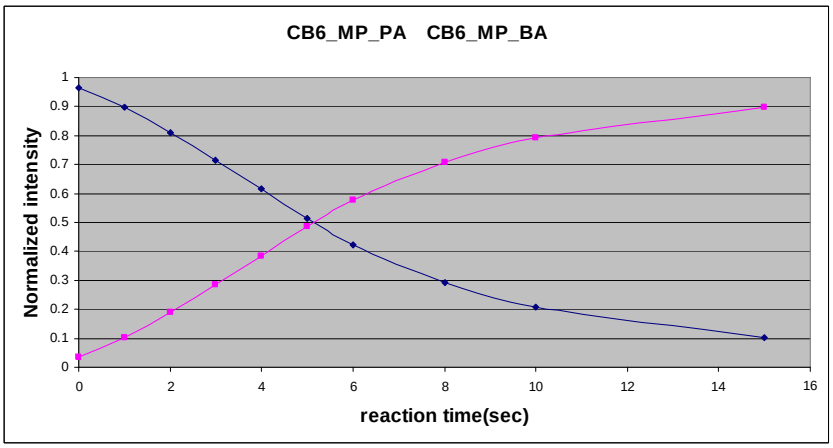

Figure 5.3: Exchange reaction associated with CB[6], MP, PA and (S)-BA

Next we let the $[CB[6]\bullet 2MP+2H]^{2+}$ complex exchange with neutral (*S*)-BA in the trapping cell to produce a ternary complex (Figure 5.4). We observed that formation of the (*R*,*S*)-$[CB[6]\bullet MP\bullet BA]^{2+}$ complex is faster than formation of the analogous (*S*,*S*) homochiral diastereomer. Because the reactions haven't reached equilibrium, we determined the equilibrium constant from the ratio of the rate constants for the forward and reverse reactions, respectively (see figure 5.5). We collected enough data at short reaction times to make sure the kinetic fit gave accurate rate constants.

(*R*)-MP

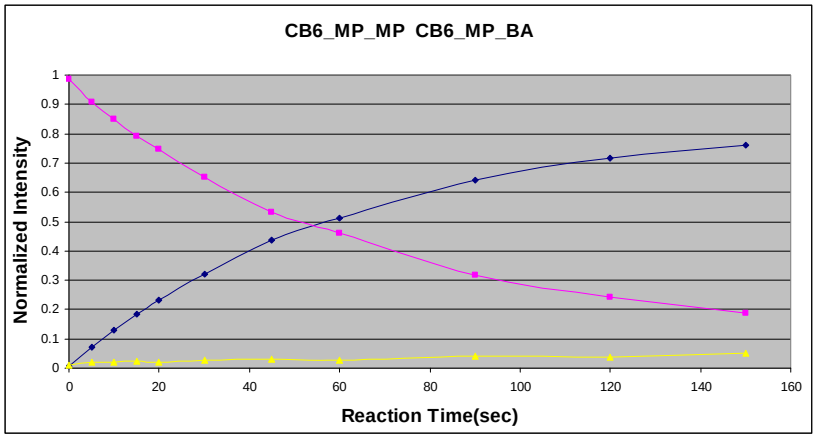

(*S*)-MP

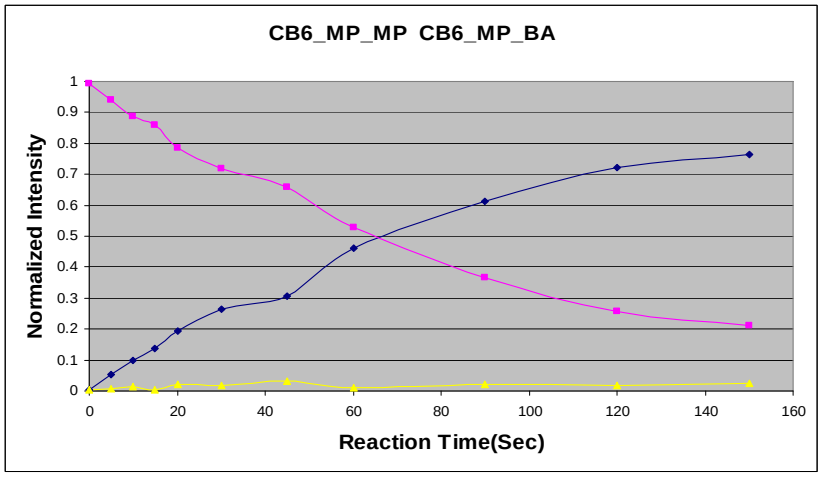

Figure 5.4: Exchange reaction associated with CB[6], MP and (S)-BA

(*R*)-MP

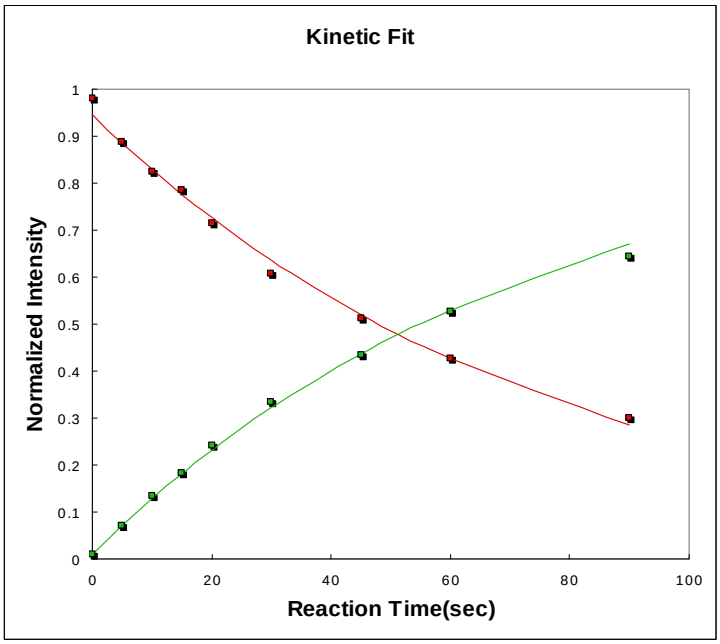

(*S*)-MP

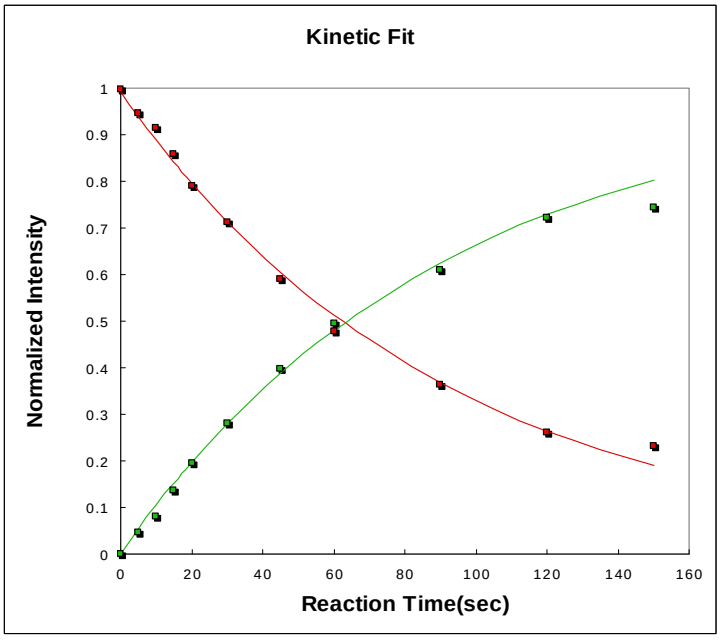

Figure 5.5: Kinetic fit results for exchange reaction associated with CB[6], MP and (S)-BA. The red dots represent the CB6_MP_MP complex, and the green dots represent the CB6_MP_BA complex.

The exchange reactions were repeated three times for the (*R*)-MP and (*S*)-MP alternatively to make sure the result is reproducible. The equilibrium constant are listed in table 5-1. The data in table 5-1 shows that (*R*,*S*)-[CB[6]•MP•BA]$^{2+}$ complex is 13% more stable than the analogous (*S*,*S*) homochiral diastereomer.

Table 5-1: Equilibrium constants for (*R*)-MP and (*S*)-MP systems

	1 st	2 nd	3 rd	mean
K_{eq} of (*R*,*S*)-[CB[6]•MP•BA]$^{2+}$	0.0133	0.0119	0.0104	-
K_{eq} of (*S*,*S*)-[CB[6]•MP•BA]$^{2+}$	0.0110	0.0105	0.00982	-
K_{eq} ratio of (*R*,*S*)/ (*S*,*S*)	1.20	1.13	1.06	1.13

Based on the published results from solution data, we expect (*S*)-2-methylbutylamine (MB) to result in greater enantiodiscrimination than that was observed for BA. The stereo center is located α to the ammonium group in BA, however it is in the β position in MB. Therefore, the stereo center of MB will be forced to penetrate more deeply into the cucurbituril cavity, imparting chirality in a more restricted space than in the BA complex. However, the experimental result showed no enantiodiscrimination in the gas phase (Figure 5.6).

Other than (*S*)-2-methylbutylamine (MB), I also tried (*S*)-cyclohexylethylamine (CHE) and (*S*)-N, α-dimethylbenzylamine (DBA). Compared to MB, CHE has a bulky group and DBA is a secondary amine. They might slow down the fast exchange reaction, so the enantiodiscrimination effect might be enlarged enough to be observed.

However, the experimental result showed no enantiodiscrimination for either CHE or DBA (Figure 5.7 and 5.8).

(*R*)-MP

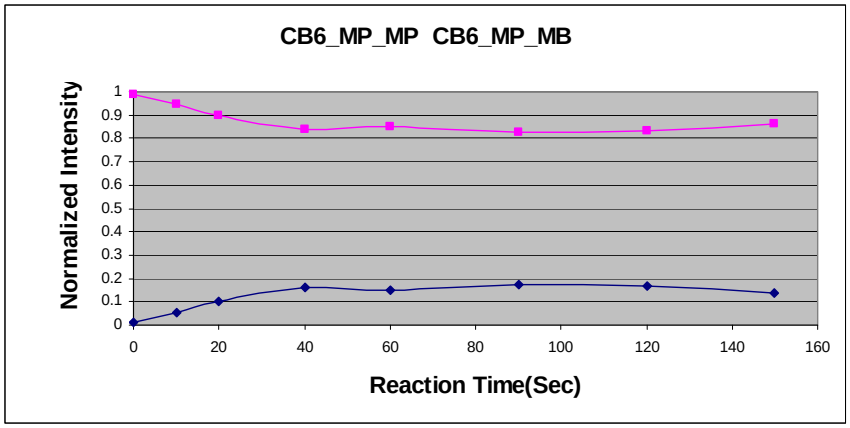

(*S*)-MP

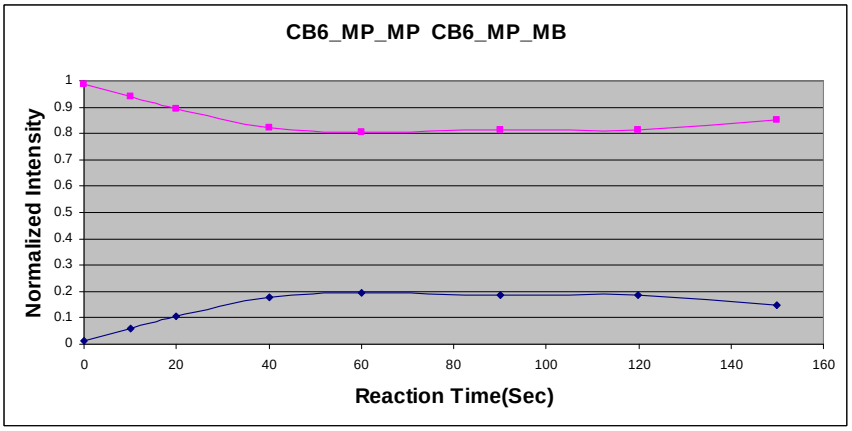

Figure 5.6: Exchange reaction associated with CB[6], MP and (S)-MB

(*R*)-MP

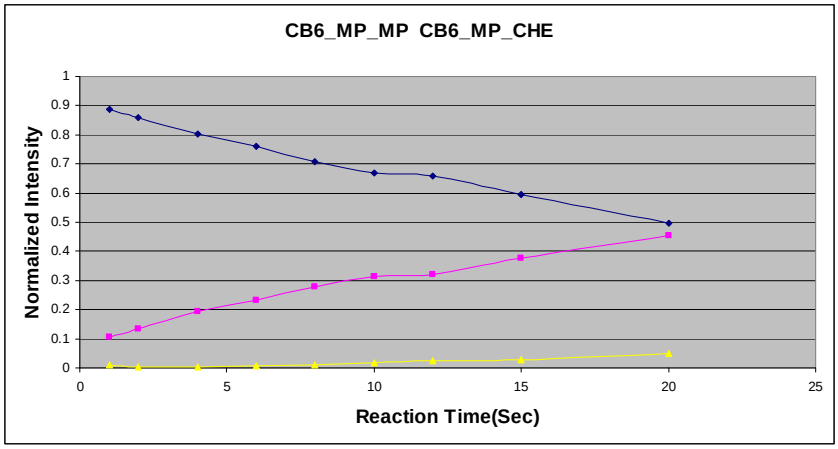

(*S*)-MP

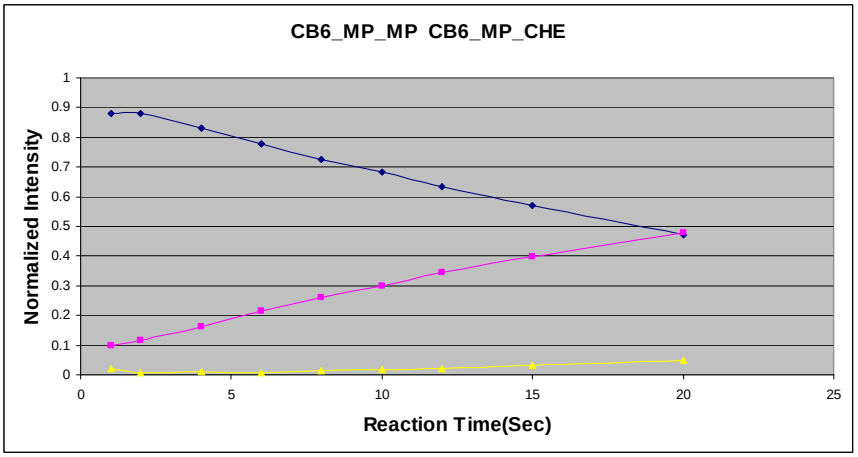

Figure 5.7: Exchange reaction associated with CB[6], MP and (S)-CHE

(*R*)-MP

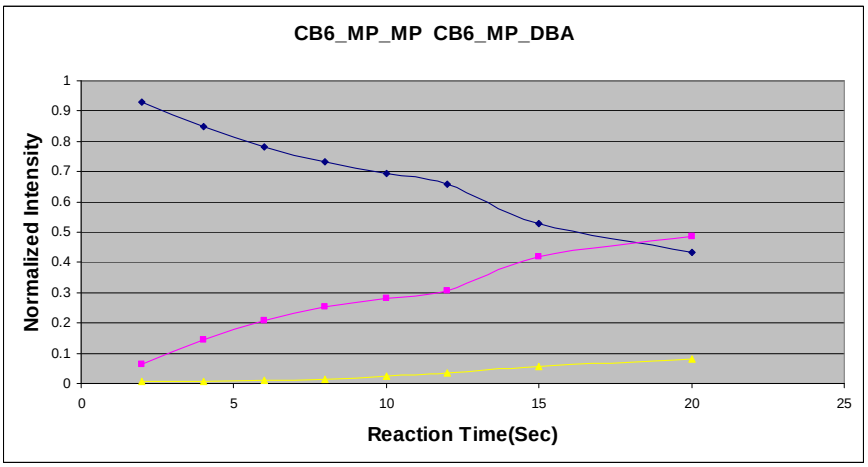

(*S*)-MP

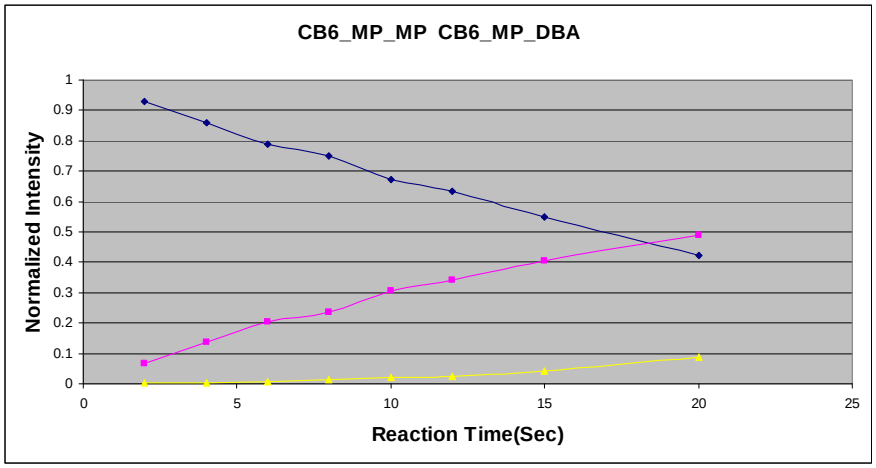

Figure 5.8: Exchange reaction associated with CB[6], MP and (S)-DBA

Another experiment I carried out is forming the ternary complex [CB[6]•MP•(*S*)-BA+2H]$^{2+}$ by attaching two chiral amines to the two portals of CB[6]. In the trapping cell, the ternary complex exchanged neutral (*S*)-BA for neutral (*S*)-CHE. The experimental result again showed no enantiodiscrimination in the exchange reaction (Figure 5.9).

(*R*)-MP

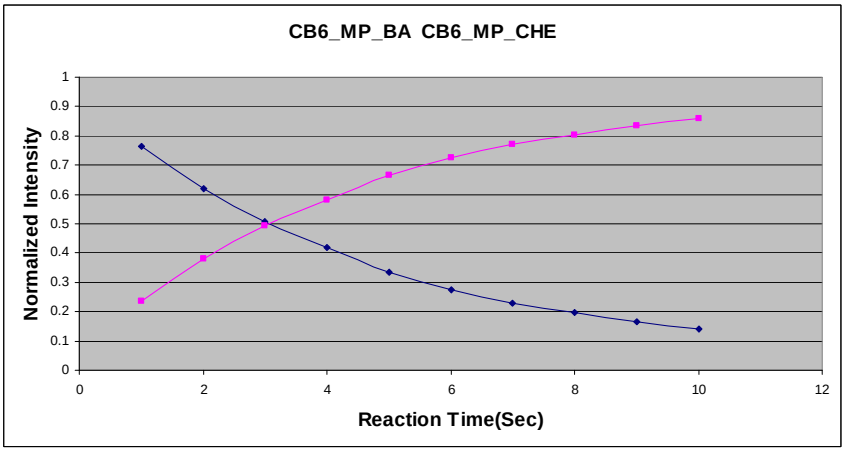

(*S*)-MP

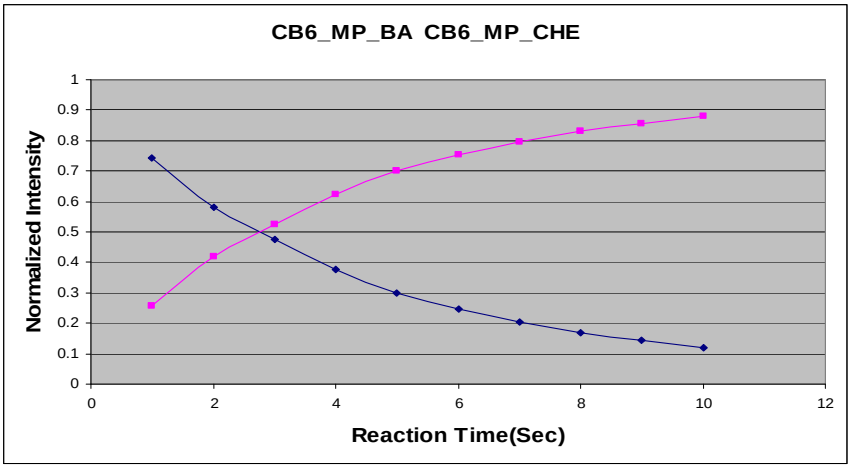

Figure 5.9: Exchange reaction associated with CB[6], MP, (*S*)-BA and (*S*)-CHE

As for CB[7], it has a larger cavity than CB[6] in both portal diameter and cavity width. I observed that the [CB[7]•MP•(*S*)-BA+2H]$^{2+}$ complex was formed in less than 1 second (much faster than was the case for CB[6]). Therefore I performed sustained off-resonance irradiation (SORI) collision-induced dissociation experiments on this complex to compare the stability of the two ternary complexs (Figure 5.10).

(R)-MP

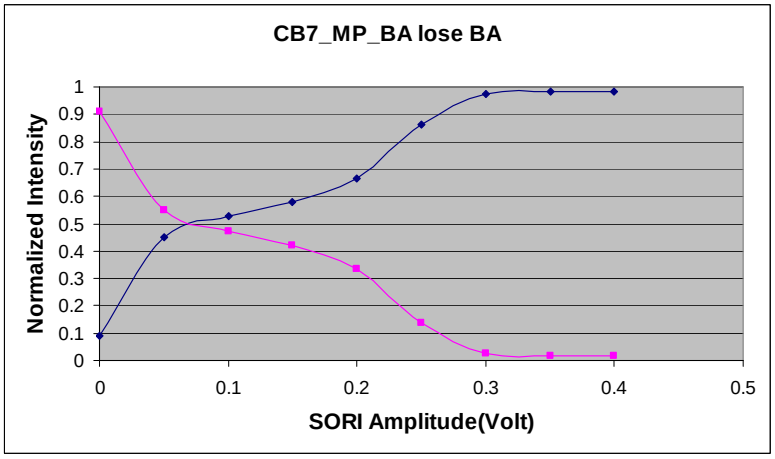

(S)-MP

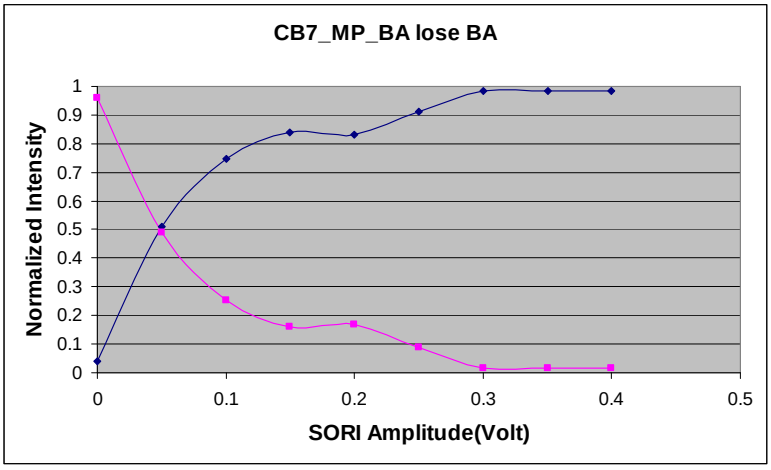

Figure 5.10: Dissociation reaction associated with CB[7], MP and (S)-BA

The dissociation for both diastereomers is complete at an amplitude of 0.3 volts (figure 5.10) with the diastereomers losing BA. However, the dissociation curves for the (*R*,*S*)-[CB[7]•MP•BA]$^{2+}$ complex and the (*S*,*S*)-[CB[7]•MP•BA]$^{2+}$ complex are not exactly the same. For instance, about 50% of the heterochiral diastereomer loses BA at 0.1 volt, whereas nearly 80% of the homochiral diastereomer loses BA at the same SORI amplitude. Therefore, the heterochiral diastereomer is more stable than the homochiral diastereomer. This conclusion is consistent with the Rekharsky's result in solution.

From the experimental results above, it is clear that chiral recognition of guests by achiral hosts (CBs) in the gas phase is not as good as was observed in solution. One possible explanation is that the exchange reaction mechanism is not the same for solution and the gas phase. In Rekharsky's study, the thermodynamic parameters for the complexation of chiral auxiliary (*S*)-MP with CB[6] in solution indicate optimal position at the CB portals. NMR studies provide strong evidence to indicate partial

insertion of chiral MP into the CB[6] cavity. Therefore, it is likely that MP's hydrophobic methyl substituent is included inside the CB[6] cavity. After the replacement of one MP by a stronger chiral binder, such as BA or MB, the chiral binder is small enough to penetrate deeper into the CB[6] cavity, so both the stereo center of MP and the stereo center of the stronger chiral binder are accommodated insider the cavity. Thus high enantioselectivity in the assembled complex can be observed in the solution phase. That is to say the enantiodiscrimination does not happen between the "leaving" MP and the "approaching" stronger chiral binder, but occurs between the MP that remains with the complex and the approaching chiral binder. In the gas phase, the complex is isolated, no solvent molecules surround the CBs, hydrophobic effects are absent, and it is possible that the MP's hydrophobic methyl substituent and the stronger chiral binder might not be simultaneously included inside the cavity. The dissociation experiment for the CB[7] ternary complex shows that the dissociation amplitude for losing BA (the stronger chiral binder) is only 0.3 volts. This small value suggests that BA binds externally to the CB[7]. Because the stereo centers on the MP and on the stronger chiral binder are not close enough to each other in the gas phase, we observed no enantiodiscrimination for most of our experiments. Our results in the gas phase further suggest that the enantiodiscrimination does not happen between the "leaving" MP and the "approaching" stronger chiral binder. We designed several cases for close distance between the "leaving" MP and the "approaching" stronger chiral binder, however, we could not observe any chiral recognition.

Conclusions

The CB[6], 2-methylpiperazine (MP) and (*S*)-sec-butylamine (BA) system showed an average 13% enantiodiscrimination in the gas phase. 2-methylbutylamine (MB) did not result in greater enantiodiscrimination, in contrast with observations in solution. MP is a proper auxiliary chiral molecule for CB[6], because it binds to CB[6] with appropriate strength. The gas phase environment is not favorable for accommodating stereo centers inside the CB cavity, which is apparently necessary for induction of enantiodiscrimination in achiral CBs. Gas phase chiral recognition does not happen between the "leaving" auxiliary group and the "approaching" stronger chiral binder. To enable high induced enantioselectivity to occur with achiral hosts (CBs) in gas phase, we need to choose the proper CB molecule that can contain the stereo center of the chiral auxiliary as well as that of the stronger chiral binder.

As for the [CB[7]•MP•BA] ternary complex, the dissociation curves suggest the heterochiral diastereomer is more stable than the homochiral diastereomer. This conclusion is consistent with the Rekharsky's result in solution phase. We cann't carry out the exchange experiment here because the reaction rate is too fast (in less than 1 second). The calculation result showed that $[CB6+MP]^{2+}$ is more stable than $[CB7+MP]^{2+}$ because MP fits the CB6 cavity size better than the CB7 cavity size. Therefore, we have to look for more proper auxiliary binder for CB7 system.

References

(1) Freeman, W. A.; Mock, W. L.; Shih, N.-Y. *J. Am. Chem. Soc.*, **1981**, *103*, 7367.

(2) Cram, D. J.; Cram, J. M. *Science* **1974**, *183*, 803-809.

(3) Schneider, H. J. *Angew. Chem. Int. Ed. Engl.* **1991**, *30*, 1417-1436.

(4) Buschmann, H.-J.; Cleve, E.; Jansen, K.; Wego, A.; Schollmeyer, E. *J. Inclusion Phenom. Macrocyclic Chem.* **2001**, *40*, 117-120.

(5) Mock, W. L. In *Comprehensive Supramolecular Chemistry*; Vogtle, F., Ed.; Elsevier: New York, 1996; Vol. 2, pp 477-493.

(6) Buschmann, H.-J.; Wego, A.; Schollmeyer, E.; Döpp, D. *Supramolecular Chem.* **2000,** *11,* 225-231.

(7) Buschmann, H.-J.; Jansen, K.; Schollmeyer, E. *J. Inclusion Phenom. Macrocyclic Chem.* **2000,** *37,* 231-236.

(8) Kim, S.-Y.; Jung, I.-S.; Lee, E.; Kim, J.; Sakamoto, S.; Yamaguchi, K.; Kim, K. *Angew. Chem. Int. Ed. Engl.* **2001,** *40,* 2119-2121.

(9) Buschmann, H.-J.; Jansen, K.; Schollmeyer, E. *Thermochim. Acta* ***1998,*** *317,* 95-98.

(10) Isobe, H.; Tomita, N.; Lee, J. W.; Kim, H.-J.; Kim, K.; Nakamura, E. *Angew. Chem. Int. Ed. Engl.* **2000,** *39,* 4257-4259.

(11) Buschmann, H. J.; Jansen, K.; Schollmeyer, E. *Acta Chim. Slov.* **1999,** *46(3),* 405-411.

(12) Lagona, J.; Mukhopadhyay, P.; Chakrabarti, S.; Isaacs, L *Angewandte Chemie International Edition* Volume, **2005** *44*, 4844 – 4870.

(13) Ong, W.; Kaifer, A. E. *J. Org. Chem.*, **2004**, *69*, 1383-1385.

(14) Zhang, H.; Paulsen, E. S.; Walker, K. A.; Krakowiak, K. E.; Dearden, D. V. *J.*

Am. Chem. Soc. **2003,** *125*, 9284-9285.

(15) Rekharsky, M. V.; Yamamura, H.; Inoue, C.; Kawai, M.; Osaka, I.; Arakawa, R.; Shiba, K.; Sato, A. Ko, Y. H.; Selvapalam, N.; Kim, K.; Inoue, Y. *J. Am. Chem. Soc.* **2006**, *128*, 14871-14880.

(16) Dearden, D. V. *J. Am. Chem. Soc.* **1997**, *119*, 353-359.

(17) Liang, Y.; Dearden, D. V. *J. Phys. Chem. A*, **2002**, *106*, 9665-9671.

(18) Senko, M. W.; Canterbury, J. D.; Guan, S.; Marshall, A. G. *Rapid Commun. Mass Spectrom.* **1996**, *10*, 1839-1844.

(19) Blakney, G. T.; Hendrickson, C. L.; Marshall, A. G. In *55th ASMS Conference on Mass Spectrometry and Allied Topics*; Indianapolis, IN; 2007.

(20) Wigger, M.; Nawrocki, J. P.; Watson, C. H.; Eyler, J. R.; Benner, S. A. *Rapid Commun. Mass Spectrom.* **1997**, *11*, 1749-1752.

(21) Chen, L.; Wang, T.-C. L.; Ricca, T. L.; Marshall, A. G. *Anal. Chem.* **1987**, *59*, 449-454.

(22) Gauthier, J. W.; Trautman, T. R.; Jacobson, D. B. *Anal. Chim. Acta* **1991**, *246*, 211-225.

(23) Jiao, C. Q.; Ranatunga, D. R. A.; Vaughn, W. E.; Freiser, B. S. *J. Am. Soc. Mass Spectrom.* **1996**, *7*, 118-122.

Chapter 6

Summary and Perspective

We investigated and developed mass spectrometric techniques for the study of fundamental interactions that influence enantiodiscrimination in supramolecular complexes. We are interested in gas phase studies of fundamental interactions because the gas phase avoids complications and masking effects that may arise upon solvation. The experimental results can be directly compared with those of high-level computational studies, where the molecular system is isolated as in the gas phase. Our results show that the interactions between aromatic crown molecules and aromatic amines in the gas phase, that are important to enantiodiscrimination, are π-π stacking and hydrogen bonding. High affinity between host and guest doesn't necessarily result in better recognition. Variable temperature experiments could be done to measure the standard entropy and enthalpy for enantiodiscrimination in these systems, which might improve our understanding of the function of those fundamental interactions. This study could be used to guide improved enantiodiscrimination in some drugs and natural producs.

In the aromatic crowns and aromatic amines system, we found that the degree of chiral recognition is greater in the gas phase than in solution. However, that is not always the case. Rekharsky's work[1] shows successful chiral recognition using an achiral host in solution by conferring chirality on cucurbiturils. They utilized a proper chiral auxiliary binder to induce chirality for the CB complex and then observed the

exchange reaction between the given chiral auxiliary binder and another chiral guest. In this case, they made the chiral recognition happen in a restricted space (CB cavity), which might strengthen or hinder the discrimination. Their experimental results showed an unprecedented 95% enantioselectivity in aqueous NaCl solution for a carefully selected system, which is the highest enantioselectivity ever reported for a supramolecular system derived from an achiral host. Inspired by their results, we carried out gas phase experiments for similar systems. The highest enantioselectivity we obtained was an average 13% enantiodiscrimination for the CB[6], 2-methylpiperazine (MP) and (*S*)-sec-butylamine (BA) system. It seems that the gas phase environment is not favorable for accommodating multiple stereo centers inside the CB cavity, which is apparently necessary for induction of enantiodiscrimination in achiral CBs. Gas phase chiral recognition does not happen between the "leaving" auxiliary group and the "approaching" stronger chiral binder. To enable high induced enantioselectivity to occur with achiral hosts (CBs) in gas phase, we need to choose the proper CB molecule that can contain the stereo center of the chiral auxiliary as well as that of the stronger chiral binder. For example, we could try additional amino acids to find those that might thread through CB[7]. In such a case, no matter which amino acid is replaced by a stronger chiral binder, the chance for close contact between the stereocenters will be largely increased. In addition, we need to do more computational modeling work to guide our experiments.

For more than 15 years, we have used electrospray ionization (ESI) to transfer supramolecular complexes from solution to the gas phase. However, ESI has ion

suppression problems, especially when the sample is a mixture or it has a high concentration of salt. Therefore we developed and characterized new sample introduction techniques for fragile supramolecular complexes, focusing on porous polymer monolith nanospray ionization. Nanoelectrospray usually yields cold ionization, and analyte suppression can be greatly reduced in comparison to conventional electrospray. In comparison to conventional tapered fused silica microelectrospray emitters, the PPM emitters produce generally stronger absolute signal with much greater stability. Ion suppression is decreased with the PPM emitter to the extent that the mass spectrometrically observed complex ratio is in good agreement with the concentrations in solution. Finally, the reproducibility of emitter performance is good. One very attractive feature of nanospray is cold spray, which means fragile complexes survive the ionization process. A good system to test the "coldness" of PPM nanospray is resorc[4]arene with Fe, Mn, Co, Ni, Zn or Ga-assembled into supramolecular cages, which in the past have only been observed in very gentle sonic spray ionization (weak signal).[2] So far we have only observed the peak for half of the cage, suggesting the current PPM nanospray is not as cold as sonic spray ionization (SSI). It is likely that the tuning parameters in the source or in the electrostatic ion guide may destroy the target ion although the target ion is formed in the ionization step. We could also couple the PPM nanospray emitter with the electrosonic spray ionization invented by Dr. Cooks[3] to see whether we can obtain the features from the two ionization modes simultaneously.

CRAFTI is a recently-developed method to measure collision cross sections with

FTICR-MS. CRAFTI stands for cross-sectional areas by Fourier transform ICR. The CRAFTI technique provides information to probe the gas phase conformations of supramolecular complexes, and more importantly it allows determination of the shape, size and mass of a molecule at the same time, with ultrahigh mass resolution. Our group has considerable evidence that CRAFTI is an appropriate method for positive ions. Therefore, we are eager to know whether this new technique is valid for negative ions as well. Based on the fact that the experimental cross sections correlate linearly with theoretical values computed from likely structures, we have obtained evidence that CRAFTI is an appropriate method for negative ions. However, before we apply this method to additional negative ions, we need to better understand the factors that cause the big differences between the theoretical values and experimental values. One explanation for the big differences between the theoretical values and experimental values is that the calculation model in MOBCAL is computing cross sections for collisions with He, which is not the same as the experimental condition. We also know that ion dissociation is a large contributor to CRAFTI cross sections so we expect them to be larger than the MOBCAL values. We have to further optimize the CRAFTI technique to make it a general technique. We need to carefully tune the excitation amplitude and the isolation amplitude to make the signal strong and monoisotopic for weak ions. Collision cross sections yield useful conformational information, so one of the applications of CRAFTI is to examine the conformations of different isomers. For example, we could electrospray mixtures of isomers with different cross sections to see whether these isomers can be detected and quantified.

Biological molecules will be another target in CRAFTI application. For instance, we could determine the degree of unfolding in proteins by measuring their collision cross sections and multiple charges on the proteins.

References

(1) Rekharsky, M. V.; Yamamura, H.; Inoue, C.; Kawai, M.; Osaka, I.; Arakawa, R.; Shiba, K.; Sato, A. Ko, Y. H.; Selvapalam, N.; Kim, K.; Inoue, Y. *J. Am. Chem. Soc.* **2006**, *128*, 14871-14880.

(2) Gardner J. S. "Tetradipicolyamine-substituted resorc[4]arene cavitands: I. Anion binding and transition metal assembled coordination cages and nanoarchitectures. II. Polymer inclusion membranes applied to anion separations" Ph.D. Dissertation, Brigham Young University, Provo, UT, June, 2005.

(3) Takáts, Z.; Wiseman, J. M.; Gologan, B.; Cooks, R. G. *Anal. Chem.* **2004**, *76*, 4050-4058.